

# University of St Andrews



Full metadata for this thesis is available in  
St Andrews Research Repository  
at:

<http://research-repository.st-andrews.ac.uk/>

This thesis is protected by original copyright

**Carrier transport, ultrafast spin dynamics and  
polarisation switching in InGaAsP multiple quantum wells.**

**Dawn Marshall, MSci.**



*J.F. Allen Physics Research Laboratory  
Department of Physics and Astronomy*

*University of St Andrews*

*North Haugh*

*St Andrews KY16 9SS*

*Scotland*

A thesis submitted to the University of St Andrews  
in application for the degree of Doctor of Philosophy

September 2000



in D<sup>684</sup>

I, Dawn Marshall, hereby certify that this thesis, which is approximately 29,000 words in length, has been written by me, that it is the record of work carried out by me and that it has not been submitted in any previous application for a higher degree.

Date 27.10.00

Signature of candidate

I was admitted as a research student in September 1997 and as a candidate for the degree of Doctor of Philosophy in Physics; the higher study for which this is a record was carried out in the University of St. Andrews between 1997 and 2000.

Date 27.10.00

Signature of candidate

I hereby certify that the candidate has fulfilled the conditions of the Resolution and Regulations appropriate for the degree of Doctor of Philosophy in the University of St. Andrews and that the candidate is qualified to submit this thesis in application for that degree.

Date 27/10/00

Signature of supervisor

In submitting this thesis to the University of St. Andrews I understand that I am giving permission for it to be made available for use in accordance with the regulations of the University Library for the time being in force, subject to any copyright vested in the work not being affected thereby. I also understand that the title and abstract will be published, and that a copy of the work may be made and supplied to any *bona fide* library or research worker.

Date 27/10/00

Signature of candidate



## Abstract

The carrier dynamics and nonlinear optical properties of room temperature InGaAsP multiple quantum well semiconductors with band-gap energies at 1.5 microns are reported. Measurements were made on picosecond timescales using a new optical parametric oscillator (OPO) source. Excitonic nonlinearities, carrier recombination times, carrier diffusion and polarisation switching were studied using pump-probe, time resolved photoluminescence and transient grating techniques.

A picosecond pulse OPO was constructed using PPLN as the nonlinear medium and pumped by a mode-locked Ti:Sapphire laser. A tuning range of 1.3 to 1.57 microns was demonstrated and characterised.

Six samples were investigated. Bimolecular radiative recombination gave a long recombination time of around 200ns in an undoped sample while carrier sweep-out was proposed as the dominant mechanism in five p-i-n structures with recovery times in the range of 6 to 40ns.

Both amplitude and spin gratings were used to measure electron and hole mobilities. Hole mobilities were consistent with bulk InGaAsP while a high electron mobility was identified. The latter was attributed to the high carrier density regime for the electron diffusion.

Linear and circular polarisations were employed in pump-probe measurements to give spin relaxation times with the conclusion that the D'Yakonov Perel mechanism dominated in this material system at room temperature. An ultrafast polarisation switch was demonstrated using electron spin and a new induced birefringence discovered.

# Contents

<b>CHAPTER 1 INTRODUCTION.....</b>	<b>1</b>
1-1 BIBLIOGRAPHY .....	5
<b>CHAPTER 2 SEMICONDUCTOR QUANTUM WELLS.....</b>	<b>7</b>
2-1 SUMMARY .....	7
2-2 INTRODUCTION TO THE SEMICONDUCTOR QUANTUM WELL .....	7
2-3 ENERGY LEVELS .....	8
2-4 OPTICAL PROPERTIES .....	11
2-4-1 <i>Density of states</i> .....	11
2-4-2 <i>Excitons</i> .....	13
2-4-3 <i>Selection rules</i> .....	14
2-4-4 <i>Exciton Saturation</i> .....	16
2-5 TRANSPORT DYNAMICS .....	19
2-5-1 <i>Drift mobility</i> .....	19
2-5-2 <i>Scattering</i> .....	21
2-5-3 <i>Diffusion</i> .....	22
2-5-4 <i>Ambipolar diffusion</i> .....	23
2-6 FABRICATION OF QUANTUM WELLS.....	24
2-6-1 <i>Vapour phase epitaxy (VPE)</i> .....	24
2-6-2 <i>Molecular beam epitaxy (MBE)</i> .....	24
2-6-3 <i>Metal organic chemical vapour deposition (MOCVD)</i> .....	24
2-7 INGAAs(P).....	26
2-8 BIBLIOGRAPHY .....	29
<b>CHAPTER 3 PPLN OPTICAL PARAMETRIC OSCILLATOR.....</b>	<b>30</b>

3-1 SUMMARY .....	30
3-2 THE OPTICAL PARAMETRIC OSCILLATOR.....	30
3-2-1 <i>Second order nonlinearity</i> .....	31
3-3 WAVE PROPAGATION IN NONLINEAR MATERIALS AND THREE WAVE MIXING.....	32
3-4 BIREFRINGENT PHASE MATCHED INTERACTIONS IN NONLINEAR MATERIALS .....	33
3-5 QUASI-PHASE MATCHED INTERACTIONS .....	35
3-6 CAVITY DESIGN AND FOCUSING .....	37
3-7 THE 1.3 TO 1.57 MICRON PPLN OPTICAL PARAMETRIC OSCILLATOR .....	39
3-8 ALIGNMENT OF THE PPLN OPO.....	42
3-9 AUTOCORRELATION MEASUREMENTS .....	44
3-10 BIBLIOGRAPHY .....	46

## **CHAPTER 4 EXPERIMENTAL TECHNIQUES AND SAMPLE DESCRIPTION**

.....	48
4-1 SUMMARY .....	48
4-2 DEGENERATE TIME RESOLVED PUMP PROBE EXPERIMENTS .....	48
4-3 TRANSIENT GRATING STUDIES .....	52
4-4 TIME RESOLVED PHOTOLUMINESCENCE .....	53
4-5 INTRODUCTION TO THE INGAAS(P) SAMPLES.....	56
4-6 THEORY FOR ENERGY CALCULATIONS.....	56
4-7 SAMPLE MR534 .....	58
4-8 SAMPLE MR535 .....	58
4-9 SAMPLE MR610 .....	59
4-10 SAMPLE MR611 .....	60
4-11 SAMPLE MR850 .....	62
4-12 SAMPLE MR1168.....	63
4-13 REFERENCES .....	65

<b>CHAPTER 5 CARRIER LIFETIME.....</b>	<b>66</b>
5-1 SUMMARY .....	66
5-2 INTRODUCTION .....	66
5-3 SHOCKLEY-READ RECOMBINATION .....	67
5-4 RADIATIVE RECOMBINATION .....	68
5-5 AUGER RECOMBINATION .....	68
5-6 THERMIONIC EMISSION AND TUNNELLING .....	70
5-7 EXPERIMENTAL SET-UP .....	72
5-8 RESULT FOR SAMPLE MR1168 (UNDOPED) .....	74
5-9 DISCUSSION FOR MR1168 (UNDOPED).....	75
5-10 RESULTS FOR THE P-I-N STRUCTURE SAMPLES .....	77
5-11 DISCUSSION FOR P-I-N STRUCTURES.....	82
<i>5-11-1 Conclusion.....</i>	86
5-12 BIBLIOGRAPHY .....	87
<b>CHAPTER 6 SPIN RELAXATION.....</b>	<b>88</b>
6-1 SUMMARY .....	88
6-2 INTRODUCTION .....	88
6-3 SPIN RELAXATION MECHANISMS.....	89
<i>6-3-1 D'yakonov and Perel mechanism.....</i>	89
<i>6-3-2 Elliot and Yafet mechanism .....</i>	92
<i>6-3-3 Bir, Aronov and Pikus mechanism .....</i>	93
<i>6-3-4 Dominant mechanisms in quantum well semiconductors.....</i>	94
6-4 DYNAMICAL MODEL OF THE SPIN RELAXATION.....	95
6-5 SPIN RELAXATION EXPERIMENTAL DETAILS .....	99
6-6 RESULTS.....	100

6-7 DISCUSSION.....	107
6-8 CONCLUSION .....	111
6-9 BIBLIOGRAPHY .....	112
<b>CHAPTER 7 ALL OPTICAL SPIN POLARISATION SWITCH.....</b>	<b>116</b>
7-1 SUMMARY .....	116
7-2 INTRODUCTION .....	116
7-3 AN ALL-OPTICAL POLARISATION SWITCH AT 1.5 MICRONS .....	119
7-4 RESULTS.....	121
<i>7-4-1 All optical polarisation switch.....</i>	<i>121</i>
<i>7-4-2 Experimental analysis of switch.....</i>	<i>125</i>
7-5 ANALYSIS.....	129
7-6 EXPERIMENTAL SET-UP TO DETERMINE THE BIREFRINGENCE.....	130
7-7 BIREFRINGENCE RESULTS .....	131
7-8 COMBINATION OF THE SWITCH AND BIREFRINGENCE .....	136
7-9 MODEL OF COMBINATION OF SPIN POLARISATION AND BIREFRINGENCE.....	136
7-10 CONCLUSION .....	140
7-11 BIBLIOGRAPHY .....	141
<b>CHAPTER 8 TRANSIENT GRATING STUDIES .....</b>	<b>144</b>
8-1 SUMMARY .....	144
8-2 INTRODUCTION .....	144
8-3 AMPLITUDE GRATINGS .....	145
<i>8-3-1 Formation of an amplitude grating.....</i>	<i>145</i>
<i>8-3-2 Amplitude grating decay.....</i>	<i>147</i>
8-4 SPIN GRATINGS.....	149
<i>8-4-1 Formation of a spin grating.....</i>	<i>149</i>

<i>8-4-2 Spin grating decay.....</i>	150
8-5 EXPERIMENTAL SET-UP .....	152
8-6 RESULTS.....	152
<i>8-6-1 Two beam interference .....</i>	152
<i>8-6-2 Time resolved amplitude gratings.....</i>	154
<i>8-6-3 Time resolved spin gratings.....</i>	160
8-7 ANALYSIS.....	164
<i>8-7-1 Amplitude grating discussion and conclusion .....</i>	164
<i>8-7-2 Spin grating discussion and conclusion .....</i>	164
8-8 BIBLIOGRAPHY .....	167
<b>CHAPTER 9 CONCLUSIONS .....</b>	<b>170</b>
<b>CHAPTER 10 PUBLICATIONS .....</b>	<b>175</b>
10-1 JOURNAL PUBLICATIONS .....	175
10-2 CONFERENCE PUBLICATIONS .....	176
<b>CHAPTER 11 ACKNOWLEDGEMENTS .....</b>	<b>178</b>

# Chapter 1

## Introduction

In recent years the demands of the telecommunication industry have been pushing forward research in the area of optoelectronics. Out of this has arisen the exciting new field of spintronics where the spin of an electron is used to control, store and transfer optical signals and information<sup>1,2</sup>.

The advent of growth techniques such as molecular beam epitaxy (MBE) and metal-organic chemical vapour phase epitaxy (MOCVD) in the 1970s enabled the production of accurately grown layers of semiconductor. Most importantly, the layers can now be grown so thin that quantisation effects can be observed. This occurs when the thickness is as small as the de Broglie wavelength of the electron. By sandwiching one of these ultra-thin layers between two layers of a different material with higher bandgap it is possible to create a square potential difference. The carriers are confined in one direction and this has been termed the semiconductor quantum well. Further confinement leads to quantum wires and dots. The potential well can be described by Schrödinger's theory of quantum mechanics and is a practical way of observing the situation of a particle in a box.

The confinement causes a change in the absorption characteristics when compared to the bulk material. There is an enhancement of the absorption effects of the quasi-particle known as an exciton. This is a bound electron hole pair that is then observable at room temperature in the quantum wells. A way of further enhancing the absorption is to grow a multiple quantum well. Many identical layers of the quantum well

sandwiches are grown on top of each other. Ideally, the multiple quantum well will have the same optical effects as a single quantum well but with  $n$  times enhancement for  $n$  layers.

Quantum wells also show a number of new properties when compared to the bulk material. One of the most interesting of these is the quantum confined Stark effect (QCSE) where the application of an electric field across the quantum wells produces a change in the absorption edge<sup>3</sup>. This red-shift is utilised in electro-optic devices such as the SEED (self electro-optic device)<sup>4</sup>. Other applications of quantum wells include lasers<sup>5</sup>, optical switches<sup>6,7</sup> and modulators<sup>8-10</sup>.

To investigate the nonlinear properties of quantum wells ultrafast spectroscopy is used<sup>11,12</sup>. One such technique is to use the procedure of pump-probe. This is where the optical properties of the semiconductor are changed by one laser pulse, the pump, and then examined with another of less intensity, the probe. The probe beam can be delayed in time to investigate temporal changes in transmission due to the absorption saturation or other effects of the pump pulse.

The optical pulse source used to look at the multiple quantum wells discussed in this thesis is an optical parametric oscillator (OPO). The OPO is an attractive source of ultrashort pulses that is capable of producing a wide range of wavelengths in either continuous wave or pulsed form. The OPO consists of a nonlinear crystal that is placed inside a resonator and pumped with a high power wave. Burneika demonstrated the potential of the pulsed OPO in 1972<sup>13</sup>. It was proposed that the cavity lengths of the OPO and the mode-locked pump laser were set equal, termed synchronously pumping, in order to create pulses at the same repetition rate as the pump laser.

In the work presented in this thesis the pump laser is a picosecond self-modelocked Ti-Sapphire laser (Spectra-Physics Tsunami) and the nonlinear crystal is periodically poled lithium niobate (PPLN). This gives a tuning range of 1.3 to 1.57 microns.

The wavelength range of 1.3 to 1.55 microns is essential in the field of telecommunications. At these points there is a window of transmission in the attenuation of the optical fibres, Figure 1-1. To construct devices based on quantum wells that operate at these communication wavelengths, materials with the corresponding band-gaps are engineered.

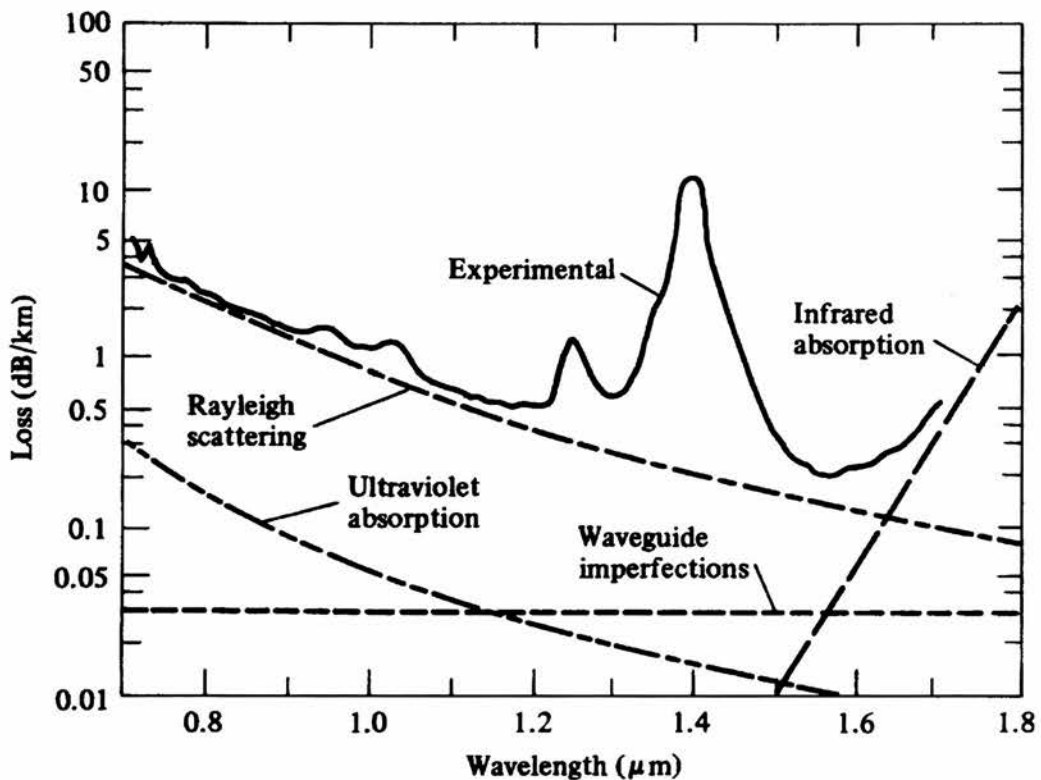


*Figure 1-1 Attenuation as a function of wavelength in optical fibres. Transmission windows can be found at 1.3 and 1.55 microns.*

The alloy semiconductor InGaAs(P) has a bandstructure that can provide operation at 1.5 microns at room temperature given the correct alloy composition. Lattice matching to InP enables transmission through the substrate at 1.5 microns. The bandgap can be

## Chapter 1

## Introduction

further engineered by altering the quantisation conditions to enable fine-tuning of the exciton resonance. In this thesis some of the carrier dynamics and device applications of InGaAs(P) multiple quantum wells are investigated.

Chapter 2 introduces the basic principles of semiconductor quantum wells. Chapter 3 describes the configuration and operation of the PPLN OPO. Chapter 4 outlines the experimental techniques used for transient studies and describes the composition of the InGaAs(P) samples. Chapter 5, 6 and 8 study the carrier lifetime, spin relaxation and diffusion characteristics respectively. The diffusion was measured to obtain the mobility, which was required for theoretical calculations of the spin relaxation times. Chapter 7 describes how the spin of the electrons can be utilised to create an all-optical polarisation switch and illustrates the effects of birefringence. Chapter 9 combines all the results into a conclusion.

**1-1 Bibliography**

- 1 J. M. Kikkawa, I. P. Smorchkova, N. Samarth, and D. D. Awschalom, "Room-temperature spin memory in two-dimensional electron gases," *Science*, **277** (5330), pp. 1284-1287, 1997.
- 2 D. D. Awschalom and J. M. Kikkawa, "Electron spin and optical coherence in semiconductors," *Physics Today*, **52** (6), pp. 33-38, 1999.
- 3 D. A. B. Miller, D. S. Chemla, T. C. Damen, A. C. Gossard, W. Wiegmann, T. H. Wood, and C. A. Burrus, "Band-Edge Electroabsorption in Quantum Well Structures: The Quantum-Confinement Stark Effect," *Phys. Rev. Lett.*, **53** (22), pp. 2173-2176, 1984.
- 4 D. A. B. Miller, "Quantum-Well Self-Electro-Optic Effect Devices," *Opt. and Quant. Elect.*, **22**, pp. S61-S98, 1990.
- 5 P. S. Zory, *Quantum well lasers* (Academic Press, 1993).
- 6 I. Gontijo, D. T. Neilson, A. C. Walker, G. T. Kennedy, and W. Sibbett, "Nonlinear InGaAs-InGaAsP single-quantum-well all-optical switch - Theory and experiments," *IEEE J. Quantum Electron.*, **32** (12), pp. 2112-2121, 1996.
- 7 K. G. Ravikumar, T. Aizawa, S. Suzuki, and R. Yamauchi, "Observation of Polarization Independent Electric-Field Effect in InGaAs/InP Tensile Strained Quantum-Well and Its Proposal For Optical Switch," *App. Phys. Lett.*, **61** (16), pp. 1904-1906, 1992.
- 8 Y. Kuwamura, Y. Nishiuma, and M. Yamada, "Design of a surface-illuminated-type semiconductor optical modulator with multi-quantum-well structures," *Electronics and Communications in Japan Part II-Electronics*, **83** (5), pp. 28-39, 2000.

- 9 E. S. Nam, S. W. Lee, D. H. Jang, J. G. Lee, and K. E. Pyun, "Monolithic integration of a 1.55-micron strained multiple-quantum-well distributed feedback laser and quantum-confined Stark-effect modulator by metal organic vapor-phase epitaxy using an InP-buffer-layer incorporated Butt coupling scheme," *Journal of the Korean Physical Society*, **36** (4), pp. 228-232, 2000.
- 10 M. Wraback and H. Shen, "A femtosecond, polarization-sensitive optically addressed modulator based on virtual exciton effects in an anisotropically strained multiple quantum well," *App. Phys. Lett.*, **76** (10), pp. 1288-1290, 2000.
- 11 Alfano, *Semiconductors Probed by Ultrafast Laser Spectroscopy Volume I* (Academic Press Inc., 1984).
- 12 Alfano, *Semiconductors Probed by Ultrafast Laser Spectroscopy Volume II* (Academic Press Inc., 1984).
- 13 K. Burneika, M. Ignatavichyus, V. Kabelka, A. Piskarskas, and A. Stabinis, "Parametric light amplification and oscillation in KDP with mode-locked pump," *IEEE J. Quantum Electron.*, **8**, pp. 574, 1972.

## Chapter 2

# Semiconductor quantum wells

### ***2-1 Summary***

In this chapter the quantum well is introduced. Optical and carrier transport properties and semiconductor growth techniques are discussed. InGaAs(P) quantum wells are outlined.

### ***2-2 Introduction to the semiconductor quantum well***

A multiple quantum well is a structure constructed of very thin layers of semiconductor material where the electrons and holes behave like standing waves as if they are trapped in a quantum box, i.e. energy levels are quantised. In the quantum well, the motion of the electrons is restricted in one dimension to a distance comparable to or smaller than the Bohr radius of the exciton. For typical semiconductors this limit is reached for well layer thicknesses below tens of nanometers.

The electrons and holes can exist either in the same semiconductor, type I heterostructures, or in different semiconductor materials, type II heterostructures as shown in Figure 2-1. The band-offset ratio is defined as  $\Delta E_c : \Delta E_v$ .

Thermally generated electrons and holes are intrinsic carriers. To increase the free carrier density impurities known as dopants are introduced. They are chosen so as to provide one more or one less electron per impurity atom than the host semiconductor (donors and acceptors). The semiconductor is then labelled n-type, p-type or intrinsic depending whether it is doped with donors or acceptors or the doping is low enough to be dominated by thermally generated carriers.

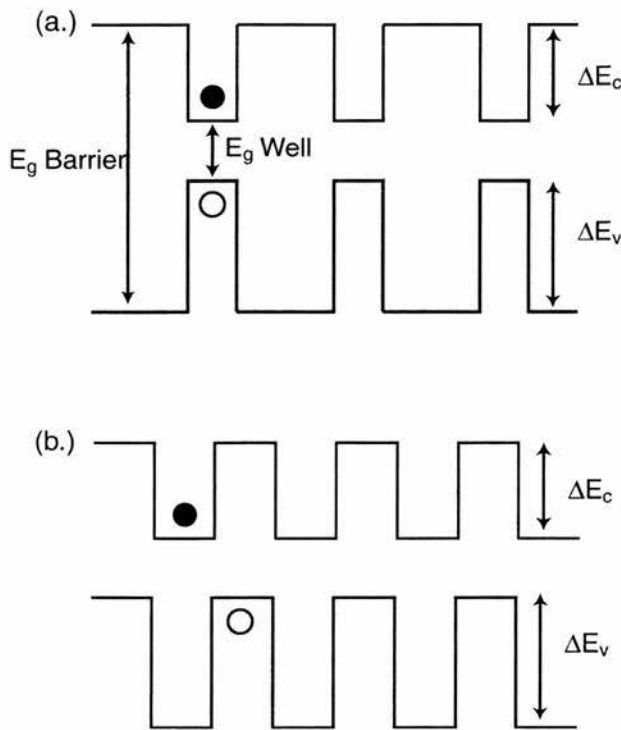


Figure 2-1 Band structure for (a.) type I and (b.) type II semiconductors. The filled and unfilled circles indicate where the electrons and holes reside respectively.

### 2-3 Energy levels

To describe quantum well energy levels in the conduction band we start from the particle in a box view. Schrödinger's equation in one dimension is:

$$\frac{-\hbar^2}{2m^*} \frac{d^2\phi_n}{dz^2} + V(z)\phi_n = E_n\phi_n \quad (2.1)$$

where  $\phi$  is the wavefunction of the particle,  $m^*$  the effective mass and  $V(z)$  the band edge energy. For the simplest case of an infinite quantum well of length  $L_z$  with confinement in the z direction the solutions for the energy levels and wavefunctions are:

$$E_n = \frac{\hbar^2}{2m^*} \left[ \frac{n\pi}{L_z} \right]^2, n = 1, 2, 3.. \quad (2.2)$$

and

$$\phi_n = \sqrt{\frac{2}{L}} \sin\left(\frac{n\pi z}{L_z}\right) \quad (2.3)$$

However, in a real semiconductor quantum well the barriers are not infinite.

In the plane of the layers the electrons are not affected by the confinement and the band structure of this plane is similar to bulk and can usually be approximated by a parabola near  $k=0$ :

$$E_{x,y} = \frac{\hbar^2 (k_x^2 + k_y^2)}{2m_a^*} \quad (2.4)$$

For interaction between light and electrons in the quantum wells the quantisation must be taken into account and hence the conduction band is described by the finite case of the Schrödinger equation with a potential height of  $V_0$ . If we apply continuity conditions to equation (2.1) and its first derivative we arrive at:

$$\frac{k}{m_a^*} \tan\left(\frac{kL}{2}\right) = \frac{K}{m_b^*} \quad (2.5)$$

and

$$\frac{k}{m_a^*} \cot\left(\frac{kL}{2}\right) = -\frac{K}{m_b^*} \quad (2.6)$$

where  $m_a^*$  and  $m_b^*$  are the electron effective masses in the well and barrier region respectively,  $k^2 = \frac{2m_a^*}{\hbar^2} (E_n - V_0)$  and  $K^2 = \frac{2m_a^*}{\hbar^2} E_n$ . Equations (2.5) and (2.6) cannot be solved analytically and so must be evaluated by graphical or numerical methods.

The valence band is more complicated as the quantum confinement lifts the four-fold degeneracy of the holes at  $k=0$  in 3D. The  $\mathbf{k.p}$  interaction as described by the Luttinger

Hamiltonian, describing the valence band curvature in terms of the hole effective masses, then yields the dispersion in the  $y$ -direction<sup>1</sup>. Finally higher order terms lead to an anti-crossing behaviour<sup>2</sup>, as shown in Figure 2-2. The introduction of more wells leads to a continuous band of states. Hence, we have a lifting of degeneracy at  $k=0$  with the heavy hole of angular momentum  $J_z = \pm \frac{3}{2}$  and the light hole  $J_z = \pm \frac{1}{2}$ .

Dingle et al studied the transition from single wells to multiple connected wells by use of optical absorption and discovered that  $N$ -degenerate levels give rise to bands with  $2N$  states<sup>3</sup>.

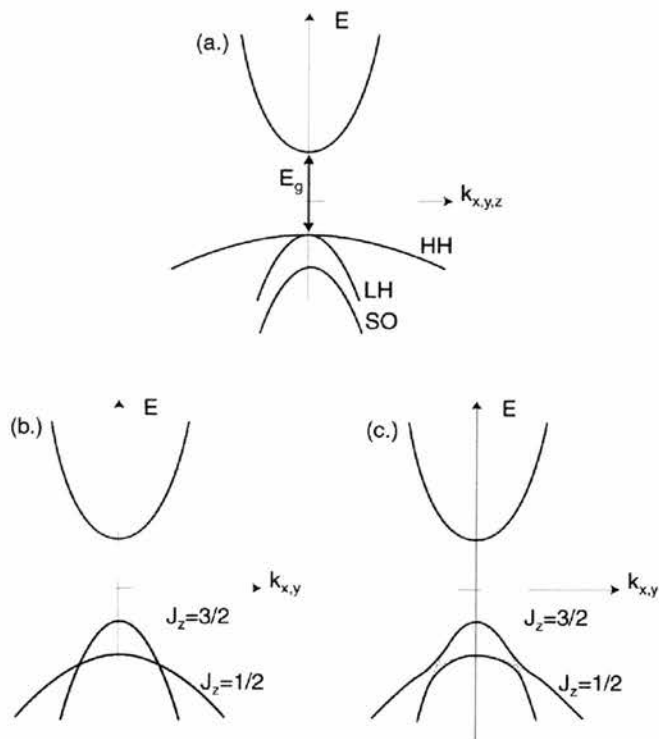


*Figure 2-2 Schematic dispersion of the energy levels (a.) in 3D (b.) showing the crossing behaviour in presence of a square well confinement in the  $z$ -direction (c.) with the inclusion of higher order terms.*

## 2-4 Optical properties

### 2-4-1 Density of states

The density of states defines optical absorption in a semiconductor. It is defined as the number of available electronic states per unit volume per unit energy around an energy  $E$ . In a bulk semiconductor, assuming parabolic bands and taking into account that the electron is a fermion and therefore has two possible spin states with a given energy, the density of states is given by:

$$D_{3D}(E) = \frac{1}{2\pi^2} \left( \frac{2m^*}{\hbar^2} \right)^{\frac{3}{2}} E^{1/2} \quad (2.7)$$

When we impose confinement to 2D, each energy level has an associated 2D parabolic band of the form  $E_\perp = \frac{\hbar^2 k_\perp^2}{2m}$  which has a constant density of states given by:

$$D_{2D}(E) = \frac{nm^*}{\pi\hbar^2} \frac{1}{a}, n=1, 2, 3, \dots \quad (2.8)$$

This creates a step like spectra and the corresponding absorption spectrum is shown in comparison to the 3D case in Figure 2-3.

Figure 2-4 shows a typical InGaAsP multiple quantum well absorption spectra. The lifting of the degeneracy between the light and heavy holes can be seen from double peaks at  $n=1$  and there is a clear step at the start of absorption into each band. Also, at the band edge absorption peaks due to excitons can be observed.

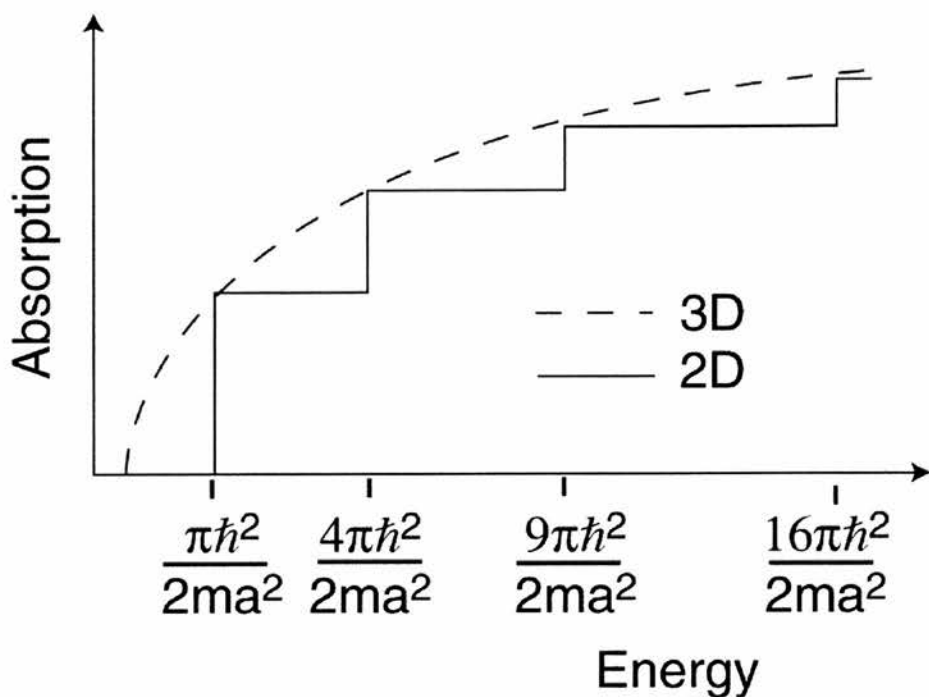


Figure 2-3 Comparison of the parabolic 3D and step-like 2D density of states.

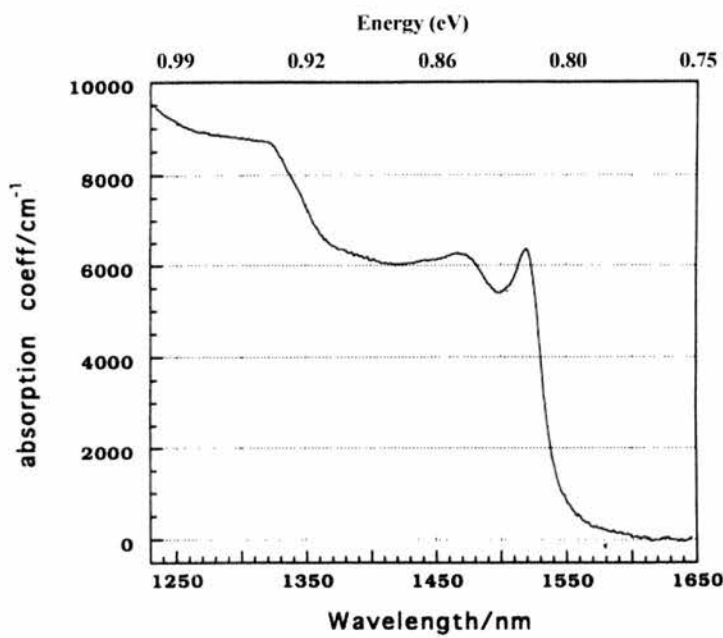


Figure 2-4 Room temperature for an InGaAsP MQW showing the heavy and light holes  
(sample MR535)

## 2-4-2 Excitons

An exciton is a bound electron hole pair where the attraction between the pair can be described as a Coulomb interaction:

$$V(r) = -\frac{e^2}{\epsilon r} \quad (2.9)$$

In bulk semiconductors excitons are generally only observable in very high quality samples due to their small binding energies. However the confinement in quantum wells increases the binding energy and improves the optical transition strength resulting in the observation of the sharp resonance peaks in absorption spectra.

There are two distinct types of exciton, Frenkel and Wannier (otherwise known as Wannier-Mott). A Frenkel exciton exists in solids with large effective electron and hole masses and the exciton itself will only extend to a few lattice spacings. The Wannier exciton is weakly bound and non-localised, where the Bohr radius is large in comparison with the length of the lattice unit cell. The Wannier exciton is responsible for excitonic absorption features in quantum well semiconductors at room temperature.

In bulk material the exciton is said to be three dimensional but as the confinement becomes of the order of the exciton's Bohr radius it can be better described by a two dimensional analysis. In the 3D situation the exciton can be thought of as being analogous to the hydrogen atom:

$$E_n^{3D} = E_n - \frac{R_0}{n^2} \quad (2.10)$$

$$\phi_{1s}^{3D} = \frac{1}{\sqrt{\pi a_0^3}} \exp\left(-\frac{r}{a}\right) \quad (2.11)$$

where:

$$R_0 = \frac{e^4 m^*}{2\epsilon^2 \hbar^2} \text{ and } a_0 = \frac{\epsilon \hbar^2}{m^* e^2} \quad (2.12)$$

with  $\epsilon$  the dielectric constant. If this is now considered in the 2D case the equations will transform to:

$$E_n^{2D} = E_n - \frac{R_0}{\left(n - \frac{1}{2}\right)^2} \quad (2.13)$$

and

$$\phi_{1s}^{2D} = \sqrt{\frac{2}{\pi}} \frac{2}{a_0} \exp\left(-\frac{2r}{a}\right) \quad (2.14)$$

The binding energy is increased due to the fact that the increased confinement increases the overlap between the electron and hole and their attraction. As a result this reduces the 2D Bohr radius. This allows the exciton to be resolved at room temperature in quantum well semiconductors.

### 2-4-3 Selection rules

In order to understand what is happening when we excite an electron from the valance band to the conduction band we must examine some selection rules. Firstly the overlap integral between the two states must be non-zero. For the z-component of the wavefunction this integral is given by:

$$\langle \varsigma_{ei}(z_e) | \varsigma_{hj}(z_h) \rangle = \int_{-\infty}^{\infty} \varsigma_{ei}(z_e) \varsigma_{hj}(z_h) dz \quad (2.15)$$

where  $i, j$  are the numbers of conduction/valence band energy levels. The functions  $\varsigma_{ei}(z_e)$  and  $\varsigma_{hj}(z_h)$  are orthonormal for an infinite well and therefore the overlap integral is non-zero if  $i = j$ , i.e. only transitions between confined conduction and valence bands with the same quantum numbers are allowed<sup>3</sup>. In a finite well the

wavefunctions extend out into the barriers, which means that they are not exactly orthonormal and certain forbidden transitions with different quantum numbers can now occur.

Another set of transition rules exist in the form of dipole matrix elements for the optically induced transitions. Dipole matrix elements are given by  $\langle u_f | D | u_i \rangle$  where  $u_i$  and  $u_f$  are the wavefunctions of the initial and final states and D is the dipole matrix operator. For light propagating perpendicular to the layers only those dipole moments in the plane can absorb or radiate. The selection rules dictate that free electron-hole absorption must be three times larger for the HH band than for the LH band. Under circularly polarised light excitation 100% spin polarisation occurs when electrons are excited from one of the HH or LH bands, as shown in Figure 2-5. In the bulk case this would be 50%. The polarisation is defined as:

$$P = \frac{N_\uparrow - N_\downarrow}{N_\uparrow + N_\downarrow} \quad (2.16)$$

where  $N_\uparrow$  is the number of spin up carriers and  $N_\downarrow$  the number of spin down carriers.

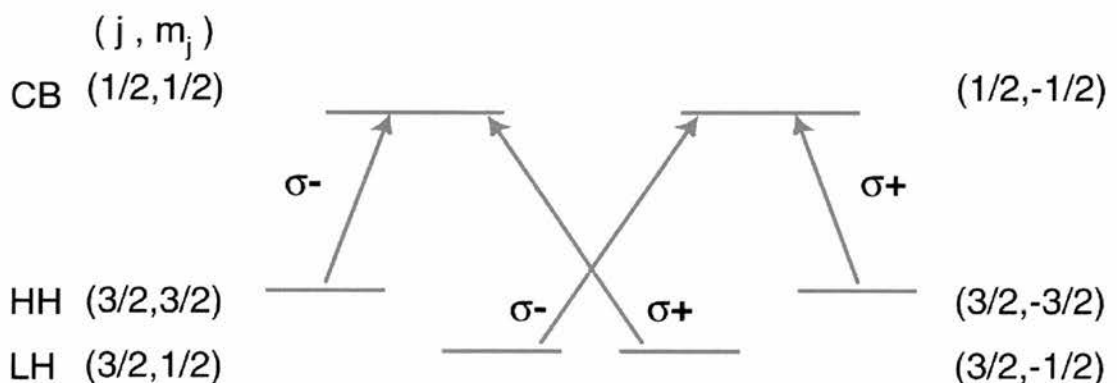


*Figure 2-5 Selection rules showing the transitions from the heavy and light holes to the conduction band with circularly polarised excitation and propagation in the z-direction.*

### 2-4-4 Exciton Saturation

One fundamental nonlinearity of semiconductors is the absorption saturation or bleaching of the excitons by photoexcited free or bound electron hole pairs<sup>4</sup>. The mechanisms involved in this saturation are important in the field of electro-absorptive devices.

Excitonic saturation can be divided into phase-space filling (PSF) and Coulomb contributions. PSF arises from the fact that each  $k$ -state has one spin up and one spin down electron. It causes directly a reduction of the exciton oscillator strength by reducing the number of single particle states that can contribute to the bound electron hole state. Schmitt-Rink et al presented a theoretical report on the transient properties of these exciton nonlinearities<sup>5</sup>. Firstly, the linear optical properties must be considered. The linear susceptibility,  $\chi$ , is defined by:

$$\chi = \sum_n \frac{f_n}{\omega - \omega_n + i\gamma_n} \quad (2.17)$$

The index  $n$  is summed over all states,  $\omega_n$  is the energy of each state,  $\gamma_n$  the width and  $f_n$  the oscillator strength of the transition. At the 1s exciton peak this susceptibility can be shown to be:

$$\chi \sim \frac{f_{1s}}{\omega - \omega_{1s} + i\gamma_{1s}} \quad (2.18)$$

The nonlinearity arises when optical excitation changes one or more of  $f_{1s}$ ,  $\gamma_{1s}$  or  $\omega_{1s}$ . It is found for excitons in room temperature quantum wells that there is no change observed in  $\omega_{1s}$  which may be understood in terms of the charge neutrality of the exciton. The change of the exciton oscillator strength is examined. It is stated that:

$$\frac{\delta f_{1s}}{f_{1s}} = -\frac{N}{N_s} \quad (2.19)$$

where  $N$  and  $N_s$  represent the density of electron hole pairs and the saturation density respectively

There are two processes that contribute to changes in  $f_{1s}$ . These are the blocking mechanism due to the exclusion principle and changes in the exciton orbital wavefunction due to the presence of electron hole pairs. The latter includes exchange and long-range Coulomb effects.

The resonant generation of excitons results in a distribution of electrons and holes and is given by:

$$f_e(k) = f_h(k) = \frac{N}{2} |U_{1s}(k)|^2 \quad (2.20)$$

where  $f_{e/h}(k)$  is the Boltzmann distribution of the electrons/holes and  $U_{1s}(k)$  the Fourier transform of the relative orbital wavefunction,  $U_{1s}(r)$ . The physical meaning of this is that the exciton is made from a linear contribution of single particle fermion states which are distributed according to  $U_{1s}(k)$  and the creation of one exciton corresponds to an occupation probability in the fermion phase space  $|U_{1s}(k)|^2$ . This is equally shared between the spin up and down states.

For the case of 2D these transform to:

$$U_{1s}(r) = \left(\frac{2}{\pi}\right)^2 \frac{2}{a_0} e^{-2r/a_0} \quad (2.21)$$

and

$$U_{1s}(k) = \sqrt{2\pi} \frac{a_0}{\left[1 + \left(\frac{a_0 k}{2}\right)^2\right]^{3/2}} \quad (2.22)$$

where  $a_0$  is the 3D Bohr radius. The relative change in the exciton oscillator strength due to the exclusion principle through PSF is:

$$\frac{\delta f_{1s}}{f_{1s}} = -\sum_k [f_e(k) + f_n(k)] \frac{U_{1s}(k)}{U_{1s}(r=0)} \quad (2.23)$$

Hence, states that are already occupied by electrons or holes are no longer available for the formation of excitons. For an exciton gas:

$$\frac{1}{N} = \frac{32}{2} \pi a_{2D}^2 \quad (2.24)$$

Therefore, when an exciton is created, an area of the semiconductor around the bound electron hole pair cannot hold any more excitons. This area is greater than the 2D Bohr radius,  $a_{2D}^2$ , of the exciton.

Coulomb screening is used to signify the decrease in the Coulomb potential of a charge when other charges are present. It is related to the charge and density of the carriers independent of their spin. The addition of a charge causes a redistribution of the carriers and a reduction in the overall energy of the system, the effective energy of the test charge and the exciton binding energy. The screening parameter,  $q_s$ , is independent of the carrier density at low temperatures<sup>5</sup>:

$$q_s = \frac{2(m_e + m_h)}{\mu a_0} \quad (2.25)$$

And it decreases at high temperatures:

$$q_s = \frac{4\pi Ne^2}{\epsilon_0 k_B T} \quad (2.26)$$

where  $\mu$  is the electron-hole reduced mass,  $\epsilon_0$  the dielectric constant and  $k_B$  the Boltzmann constant.

Exchange effects lead to the renormalization of the single particle and exciton states and may also lead to a reduction in the oscillator strength. It arises from the fermion character of the carriers. To examine the exchange effects Schmitt-Rink<sup>5</sup> et al described the unperturbed and perturbed electron hole motion by the Hamiltonians  $H$  and  $H_0$  and summed equation (2.27) over all the excited states of the exciton, resulting in equation (2.28).

$$\frac{\delta f_{1s}}{f_{1s}} = \sum_{n(\neq 1s)} \left[ \frac{\langle 1s | H - H_0 | n \rangle}{\omega_{1s} - \omega_n} \frac{U_n^*(r=0)}{U_{1s}^*(r=0)} + \frac{\langle n | H - H_0 | 1s \rangle}{\omega_{1s} - \omega_n} \frac{U_n(r=0)}{U_{1s}(r=0)} \right] \quad (2.27)$$

$$\frac{1}{N_s} = \frac{4832}{1225} \pi a_{2D}^2 \quad (2.28)$$

This theory presented by Schmitt-Rink et al was based in the fact that the excitons were in a strictly 2D state.

We can distinguish between PSF and Coulomb contributions to exciton saturation by making use of the selection rules and circularly polarised light. In GaAs quantum wells it was found that screening remains an important contribution although PSF becomes increasingly dominant in narrower wells<sup>6</sup>. Excitonic PSF was approximately four times larger than the free carrier component in narrower wells.

## 2-5 Transport dynamics

### 2-5-1 Drift mobility

The mobility of electrons in semiconductors is an important factor in the design of heterojunctions. Drift mobility is used to describe how well electrons and holes move when an electric field applied to a semiconductor.

In a uniform electric field the accelerating charged particles undergo collisions and scattering that alter the velocity of the particles. A particle will appear, over a period of time, to have an average velocity,  $v_{av}$ :

$$v_{av} = \mu E \quad (2.29)$$

where  $E$  is the electric field and  $\mu$  the proportionality constant called the mobility. The drift of both electrons and holes in an electric field will give rise to a combined drift current density, which is given by:

$$J_{drift} = e\sigma E \quad (2.30)$$

where  $\sigma$  is the conductivity defined by:

$$\sigma = (\mu_n n + \mu_p p) \quad (2.31)$$

with  $\mu_n$  and  $\mu_p$  the respective mobilities of the electron (n) and hole (p) concentrations.

In extrinsic semiconductors the conductivity is primarily a function of the majority carrier parameters.

A technique of measuring mobility is the Hall effect, which results from the forces that a moving charge experiences from electric and magnetic fields. The Hall coefficient can be written as:

$$R_H = -\frac{1}{ne} \text{ or } R_H = \frac{1}{pe} \quad (2.32)$$

depending on whether the charge carriers are electrons or holes. The Hall effect provides a practical way of determining whether a semiconductor is n-type or p-type and measuring the concentration of carriers. When combined with a measurement of the conductivity the mobility can also be ascertained. The Hall mobility is defined as the product of the Hall coefficient and the conductivity:

$$\mu_H = |R_H \sigma| \quad (2.33)$$

Hall mobilities are obtained from quantities that are easily measured and have the same dimensions as the drift mobilities.

For electrons and holes the Hall mobilities can be converted into the true drift mobilities using the following equation:

$$\mu_{n(p)} = \mu_{Hn(p)} \left( \frac{\bar{\tau}_{n(p)}^2}{\overline{\tau_{n(p)}^2}} \right) \quad (2.34)$$

The quantity  $\tau$  is the mean free time between the carrier collisions. The quantity  $\bar{\tau}_{n(p)}^2$  over  $\overline{\tau_{n(p)}^2}$  is dependent on the dominant scattering mechanism that exists in the semiconductor. This does not usually deviate far from unity and so the Hall mobility will give a rough indication of the true mobility.

### 2-5-2 Scattering

In the design of quantum well structures it is important to know the various mechanisms that limit the mobility. The movement of electrons will be affected by scattering or collisions. Electrons can suffer collisions from phonons, ionised impurities, alloy disorder, interface roughness, intersubband scattering or chemical impurities<sup>2</sup>. Phonons are quantised lattice waves and their various scattering mechanisms do not change significantly for the 2D case when compared to bulk. Therefore, it is expected that room temperature mobilities of 2D carriers to be comparable to those of 3D when phonon scattering is dominant. Typically a semiconductor contains defects such as impurities and dislocations. The most common defect is due to charged impurities. Since free carriers are generally produced when a shallow impurity is ionised the free carriers will be scattered by the ionised impurities they leave behind. The quality of the interfaces, due to growth techniques, can influence the mobility. Interfaces with a high

amount of roughness will exhibit poor mobilities. Intersubband scattering occurs at high densities when higher-level quantum levels can be populated. This increases the phase space for the final states in scattering events and hence decreases the mobility.

The mobility can be related to the average time between scattering events by:

$$\mu = \frac{e\tau_{sc}}{m^*} \quad (2.35)$$

In semiconductors the most important scattering processes involve the interaction of electrons or holes with lattice vibrations and impurity atoms. At high temperatures or in high purity samples the scattering due to lattice vibrations dominates. At low temperatures or in impure samples it is ionised impurity scattering that dominates<sup>2</sup>.

### 2-5-3 Diffusion

There is a second process that will lead to the movement of carriers within a semiconductor known as diffusion. Diffusion is the process where particles flow from regions of high concentration to those of lower concentrations by way of thermal motion. The resultant diffusion flux is directly proportional to the concentration gradient. The motion of charge results in a diffusion current density, which is related to the spatial gradient of the charge concentration by:

$$J_{diff} = (-)eD_{e(h)} \frac{dn(p)}{dx} \quad (2.36)$$

where  $n$  and  $p$  refer to the electrons and holes and  $x$  denotes the direction of the concentration gradient.  $D_{e(h)}$  is the electron (hole) diffusion coefficient which relates how well the electrons (holes) move due to a density gradient. The total current density will be the addition of the drift and the diffusion.

To convert diffusion coefficient to mobility the Einstein relation is used:

$$\frac{D_e}{\mu_e} = \frac{D_h}{\mu_h} = \frac{kT}{e} \quad (2.37)$$

The mobilities, and consequently the diffusion coefficients, have been shown to be strongly dependent on scattering processes.

#### **2-5-4 Ambipolar diffusion**

When electrons and holes are generated in a semiconductor by a process such as optical excitation the electrons and holes do not move independently of each other. The motion of electrons creates a charge imbalance and a resulting electric field that drags the holes along with them. Therefore, they will diffuse and drift in opposite directions but with the same effective diffusion coefficient. This phenomenon is called ambipolar transport. When an excess population of electrons and holes are generated at a certain point within a semiconductor they will diffuse to cancel any gradient in the carrier concentration. Due to the higher mobility of the electrons when compared to the holes the electrons would be expected to diffuse faster, leaving the holes behind. Since the motion involves charge carriers, any separation of the electrons and holes will lead to the formation of an electric field. This field will tend to slow the motion of the electrons and increase the motion of the holes. The electron and hole distributions will therefore diffuse together with a single effective diffusion coefficient. This diffusion coefficient is called the ambipolar diffusion coefficient and is given as:

$$D_a = \frac{D_e D_h (n+p)}{D_e n + D_h p} \quad (2.38)$$

Generally the electron diffusion coefficient is much greater than the hole diffusion coefficient. Therefore, the ambipolar diffusion coefficient can be approximated as twice the hole diffusion coefficient when  $n = p$ .

## **2-6 Fabrication of quantum wells**

Epitaxial growth methods allow very accurate control of the dimensions of semiconductor materials in the growth direction. It involves starting with a substrate and growing additional layers on top with control at the atomic level. It is important to use techniques that produce high quality crystals with low defect densities.

### **2-6-1 Vapour phase epitaxy (VPE)**

Vapour phase epitaxy involves overgrowth of crystals on a suitable substrate, continuing with the same crystal structure while the composition of the vapour is changed to reflect the desired doping of the layers.

### **2-6-2 Molecular beam epitaxy (MBE)**

Molecular beam epitaxy is a high vacuum technique in which crucibles containing a variety of elemental charges are placed in the growth chamber. The elements contained in the crucibles make up the components of the crystal to be grown as well as the dopants that may be used. When a crucible is heated atoms or molecules of the charge evaporate and these travel in straight paths onto the sample. The sample is heated to allow the atoms to spread and form even layers. The slow growth rate combined with the use of shutters allows the creation of monolayers.

### **2-6-3 Metal organic chemical vapour deposition (MOCVD)**

Metal organic chemical vapour deposition depends on chemical reactions at the substrate surface. A heated substrate sits at an angle in a laminar flow of gas. Radio-frequency inductive heating is used to achieve substrate temperatures comparable to those of MBE growth. The gases that pass over the substrate are a mixture of

**hydrogen as a carrier gas, organometallic precursors of the group elements and the main growth element.**

## 2-7 InGaAs(P)

In general the  $\text{In}_{1-x}\text{Ga}_x\text{As}_y\text{P}_{1-y}$  III-V quaternary has compositions specified by the parameters  $x$  and  $y$  that can independently vary between 0 and 1. The proportions of the constituents are chosen to achieve lattice matching to the substrate, in this case InP. A quaternary system is used to enable the production of compounds that have the correct combination of bandgap energy and lattice constant to construct devices of operational wavelengths at 1.3 or 1.55 microns, Figure 2-6.

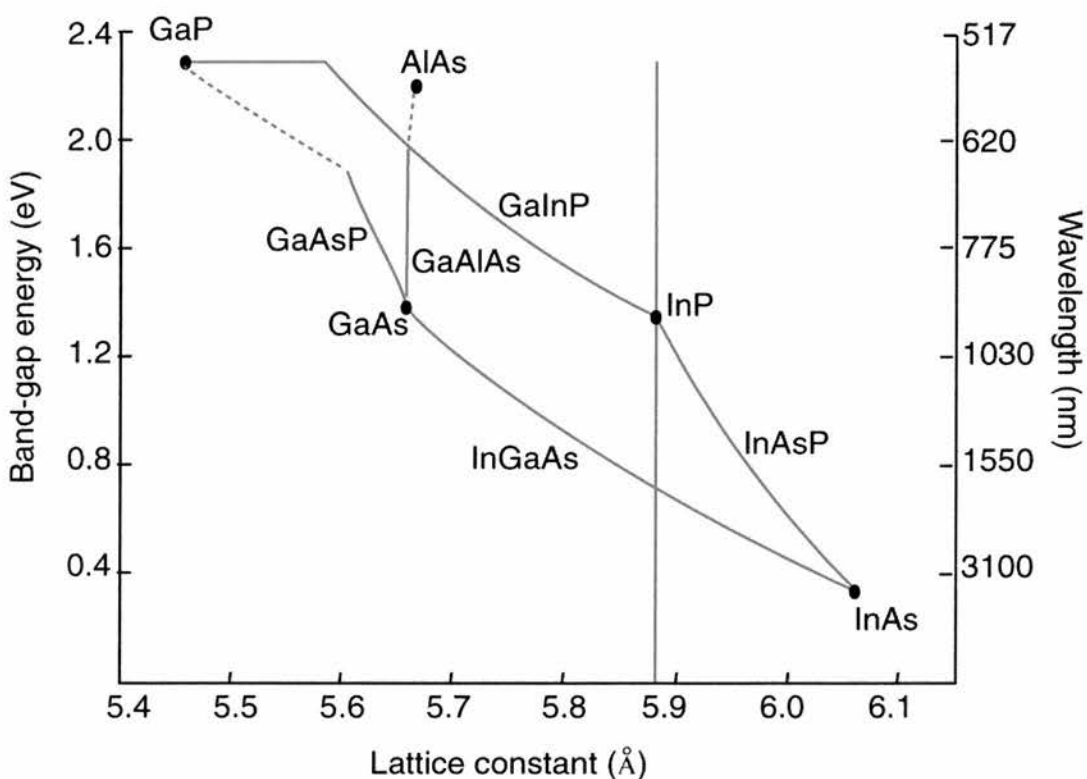
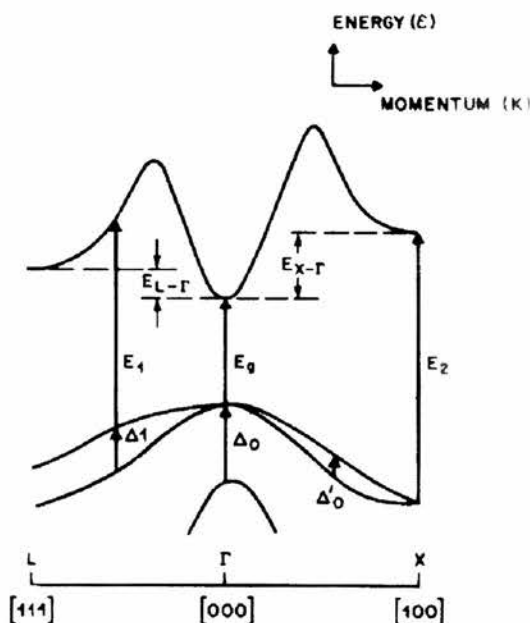


Figure 2-6 Lattice constants and band-gaps for III-V semiconductors at room temperature. The vertical line shows InGaAsP lattice matched to InP.

InP and  $\text{In}_{1-x}\text{Ga}_x\text{As}_y\text{P}_{1-y}$  have cubic zinc blende structures and any compositions that lattice match will be of direct bandgap. InGaAs(P)/InGaAsP is a type I semiconductor quantum well with an offset ratio of 40:60<sup>7</sup>. A typical direct bandgap structure is shown in Figure 2-7 illustrating the variation in electron energy with wavevector along two of the axes of symmetry in the Brillouin zone, [100] and [111]. Also indicated are

the transitions corresponding to critical points in the optical spectra. The region of interest is at the  $\Gamma$  point at the centre of the Brillouin zone. The conduction band is two fold degenerate and the highest valence band four-fold degenerate. Away from the zone centre the valance band splits into two, the heavy hole and light hole bands. There is also a lower valance band, which is split-off from the highest valance band due to the effects of spin-orbit coupling. The band gap is measured as the difference in energy between the conduction band and the highest valance band. The variation of bandgap with composition is illustrated in Figure 2-8<sup>8</sup>.



*Figure 2-7 Typical direct bandgap structure showing the variation in electron energy with wavevector along two of the symmetry axes in the Brillouin zone [100] and [110].*

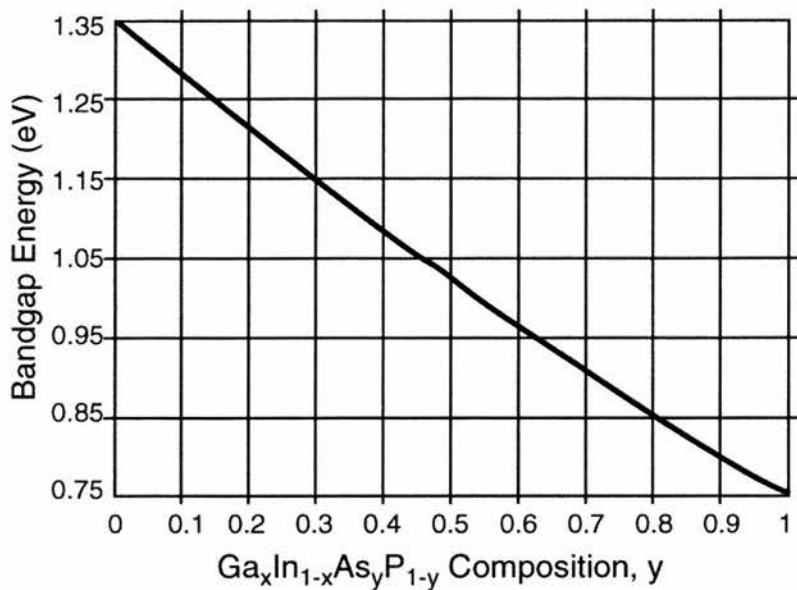


Figure 2-8 Room temperature band-gap of  $\text{Ga}_x\text{In}_{1-x}\text{As}_y\text{P}_{1-y}$  for compositions lattice matched to InP.

**2-8 Bibliography**

- 1 J. M. Luttinger, "Quantum Theory of Cyclotron Resonance in Semiconductors: General Theory," *Phys. Rev.*, **102** (4), pp. 1030-1041, 1956.
- 2 C. Weisbuch, *Quantum Semiconductor Structures* (Academic Press Inc., 1991).
- 3 R. Dingle, W. Wiegmann, and C. H. Henry, "Quantum States of Confined Carriers in Very Thin Al(x)Ga(1-x)As-GaAs-Al(x)Ga(1-x)As Heterostructures," *Phys. Rev. Lett.*, **33** (14), pp. 827-830, 1974.
- 4 S. Hunsche, K. Leo, H. Kurz, and K. Kohler, "Exciton Absorption Saturation by Phase Space Filling: Influence of Carrier Temperature and Density," *Phys. Rev. B*, **49** (23), pp. 16565-16568, 1994.
- 5 S. Schmitt-Rink, D. S. Chemla, and D. A. B. Miller, "Theory of Transient Excitonic Optical Nonlinearities in Semiconductor Quantum Well Structures," *Phys. Rev. B*, **32** (10), pp. 6601-6609, 1985.
- 6 A. Miller, P. Riblet, M. Mazilu, S. White, T. M. Holden, A. R. Cameron, and P. Perozzo, "Exciton saturation in GaAs multiple quantum wells at room temperature," *J. Appl. Phys.*, **86** (7), pp. 3734-3744, 1999.
- 7 R. W. Martin, S. L. Wong, R. J. Nicholas, A. Smith, M. A. Gibbon, E. J. Thrush, and J. P. Stagg, "Band Offsets in Strained InGaAsP/InGaAsP Quantum-Well Optical Modulator Structures," *Journal De Physique IV*, **3** (C5), pp. 327-330, 1993.
- 8 "Handbook of photonics," edited by M. C. Gupta (CRC Press, 1997).

## Chapter 3

# PPLN Optical Parametric Oscillator

### 3-1 Summary

In this chapter the principles behind the optical parametric oscillator (OPO) are outlined. The periodically poled lithium niobate (PPLN) OPO which was built in order to perform time resolved experiments on InGaAs(P) samples in this thesis is detailed. The characteristic procedures to construct this OPO are summarized to aid future researchers.

### 3-2 The Optical Parametric Oscillator

In the past decade synchronously pumped optical parametric oscillators (OPOs) have been greatly developed to produce highly versatile ultrashort laser pulse sources in the near to mid infrared. An OPO is much like a conventional laser, consisting of a resonating cavity and a nonlinear crystal, Figure 3-1. A high power pump wave,  $p$ , is passed through the crystal generating two lower energy waves. These are referred to as the signal wave,  $s$ , for the higher frequency and the idler wave,  $i$ , for the lower frequency.

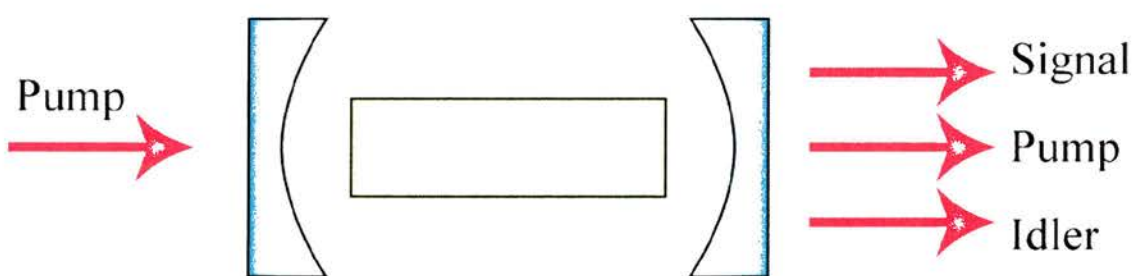


Figure 3-1 Schematic representation of an optical parametric oscillator.

The three waves must obey phase matching conditions to conserve momentum as well as energy:

$$\omega_p = \omega_s + \omega_i \quad (3.1)$$

$$\Delta k = k_p - k_s - k_i \quad (3.2)$$

where  $\omega$  and  $\mathbf{k}$  are the frequencies and wavevectors in the nonlinear crystal.

There are several methods that can be used to change the wavelength of the signal (and idler) wave. The wavelength and temperature dependency of the refractive index of the nonlinear crystal allows the most common methods of tuning by varying the pump wavelength and the crystal temperature. A third method is to change the angle of the crystal with respect to the pump beam, utilising the crystal birefringence.

The generated power and conversion efficiency will depend on the fundamental flux and frequency, crystal length, dispersion and nonlinearity, and the phase mismatch,  $\Delta k l$ , where  $l$  is the length of the crystal.

In order to understand the operation of an OPO we must consider the electric fields of the pump, signal and idler waves. To do this, we first look at the nonlinear relation between the polarisation and the electric field in the crystal and then use Maxwell's equations to determine the three-wave mixing process.

The phase and quasi-phase matched interactions and the physical configuration of the OPO can then be examined.

### **3-2-1 Second order nonlinearity**

When the strength of the electric field interacting with an optical material becomes comparable to the intra-atomic electric field, the relationship between the induced polarisation,  $\mathbf{P}$ , and the electric field strength,  $\mathbf{E}$ , can no longer be only described in terms of the linear susceptibility,  $\chi_1$ . The relationship must be expressed in terms of a power expansion series:

$$\mathbf{P} = \epsilon_0 [\chi_1 \mathbf{E} + \chi_2 \mathbf{E}^2 + \chi_3 \mathbf{E}^3 + \dots] \quad (3.3)$$

The term that is important here is the second order term,  $\chi_2 \mathbf{E}^2$ , which is responsible for the optical parametric generation as well as second harmonic generation and sum/difference frequency mixing.  $\chi_2$ , which is non-zero only in non-centrosymmetric media, is a three dimensional array with 27 elements. It is commonly replaced by the piezoelectric tensor,  $\mathbf{d}$ . These are related by:

$$\chi_{ijk} = \chi_{im} = 2d_{im} \quad (3.4)$$

The order of multiplication of the electric fields is not important. Therefore  $ijk$  can be replaced by  $im$  using the notation,  $11 \rightarrow 2$ ,  $22 \rightarrow 3$ ,  $23=32 \rightarrow 4$ ,  $13=31 \rightarrow 5$ , and  $12=21 \rightarrow 6$ . In the same way,  $im$  can be simplified.

It is possible to reduce the number of coefficients by applying Kleinmann symmetry. This draws on the symmetry of the crystal. The resulting equation is:

$$P_i = d_{\text{eff}} E_j E_k \quad (3.5)$$

where  $d_{\text{eff}}$  is the effective nonlinear coefficient that is used to determine the strength of the nonlinear interaction.

### **3-3 Wave propagation in nonlinear materials and three wave mixing**

The starting point is Maxwell's equations for the macroscopic variables, and in the general case these take the form of Equations (3.6) and (3.7)<sup>1</sup>.

$$\nabla \times \mathbf{E}(t) = -\frac{\partial}{\partial t} \mathbf{B}(t) \quad (3.6)$$

$$\nabla \times \mathbf{H}(t) = \epsilon_0 \frac{\partial}{\partial t} \mathbf{E}(t) + \mathbf{J}(t) \quad (3.7)$$

$\mathbf{J}(t)$  denotes the total volume-current density, which is the sum of the polarisation current,  $\partial\mathbf{P}(t)/\partial t$ , and the conduction current,  $\mathbf{J}_c(t)$ . The latter term is neglected, as we are concerned with induced polarisation in which this plays no part.

By using the following expression:

$$\mathbf{B}(t) = \mu_0 \mathbf{H}(t) \quad (3.8)$$

we can manipulate (3.6) and (3.7) using (3.3) to formulate the wave equation confined to propagation in the z-direction and concerning only the second order polarisation<sup>1</sup>:

$$\nabla \times \nabla \times \mathbf{E} = -\nabla^2 \mathbf{E} + \nabla(\nabla \cdot \mathbf{E}) \quad (3.9)$$

$$\frac{\partial^2 \mathbf{E}(t)}{\partial z^2} = -\frac{1}{c^2} \frac{\partial^2 \mathbf{E}(t)}{\partial t^2} - \mu_0 \frac{\partial^2 (\epsilon_0 \chi^2 \mathbf{E} \cdot \mathbf{E}(t))}{\partial t^2} \quad (3.10)$$

In the case of three wave mixing we achieve the following coupled wave equations by using slowly varying amplitude approximations and assuming that the electric fields are confined to propagation in one dimension:

$$\begin{aligned} \frac{d\mathbf{E}_i(z)}{dz} &= -i(2\omega_i \epsilon_0) \left( \frac{\mu_0}{\epsilon_i} \right)^{1/2} d_{eff} \cdot \mathbf{E}_p(z) \cdot \mathbf{E}_s^*(z) e^{i\Delta kz} \\ \frac{d\mathbf{E}_s(z)}{dz} &= -i(2\omega_s \epsilon_0) \left( \frac{\mu_0}{\epsilon_s} \right)^{1/2} d_{eff} \cdot \mathbf{E}_p(z) \cdot \mathbf{E}_i^*(z) e^{i\Delta kz} \\ \frac{d\mathbf{E}_p(z)}{dz} &= -i(2\omega_p \epsilon_0) \left( \frac{\mu_0}{\epsilon_p} \right)^{1/2} d_{eff} \cdot \mathbf{E}_s(z) \cdot \mathbf{E}_i(z) e^{i\Delta kz} \end{aligned} \quad (3.11)$$

These three equations can be used to analyse any second order nonlinear effect.

### 3-4 Birefringent phase matched interactions in nonlinear materials

The main purpose of an OPO is to enable the production of a tuneable output. There are three commonly used methods to do this. These are angle, temperature and pump

wavelength tuning. All rely on changing the refractive index of the material in the direction of propagation. The parametric generation will be most efficient when we have the perfectly phase matched condition of  $\Delta k=0$ .

As stated previously it is necessary to satisfy the energy conservation equation, Equation (3.1), with the phase matching condition given in Equation (3.2). Applying the fact that  $k=(\lambda/c)n$  and assuming  $\Delta k=0$  allows us to express these in the form:

$$n_3\omega_3 = n_1\omega_1 + n_2\omega_2 \quad (3.12)$$

The refractive index is a frequency dependent quantity therefore different frequencies will travel with different phase velocities,  $c/n$ , within the crystal. However, we can utilise the property of birefringence to compensate for this. Birefringence is when the refractive index of a material is dependent on the direction of propagation and the polarisation of the incident wave. Therefore it is possible to choose the angle of incidence and polarisation of the three waves so that all three will propagate in phase through the medium.

In a biaxial crystal there are three independent refractive indices associated with the axes,  $n_x$ ,  $n_y$  and  $n_z$ .

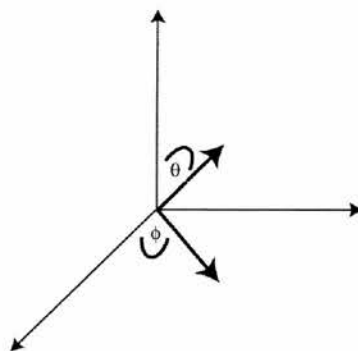


Figure 3-2 Propagation angles in a biaxial crystal

If we consider a wave travelling with direction  $(\theta, \phi)$  as shown in Figure 3-2 then the Fresnel equation for calculating the refractive index in any direction is given by:

$$\frac{\sin^2 \theta \cos^2 \phi}{[n(\theta, \phi)]^{-2} - n_x^{-2}} + \frac{\sin^2 \theta \sin^2 \phi}{[n(\theta, \phi)]^{-2} - n_y^{-2}} + \frac{\cos^2 \theta}{[n(\theta, \phi)]^{-2} - n_z^{-2}} = 0 \quad (3.13)$$

The refractive indices in the x, y and z directions can be found by employing the approximation known as the Sellmeier equation.

### ***3-5 Quasi-phase matched interactions***

Birefringent phase matching is limited by the propagation direction and polarisation combination. There is also the problem of Poynting vector walk-off. This occurs when the Poynting vector of an e-wave moves away from the k-vector when a wave propagates at an angle to the optic axis, whereas those of the o-wave remain collinear. This means that the interaction length is greatly reduced. One way of overcoming these limitations and enabling materials to be designed for operating at specific wavelengths is to use the method of quasi-phase matching (QPM).

When the pump, signal and idler wavelengths propagate collinearly through the crystal but the interaction is not phasematched by birefringence there is still interaction between them as they propagate through the crystal. The waves will slip out of phase and interact less strongly. Back conversion occurs until eventually the phase relation of the waves favour forward conversion and the process repeats itself. Throughout the crystal, the overall conversion efficiency will be negligible and no useful light will be generated, Figure 3-3. The propagation distance after which the gain is reduced by half is the coherence length,  $l_c$ . In quasi-phase matching the sign of the nonlinear coefficient is reversed and the interaction is brought back into phase.

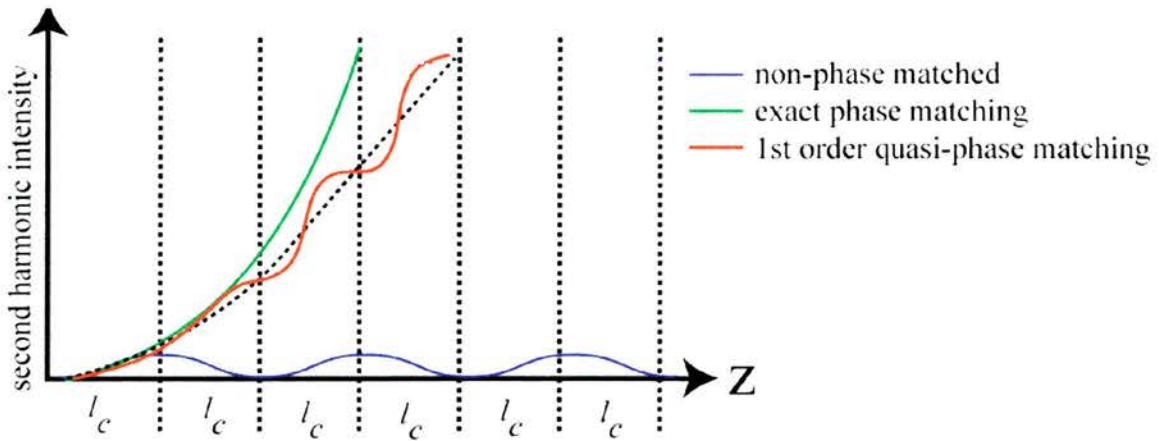


*Figure 3-3 Growth of second harmonic generation through a nonlinear crystal with no phasematching, exact phasematching and quasi-phasematching.*

The wave vector mismatch for the QPM interaction is:

$$\Delta k_Q = k_p - k_s - k_i - \frac{2\pi m}{\Lambda} \quad (3.14)$$

where  $\Lambda$  is the period of modulation within the crystal<sup>3</sup> and  $m$  is the order of the interaction. Quasi phase matching calculations are carried out in the same way as for birefringent phasematching with the inclusion of the grating period factor.

By choosing the appropriate grating period and nonlinear material it is then possible to engineer crystals to allow phasematching for specific systems. The nonlinearity is reversed by periodically poling where the polarity and therefore the nonlinearity is reversed in a ferroelectric crystal by application of an electric field.

The crystal used in this thesis is periodically poled lithium niobate ( $\text{LiNbO}_3$ ), more commonly known as PPLN. To calculate the quasi-phase matching conditions it is critical to know the precise refractive indices throughout the spectral region at various temperatures. Zelmon and Small<sup>4</sup> measured the refractive indices of congruently grown  $\text{LiNbO}_3$  to calculate new Sellmeier equations that accurately predict the refractive indices in the 0.4 to 4 micron regime. Lawrence<sup>5</sup> derived from published data a

temperature dependent Sellmeier equation for the refractive indices from 0.4 to 4.5 microns:

$$n^2 = A_1 + \frac{A_2 + B_1 F}{L^2 - (A_3 + B_2 F)^2} + B_3 F - A_4 L^2 \quad (3.15)$$

with  $L$  the vacuum wavelength in microns and  $F = (T - T_0)(T + T_0 + 546)$ . For  $T = T_0 = 24.5$  the values of the constants are:

$$\begin{aligned} A_1 &= 4.5820 & A_2 &= 0.011775 & A_3 &= 0.21802 & A_4 &= 0.027153 \\ B_1 &= 2.2314 \times 10^{-8} & B_2 &= -2.9671 \times 10^{-8} & B_3 &= 2.1429 \times 10^{-8} \end{aligned}$$

Using this approximation to the refractive index along with the QPM conditions for a specific grating period, tuning curves can be calculated for a PPLN OPO,

### **3-6 Cavity design and focusing**

The mirror reflection coatings in the OPO cavity may be designed to resonate the frequencies  $\omega_s$ ,  $\omega_i$  or both  $\omega_s$  and  $\omega_i$ . We can then also choose whether or not to resonate the pump frequency,  $\omega_p$ .

The most commonly used cavities are singly and doubly resonant resonators (SROs and DROs). These involve resonating the signal or both signal and idler respectively. The SRO case has a higher threshold input power but greater stability. One method that can be used in order to obtain these high input powers is to pump with a mode-locked laser. This will give pulses of high intensity at a constant repetition rate. The optical cavity length of the OPO will then need to match that of the pump laser allowing the resonating pulse to re-meet the pump pulse at the crystal and therefore be amplified on every round trip. Burneika<sup>6</sup> demonstrated the potential of these synchronously pumped OPOs more than two decades ago but there was a lack of suitable nonlinear materials and pump sources. The emergence of new high nonlinearity materials with low damage

thresholds with pump sources of high intensity and good beam quality has enabled synchronously resonant OPOs to become a reliable source of ultrashort near and mid infra-red wavelength pulses.

Several theoretical studies have been conducted into the effects of focusing of the pump and resonating beams. Boyd et al<sup>7</sup> investigated the optimisation of second harmonic and parametric generation by a laser beam in a uniaxial crystal, assuming Gaussian beams and that the confocal parameters,  $b$ , of the pump, signal and idler are set to be equal. The confocal parameter is defined as:

$$b = \frac{2\pi\omega_0^2}{\lambda} \quad (3.16)$$

Defining the focussing parameter,  $\xi$ , to be:

$$\xi = l/b \quad (3.17)$$

where  $l$  is the length of the nonlinear material. Boyd et al found theoretically that the optimum conversion occurred at  $\xi=2.84$  for Gaussian beam profiles.

Fischer et al<sup>8</sup> included birefringence for a cw singly resonant OPO with spherical and hemispherical resonators for both doubly and singularly resonant cases. The results are similar to that of Boyd with  $\xi=2.8$  for a spherical DRO.

If we consider unequal confocal beam parameters then it is found that we can achieve the best operation with the beam parameters of the pump and signal set to different values when diffraction and Poynting vector walk off are taken into account<sup>9</sup>.

### ***3-7 The 1.3 to 1.57 micron PPLN Optical Parametric Oscillator***

The OPO used for conducting time resolved experiments in this thesis was a three mirror synchronously pumped singly resonant standing wave cavity with a folded arm.

This was pumped by 1.8 ps pulses from a self-modelocked Ti-Sapphire laser (Spectra Physics Tsunami) with a tuning range of 700-900nm, pumped with 5W at 532nm from a frequency doubled cw diode-pumped Nd:YVO<sub>4</sub> (Spectra Physics Millennia V). The Ti-Sapphire and OPO cavity lengths were matched giving a repetition rate of the system of 82MHz with pulse duration of 1.5 ps. An isolator was placed after the Ti-Sapphire to prevent any feedback problems from the OPO. A half-wave plate is used to obtain horizontally polarised light from the Ti-Sapphire.

The nonlinear crystal used was periodically poled lithium niobate (PPLN) (Crystal Technology, California) split into eight separate segments with grating periods ranging from 21.0 to 22.4 microns, as illustrated in Figure 3-4. The crystal had dimensions of 11.5 by 5 by 0.5 mm, an antireflection coating at 1.55 microns and was held in a temperature-controlled oven to allow temperature tuning. The OPO operates at 1.5 microns with a pump wavelength of 832nm for a 21.6 micron grating period to 846nm for a 22.4 micron grating period. The calculated and experimental tuning ranges for temperatures 120 to 170 °C for a pump wavelength of 840nm and three grating periods are shown in Figure 3-5. The tuning ranges were calculated from Sellmeier equations and quasi-phase matching conditions.

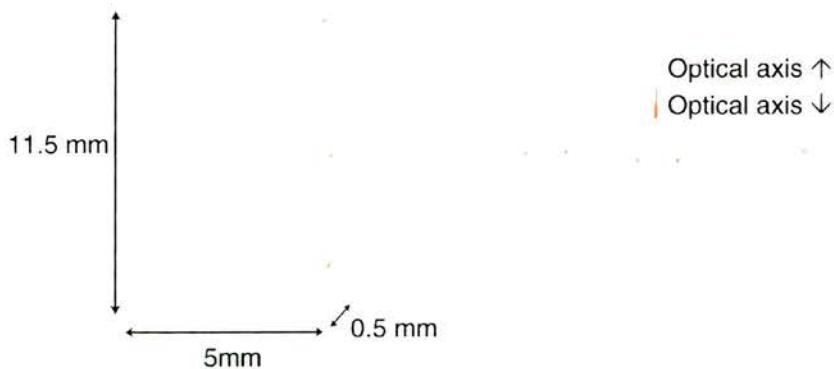


Figure 3-4 Schematic of the PPLN crystal

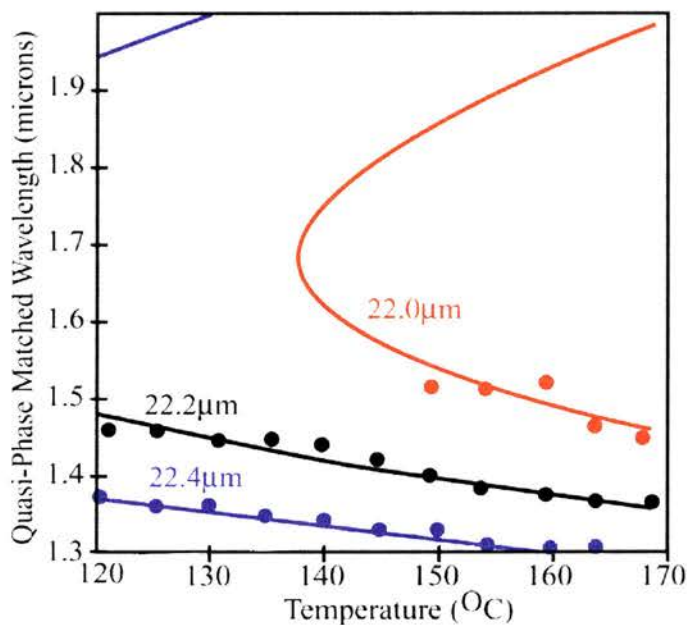


Figure 3-5 Calculated tuning curve and experimental data for grating periods 21.0 to 22.4 microns at a pump wavelength of 840nm.

It was found that extra components outside the OPO resonating cavity were needed to obtain the pump focussing required for high efficiency. A diverging 100mm lens in combination with a converging 60mm lens focused the Ti-Sapphire beam into the crystal giving a beam waist of 18 microns and a focusing parameter of  $\xi=1.5$ . Two highly reflective mirrors of radius 100mm were arranged as shown in Figure 3-6. The distances used between components were L1 to L2 155mm, L2 to M1 40mm, M1 to crystal centre 50mm and crystal centre to M2 100mm. Folding angles were kept to less

than 3 degrees to minimise astigmatism. The output coupler used varied depending on the resonating wavelength and output power required. Reflectivities of 98%, 95%, 87%, 83% and 78% were available with centre reflection wavelength at 1.55 microns.

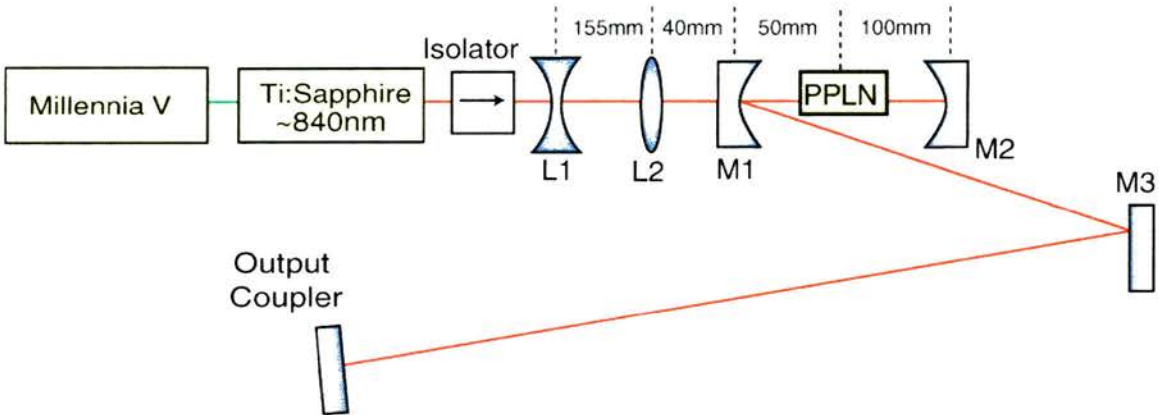


Figure 3-6 PPLN OPO set-up

The OPO was originally pumped with an Argon Ion pumped Ti-Sapphire. The introduction of the Millennia greatly improved the beam quality and stability of the laser. The threshold power for 1.5 micron output reduced from 0.72W with a 97% output coupler to 0.35W when this first pump laser was changed.

The OPO could be temperature or wavelength tuned from 1.3 to 1.57 microns. The reflection coatings of the mirrors and output coupler were the lower limit and degeneracy (signal equal to idler) presented the higher limit. The large  $\Delta k$  of PPLN allows a large amount of tuning by altering the cavity length. With the Millennia as the initial pump, a point of zero dispersion was found at 1.52 microns, which made tuning difficult around this wavelength. It was found that one prism inserted 600mm after M1 resolved this problem by increasing the amount of dispersion within the cavity. Translating the prism to include more or less glass in the optical path could then change this dispersion. The prism also spatially filtered the wavelength to give tuning by adjusting the angle of the output filter.

The OPO was optimised to operate at 1.50 to 1.55 microns with a pump wavelength of 838nm. This was operating in the grating period of 22.0 microns (the third grating period) to avoid the points of degeneracy. This also enabled tuning up and down the grating periods if necessary. Due to the large  $\Delta k$  in PPLN crystals tuning up to 40nm can be achieved through adjusting the cavity length. The wavelength adjusts as the cavity length changes to keep the optical path length the same as for the Ti:Sapphire.

### ***3-8 Alignment of the PPLN OPO***

The first step in aligning the PPLN OPO is to insert the components L1, L2 and M1 (see Figure 3-6) so that the small back-reflection of the Ti-Sapphire pump is directed back along the same path. If the isolator is not accurately set for the Ti-Sapphire wavelength these reflections can cause instability and possible loss of modelocking.

The crystal is then placed in the beam as shown in Figure 3-6. When the Ti-Sapphire laser is modelocked (pulsing) there will be a generation of blue light due to frequency doubling in the crystal. There will be a blue backwards-directed spot that should again be directed along the path of the pump beam as shown in Figure 3-7. The second cavity mirror, M2, is then placed so as to reflect the forwards-directed blue, which is emitted from the PPLN crystal, back through the crystal. There should then be two blue spots on mirror M1. M1 is then angled to direct the two blue spots to the output coupler, passing alongside but not through the PPLN crystal.

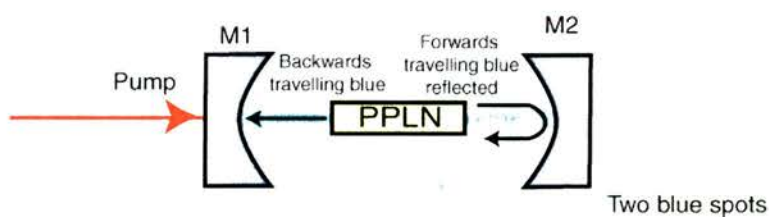


*Figure 3-7 Diagram of the alignment of the blue generation from the PPLN crystal.*

The two blue paths must be collinear. To do this the angles of the PPLN crystal and mirror M2 are altered to ensure the spots are overlapped just after reflection from M1 and at a long distance. The total optical path length is calculated from the repetition rate of the Ti-Sapphire and the output coupler is inserted to approximately equalise this. In practice a third mirror (M3) is used to fold the cavity to allow the cavity to be more compact. The two blue spots are then focussed on the output coupler by translating the crystal and M2.

The blue beam is then sent back along the same path by the use of a small pinhole near M1. The coupler is translated smoothly over a small distance to achieve matching of the OPO and Ti-sapphire cavities. A green flash will be seen when the OPO is generating. The green is due the sum of the pump and the signal from the OPO.

The prism is inserted at the Brewster angle on a translation stage. Whilst the OPO is generating in the cavity that doesn't include the prism, a small part is picked off by the edge of the prism and sent to the new output coupler. This signal is used for alignment and the beam is reflected back along the same path. The prism is then wound fully into the cavity and the original cavity stops generating. The new coupler is translated to obtain length matching to the new optical path. Observing the wavelength spectrum optimises the amount of glass needed in the cavity. This should consist of only one peak will no side band peaks.

Enclosing the OPO in a box to prevent air currents and dust greatly improves the stability and keeps the output power at a constant level.

### 3-9 Autocorrelation measurements

The temporal duration of the pulses from the OPO was measured using autocorrelation techniques. The nonlinear process of second harmonic generation is used to obtain a spatial autocorrelation trace of the optical intensity instead of a direct temporal measurement.

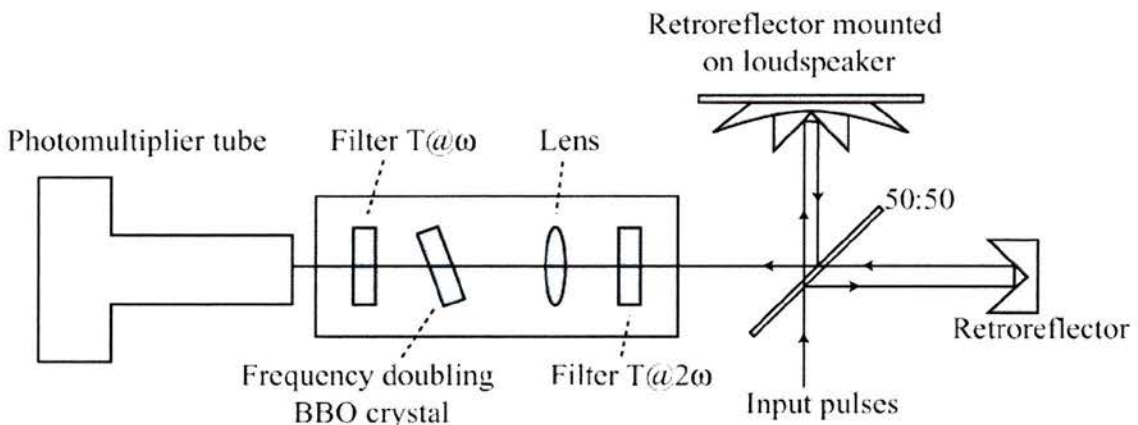


*Figure 3-8 Autocorrelation configuration*

The pulse stream is split into two by a 50:50 beamsplitter in a Michelson-type arrangement. One arm reflects off a stationary retroreflector and the other from a retroreflector mounted on an 8-inch diameter loudspeaker driven by a rounded sawtooth waveform. The two coherent pulse trains are overlapped spatially in the frequency doubling crystal. The loudspeaker translates the retroreflector and therefore varies the temporal difference between the two pulses,  $\Delta\tau$ . When the path lengths are equal ( $\Delta\tau=0$ ) there is a maximum of second harmonic generation. As  $\Delta\tau$  increases the second harmonic signal decreases until there is no overlap between the two pulses and no signal produced. The repetition rate of the speaker is much less than that of the laser so the autocorrelation is made up of many pulses overlapping at varying path differences.

A photomultiplier tube detects the second harmonic signal from the BBO crystal and is output on an oscilloscope.

Translating the stationary retroreflector by a set distance and noting how far the trace moves on the oscilloscope calibrates the autocorrelation trace. This can then be converted to time by dividing by the speed of light. The full width half maximum (FWHM) of the trace,  $\tau_{ac}$ , is related to the actual pulse duration,  $\tau_p$ , by:

$$\tau_p = \frac{\tau_{ac}}{k} \quad (3.18)$$

where the factor k depends on the assumed pulse shape. In the case of a  $\text{sech}^2$  pulse shape this autocorrelation factor is 1.54.

Two autocorrelators were built in order to measure the pulse times from both systems. An example of autocorrelation pulses from the Ti:sapphire laser and the PPLN OPO are shown in Figure 3-9, where the pulses has a widths of 1.8 and 1.5ps respectively, assuming the  $\text{sech}^2$  pulse shape.

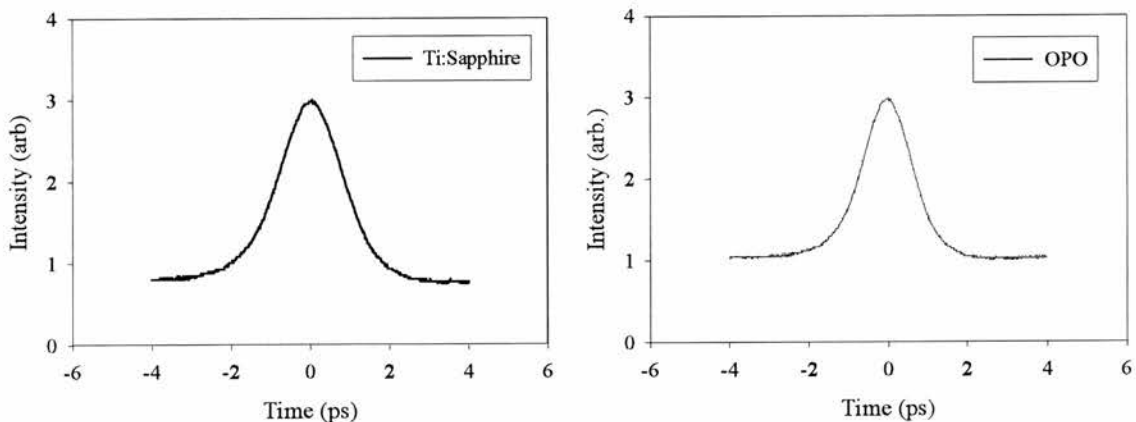


*Figure 3-9 Autocorrelation of a 1.8ps pulse from the Ti:Sapphire laser and 1.5ps pulse from the OPO.*

**3-10 Bibliography**

- 1 P. N. Butcher and D. Cotter, *The elements of nonlinear optics* (Cambridge University Press, 1990).
- 2 Y. J. Ding and J. B. Khurgin, "Second-Harmonic Generation Based on Quasi-Phase Matching: A Novel Configuration," *Optics Lett.*, **21** (18), pp. 1445-1447, 1996.
- 3 L. E. Myers, R. C. Eckardt, M. M. Fejer, R. L. Byer, W. R. Bosenberg, and J. W. Pierce, "Quasi-Phase Matched Optical Parametric Oscillators in Bulk Periodically Poled LiNbO<sub>3</sub>," *J. Opt. Soc. Am. B*, **12** (11), pp. 2102-2116, 1995.
- 4 D. E. Zelmon and D. L. Small, "Infrared Corrected Sellmeier Coefficients for Congruently Grown Lithium Niobate and 5 Mol. % Magnesium Oxide-Doped Lithium Niobate," *J. Opt. Soc. Am. B*, **14** (12), pp. 3319-3322, 1997.
- 5 M. Lawrence, "Short Communication - A Temperature Dependent Dispersion Equation for Congruently Grown Lithium Niobate," *Opt. and Quan. Elect.*, **16** , pp. 373-374, 1984.
- 6 K. Burneika, M. Ignatavichyus, V. Kabelka, A. Piskarskas, and A. Stabinis, "Parametric light amplification and oscillation in KDP with mode-locked pump," *IEEE J. Quantum Electron.*, **8** , pp. 574, 1972.
- 7 G. D. Boyd and D. A. Kleinmann, "Parametric Interaction of Focused Gaussian Light Beams," *J. Appl. Phys.*, **39** (8), pp. 3597-3639, 1968.
- 8 R. Fischer, C. Tran-ba, and L. W. Wieczorek, "Optimal Focusing in a Singly Resonant Optical Parametric Oscillator," *Sov. J. Quantum Electron.*, **7** (12), pp. 1455-1458, 1977.

- 9 S. Guha, F. Wu, and J. Falk, "The Effects of Focusing on Parametric Oscillation," *IEEE J. Quant. Electron.*, **18** (5), pp. 907-912, 1982.

## Chapter 4

# Experimental techniques and sample description

### **4-1 Summary**

The techniques used to study the optical properties of multiple quantum wells are introduced. The InGaAs(P) samples that are investigated in the following chapters of this thesis are detailed. Where available, the absorption spectra are included.

### **4-2 Degenerate time resolved pump probe experiments**

In order to examine the short time scale characteristics of a material we employ a technique whereby one pulse excites the material then a smaller pulse probes the effects. This smaller pulse can be delayed in time by increasing the path difference of the two beams. The experimental set-up to do this is shown in Figure 4-1. A Spectra Physics Ti-Sapphire is pumped by a solid state Millennia V. The Ti-sapphire then pumps a PPLN OPO, which is temperature tuned to produce pulses around 1.5 microns for InGaAsP measurements. The pulses are 1.5 ps duration and the repetition rate of the system is 82MHz, giving a pulse separation of 12ns.

A 50:50 beamsplitter splits the 1.5 micron pulse train into two components, labelled pump and probe. The pump is the beam that is transmitted through the beamsplitter and the probe is reflected at 45 degrees. The path length of one of the arms, in this case the probe, can be varied by a retroreflector mounted on a translation stage. The probe beam is passed along the translation stage, reflected off the retroreflector to a plane mirror. It is then reflected back along its original path, returning off the retroreflector and through the beamsplitter. This fold back on the original path aids in the reduction of walk-off when the translation stage is moved.

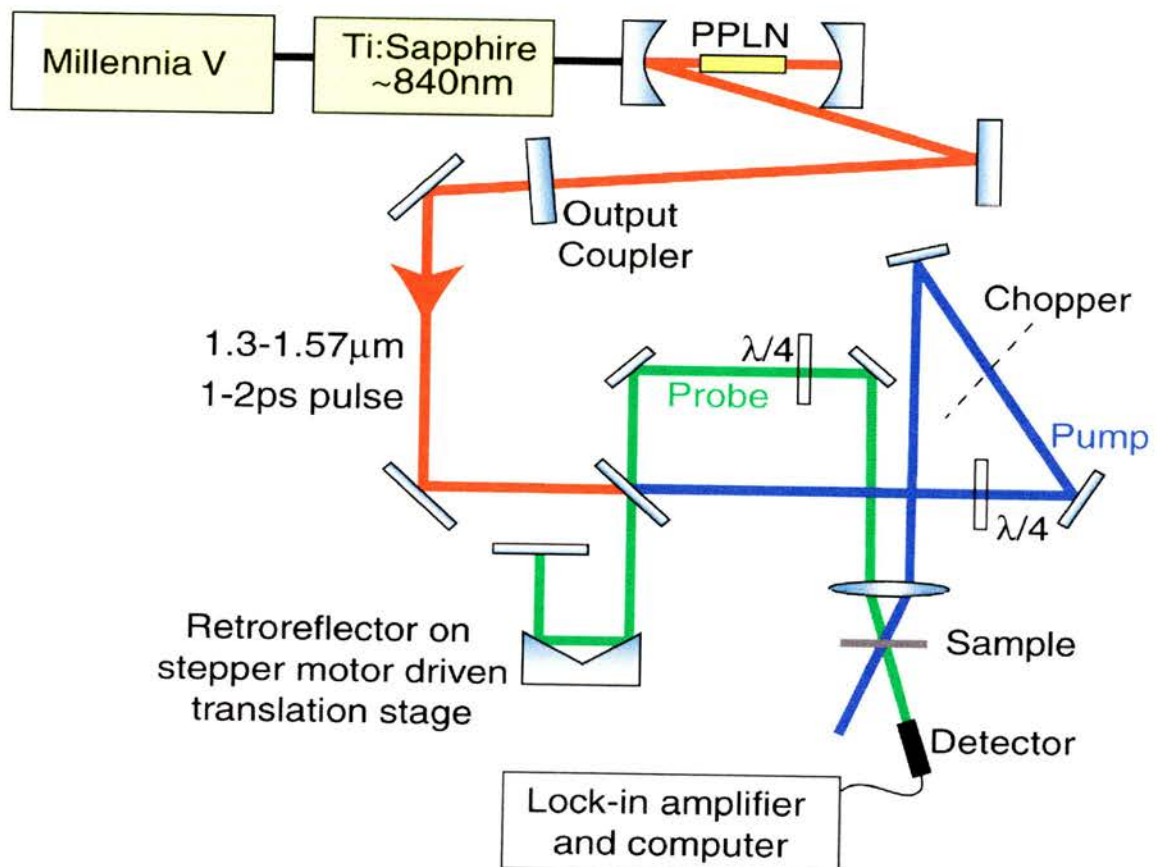


Figure 4-1 Degenerate time resolved pump-probe set-up.

Since there are two reflections off the retroreflector, for each unit the stage moves the path length changes by four units. The probe beam length is set to be equal to the pump when the retroreflector is near the front of the delay stage. To check the walk-off the probe beam is shown on an infrared camera at a long distance after the stage. The stage is translated in both directions and walk-off minimised with the angle of the beamsplitter and the mirror at the end of the stage.

Both arms are aligned parallel then focused on the sample by a single 100mm converging lens. The pump is set to be 1mW and the probe 0.1mW by graded filter wheels.

The pump beam is chopped to allow phase sensitive detection. The modulation is transferred to the probe and the transmitted signal detected by a biased large area germanium photodiode. A digital lock-in amplifier then detects the change in probe signal caused by the pump and a computer records the output data. The translation stage is driven by a stepper motor and controlled by the computer via an IEEE interface card. The transient experiments can then be performed with a computer program that moves the stage in set steps and records and stores the output from the lock-in amplifier at each step.

To optimise the pump-probe signal, the two beams are first overlapped at the focus of the lens. This is done using an infrared camera with no focusing components in the place of the sample (neutral density filters of at least 4ND essential). The detector is placed on the probe beam. Chopping the probe, blocking the pump beam and translating the detector to maximise the signal can achieve optimisation of the detector position.

At this point it is important to check that the detector is not saturating by measuring the response as a function of the probe power. This should be linear in the power regions

that are being used. If neutral density filters are required, it is necessary to angle them in such a way as not to cause multiple reflections or increase the pump scatter into the detector.

Chopping the pump, the translation stage is positioned so that the probe arrives after the pump (after zero delay). The sample is translated through the focus of the beams until there is a rise in the signal. This can then be maximised by small adjustments of the sample, in all directions. The scatter from the pump is blocked as much as possible. The overlap of the pump and probe can then be adjusted by altering the angle of the probe beam after the translation stage in order to tweak up the signal further. Note that if the beams are clipping the sample holder then there will be a large signal from scatter as the sample is translated. To check the scatter signal the probe beam is blocked.

The addition of two quarter-wave plates facilitates spin relaxation measurements. These can be orientated in order to transform the linear polarised OPO output to circular polarised light. To check the orientation, an analyser set parallel to the original signal is placed after the quarter wave plates. The quarter wave plate is rotated until a minimum is found. The addition of a half wave plate enables full rotation of a linearly polarised beam. This system is needed to obtain results in Chapters 6 and 7.

### 4-3 Transient grating studies

The spatial dynamics of excited carriers can be investigated by examining the decay of an optically induced grating. This technique is used to obtain the results in Chapter 8.

Producing an optical grating with the use of two pump beams carries out transient grating studies. The pump beam is split into two. The extra pump beam is reflected off a retroreflector and then focussed onto the sample with the original pump and probe. The two pump beams are overlapped in space and time by performing transient pump-probe scans with each of the pumps separately and moving the new retroreflector until both scans have zero delay in the same place.

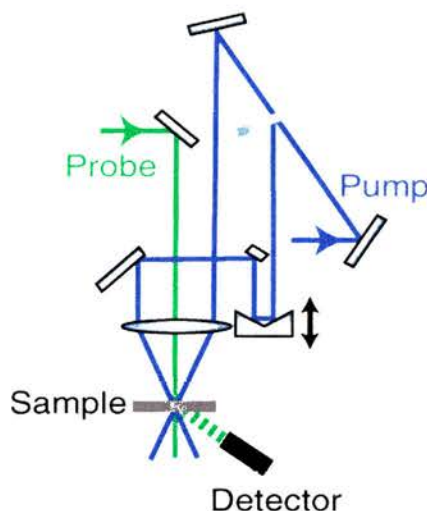


Figure 4-2 Transient grating studies set-up.

With both pump beams of equal intensity incident on the sample the probe is set at zero delay. Chopping the probe, the detector is pin-holed to reduce the signal from the scattered pump and translated around the expected angle of the deflected beam until a signal is found, then maximised. The stage is then moved before zero delay and a transient scan taken.

To perform spin-grating experiments, a half wave plate is inserted to rotate the polarisation of one of the pump beams.

#### **4-4 Time resolved photoluminescence**

Time resolved photoluminescence experiments were performed with apparatus at Heriot Watt University, Edinburgh in conjunction with Dr Gerald Buller and Dr Jason Smith.

Room temperature time resolved photoluminescence measurements of InGaAs(P) can be made using a microscope-based instrument derived from an Edinburgh Instruments Lifemap<sup>1,2</sup>. The excitation source used in these measurements is a passively Q-switched InGaAs laser diode with a variable repetition rate and 10ps pulse duration at 1.3 microns. Excitation was recorded from the 1.5 micron spectral region with wavelength discrimination provided by optical bandpass filters.

The optical system is constructed around a standard infinite-conjugate microscope as shown in Figure 4-3. An optical routing module is inserted into the microscope column in order to allow relaying the laser excitation signal to the sample with minimum attenuation, directing the collected photoluminescence into the single photon avalanche photodiode (SPAD) and splitting a small part of the excitation signal in order to trigger the timing electronics via a second avalanche photodiode. The trigger could also be electronic from the diode.

The optical routing consists of polarising beamsplitter cubes. The upper cube has an operating wavelength of the excitation laser and directs the signal towards the sample. A small component of the initial beam is transmitted through the cube to the trigger photodiode and this provides the start signal for the time-to-amplitude converter (TAC). The TAC produces an output pulse with an amplitude proportional to the time interval between the start and stop inputs. This is then digitised and stored in a multichannel analyser.

The second beamsplitter is broadband coated and the excitation beam passes straight through to the sample via a large numerical aperture microscope objective. The

## Chapter 4              Experimental techniques and sample description

photoluminescence is unpolarised so some of it is reflected to the SPAD, which is biased above breakdown to produce a large avalanche response and is held in a cryostat. The SPAD is operated in a gated active quenching circuit. The photoluminescence is directed to the SPAD via optical fibres.

Disconnecting the optical fibre from the SPAD and directing a laser down this fibre onto the sample achieves alignment. An infrared camera can be positioned in the line of the samples and beamsplitters as shown in Figure 4-3. The excite beam and the alignment laser are overlapped. The fibre is then reconnected onto the SPAD.

The time resolved photoluminescence results are described in Chapter 5.

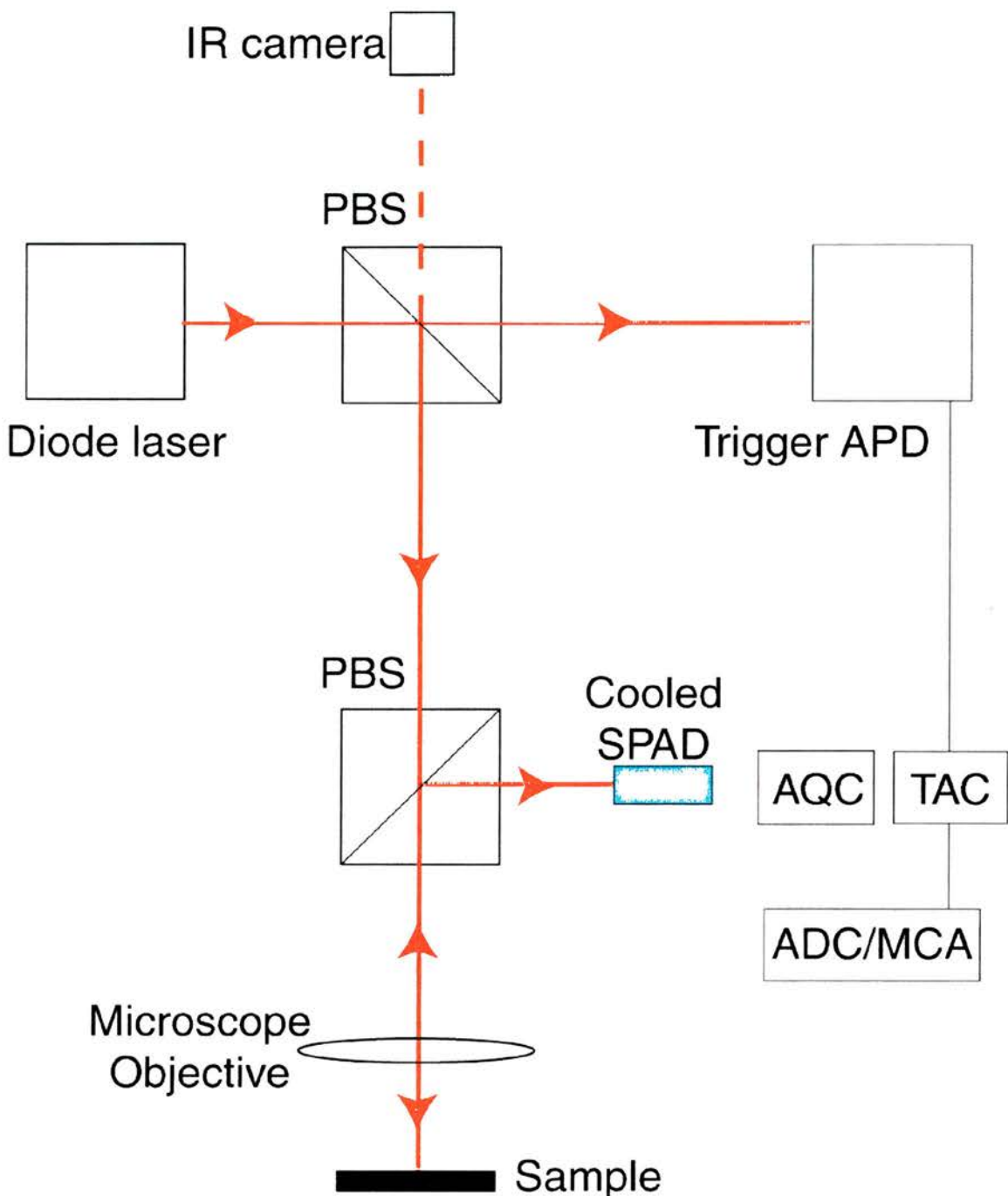


Figure 4-3 Schematic representation of the time resolved photoluminescence set-up.

Polarisation beamsplitters are used to direct the beams. APD is the avalanche photodiode, AQC the active quenching circuit, TAC the time-to-amplitude converter and ADC/MCA the analog-to-digital converter and multichannel analyser.

#### ***4-5 Introduction to the InGaAs(P) samples***

The samples outlined in this chapter and the following chapters are labelled MR534, MR535, MR610, MR611, MR850 and MR1168. Chris Button from the University of Sheffield grew the samples by metalorganic vapour phase epitaxy (MOVPE). They are all p-i-n structures apart from MR1168, which is not intentionally doped.

In this chapter we describe the MQW compositions, well widths and doping concentrations. The energy gaps, electron and hole masses, 1<sup>st</sup> energy levels and transition wavelengths are calculated.

Taking into account that the compositions of the quantum well and barrier layers will not be grown exactly to specification over the whole growth process and the theoretical method uses idealised finite well calculations, the experimental measurement of the exciton peak wavelength is shown to be consistent with the theoretical predictions.

#### ***4-6 Theory for energy calculations***

$\text{In}_{1-x}\text{Ga}_x\text{As}_y(\text{P}_{1-y})$  has a direct bandgap over the full range of lattice matched compounds and the size of the band gap is controlled by the mole fraction, y, using the expression<sup>3</sup>:

$$E_g = 1.35 - 0.72y + 0.12y^2 \quad (4.1)$$

and x is determined by the lattice matching.

Heavy hole and light masses can be calculated from<sup>3</sup>:

$$m_{hh}/m_o = (1-y)[0.79x + 0.45(1-x)] + y[0.45x + 0.4(1-x)] \quad (4.2)$$

and

$$m_h/m_o = (1-y)[0.14x + 0.12(1-x)] + y[0.082x + 0.026(1-x)] \quad (4.3)$$

The electron effective mass can be found from<sup>4</sup>:

$$m_c = 0.080 - 0.039y \quad (4.4)$$

Martin et al<sup>5</sup> evaluated the offset ratio for unstrained InGaAsP as 40:60 ( $\Delta E_c:\Delta E_v$ ).

The energy levels and transitions can then be calculated from graphical solutions to the finite well equations as described in chapter 2.

An overview of the material parameters of InGaAsP has been written by Adachi<sup>6</sup> and the Ioffe Physico Technical Institute website<sup>7</sup> provides information on a range of semiconductor materials.

#### **4-7 Sample MR534**

Sample MR534 consists of 60 periods of 6.5nm  $\text{In}_{0.565}\text{Ga}_{0.435}\text{As}_{0.933}\text{P}_{0.067}$  quantum wells separated by 7.5nm  $\text{In}_{0.869}\text{Ga}_{0.131}\text{As}_{0.287}\text{P}_{0.713}$  barriers. This was grown lattice matched to an InP substrate in a p-i-n structure with doping concentrations of  $3 \times 10^{18} \text{ cm}^{-3}$  in both p and n regions.

This sample was not intentionally doped in the intrinsic region. The heavy hole exciton is experimentally resolved around  $1.530\mu\text{m}$  at room temperature.

The energy gaps of the well and barrier are calculated to be 0.783eV and 1.153eV respectively. This gives an energy gap difference of 0.37eV. The electron, heavy hole and light hole masses for this composition are predicted to be  $0.044m_0$ ,  $0.434m_0$  and  $0.056m_0$ , for the well and  $0.0688m_0$ ,  $0.469m_0$  and  $0.097m_0$  for the barrier, where  $m_0$  is the electron rest mass. This calculation gives the 1<sup>st</sup> energy level of the electron, heavy hole and light hole to be 62meV, 14meV and 65meV and a band edge of 859meV. Assuming an exciton binding energy of 9meV the exciton resonance is 850meV. Therefore the calculated band edge and exciton transitions are  $1.44\mu\text{m}$  and  $1.46\mu\text{m}$  respectively. It is probable that the difference between the calculated and observed values is due to fluctuations in the quaternary compositions during the growth process. An absorption spectra was unavailable for this sample.

#### **4-8 Sample MR535**

Sample MR535 consists of 60 periods of 9.0nm  $\text{In}_{0.565}\text{Ga}_{0.435}\text{As}_{0.933}\text{P}_{0.067}$  quantum wells separated by 7.5nm  $\text{In}_{0.869}\text{Ga}_{0.131}\text{As}_{0.287}\text{P}_{0.713}$  barriers. This was grown lattice matched to an InP substrate in a p-i-n structure with doping concentrations of  $3 \times 10^{18} \text{ cm}^{-3}$ .

This sample was not intentionally doped in the intrinsic region. The heavy hole exciton is resolved around  $1.520\mu\text{m}$  at room temperature.

The energy gaps of the well and barrier are calculated to be 0.783eV and 1.153eV respectively. This gives an energy gap difference of 0.37eV. The electron, heavy hole and light hole masses for this composition are predicted to be  $0.044m_0$ ,  $0.434m_0$  and  $0.056m_0$ , for the well and  $0.0688m_0$ ,  $0.469m_0$  and  $0.097m_0$  for the barrier, where  $m_0$  is the electron rest mass. This calculation gives the 1<sup>st</sup> energy level of the electron, heavy hole and light hole to be 43meV, 8.2meV and 42meV and a band edge of 834meV. Assuming an exciton binding energy of 9meV the exciton resonance is 825meV. Therefore the calculated band edge and exciton transitions will be  $1.49\mu\text{m}$  and  $1.50\mu\text{m}$ . This is in good agreement with the experimental measurement. The slight difference is probably due to growth fluctuations.

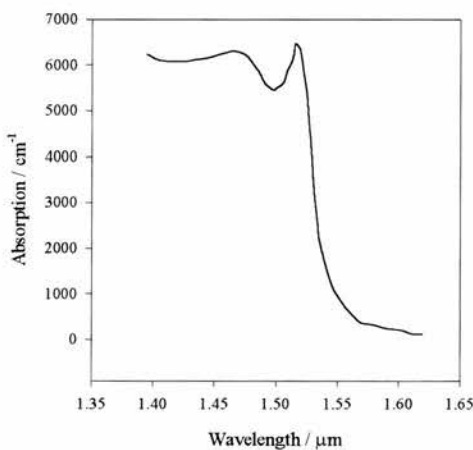


Figure 4-4 Linear absorption as a function of wavelength for sample MR535

#### 4-9 Sample MR610

Sample MR610 consists 500nm of Si doped InP followed by 60 periods of 6.5nm  $\text{In}_{0.53}\text{Ga}_{0.47}\text{As}$  quantum wells separated by 10nm  $\text{In}_{0.869}\text{Ga}_{0.131}\text{As}_{0.287}\text{P}_{0.713}$  barriers, 200nm of InP and 300nm of Zn doped InP. This is a p-i-n structure with doping

concentrations of  $3 \times 10^{18} \text{ cm}^{-3}$ . The heavy hole exciton is resolved around  $1.540 \mu\text{m}$  at room temperature.

The calculated energy gaps of the well and barrier are  $0.75\text{eV}$  and  $1.153\text{eV}$  respectively. This gives an energy gap difference of  $0.403\text{eV}$ . The predicted electron, heavy hole and light hole masses are  $0.041m_0$ ,  $0.424m_0$  and  $0.052m_0$ , for the well and  $0.0688m_0$ ,  $0.469m_0$  and  $0.097m_0$  for the barrier, where  $m_0$  is the electron rest mass. This calculation gives the 1<sup>st</sup> energy level of the electron, heavy hole and light hole to be  $67\text{meV}$ ,  $14.8\text{meV}$  and  $69.5\text{meV}$  and a band edge of  $832\text{meV}$ . Assuming an exciton binding energy of  $9\text{meV}$  the exciton resonance is  $821\text{meV}$ . Therefore the calculated band edge and exciton transitions will be  $1.49\mu\text{m}$  and  $1.51\mu\text{m}$  respectively. This is in good agreement with the experimental measurement. The slight difference is probably due to growth fluctuations.

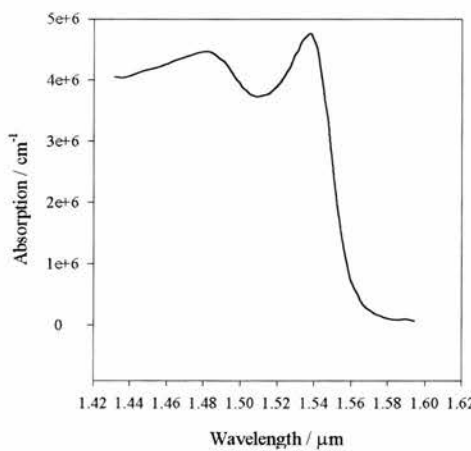


Figure 4-5 Linear absorption as a function of wavelength for sample MR610

#### 4-10 Sample MR611

Sample MR611 consists 500nm of Si doped InP followed by 60 periods of 5.5nm  $\text{In}_{0.53}\text{Ga}_{0.47}\text{As}$  quantum wells separated by 10nm  $\text{In}_{0.869}\text{Ga}_{0.131}\text{As}_{0.287}\text{P}_{0.713}$  barriers,

200nm of InP and 300nm of Zn doped InP. This is a p-i-n structure with doping concentrations of  $3 \times 10^{18} \text{ cm}^{-3}$ . The heavy hole exciton is resolved around  $1.510 \mu\text{m}$  at room temperature.

The calculated energy gaps of the well and barrier are 0.75eV and 1.153eV respectively. This gives an energy gap difference of 0.403eV. The predicted electron, heavy hole and light hole masses are  $0.041m_0$ ,  $0.424m_0$  and  $0.052m_0$ , for the well and  $0.0688m_0$ ,  $0.469m_0$  and  $0.097m_0$  for the barrier, where  $m_0$  is the electron rest mass. This calculation gives the 1<sup>st</sup> energy level of the electron, heavy hole and light hole to be 78meV, 19.6meV and 85meV and a band edge of 848meV. Assuming an exciton binding energy of 9meV the exciton resonance is 839meV. Therefore the calculated band edge and exciton transitions will be  $1.46 \mu\text{m}$  and  $1.48 \mu\text{m}$  respectively. The slight difference is probably due to growth fluctuations.

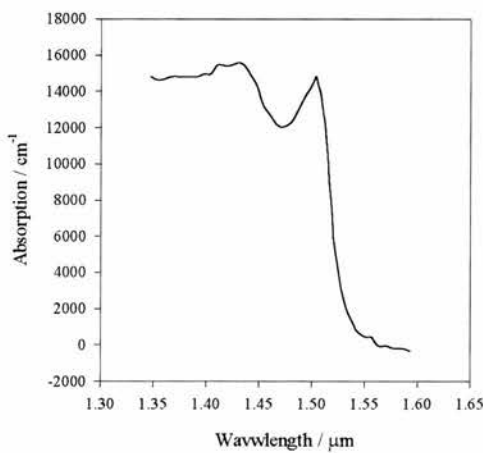


Figure 4-6 Linear absorption as a function of wavelength for sample MR611

#### **4-11 Sample MR850**

Sample MR850 consists of a 2 $\mu\text{m}$  Si doped InP buffer layer followed by 60 periods of 9.5nm  $\text{In}_{0.565}\text{Ga}_{0.435}\text{As}_{0.933}\text{P}_{0.067}$  quantum wells separated by 7.5nm  $\text{In}_{0.869}\text{Ga}_{0.131}\text{As}_{0.287}\text{P}_{0.713}$  barriers. On top of this are 200nm of InP then 300nm of Zn doped InP. Seven periods of 114.2nm  $\text{In}_{0.696}\text{Ga}_{0.304}\text{As}_{0.658}\text{P}_{0.341}$  doped with  $2 \times 10^{18} \text{ cm}^{-3}$  Zn and 122.3nm Zn doped InP, creating an antireflection stack. All the InP doping concentrations are  $3 \times 10^{18} \text{ cm}^{-3}$ .

The substrate is grown on axis (100) and is composed of InP(Fe) misorientated at 0.35 degrees off to (110) and InP(S) misorientated at 0.35 degrees off to (110). The heavy hole exciton is resolved around 1.510 $\mu\text{m}$  at room temperature.

The calculated energy gaps of the well and barrier are 0.783eV and 1.153eV respectively. This gives an energy gap difference of 0.37eV. The predicted electron, heavy hole and light hole masses are  $0.044m_0$ ,  $0.434m_0$  and  $0.056m_0$ , for the well and  $0.0688m_0$ ,  $0.469m_0$  and  $0.097m_0$  for the barrier, where  $m_0$  is the electron rest mass. This calculation gives the 1<sup>st</sup> energy level of the electron, heavy hole and light hole to be 40.4meV, 7.5meV and 39.2meV and a band edge of 831meV. Assuming an exciton binding energy of 9meV the exciton resonance is 822meV. Therefore the calculated band edge and exciton transitions will be 1.49 $\mu\text{m}$  and 1.51 $\mu\text{m}$  respectively.

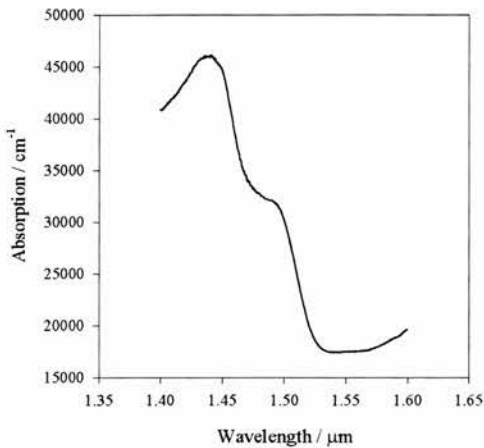


Figure 4-7 Linear absorption as a function of wavelength for sample MR850

#### 4-12 Sample MR1168

Sample MR1168 consists of 60 periods of 10nm  $\text{In}_{0.565}\text{Ga}_{0.435}\text{As}_{0.933}\text{P}_{0.067}$  quantum wells separated by 7nm  $\text{In}_{0.869}\text{Ga}_{0.131}\text{As}_{0.287}\text{P}_{0.713}$  barriers. This is surrounded by 500nm and 250nm of InP.

The substrate is grown on axis (100) and is composed of InP(S) misorientated at 0.35 degrees off to (110) and InP(Zn) misorientated at 0.2 degrees off to (110). This sample was not intentionally doped. The heavy hole exciton is resolved around  $1.525\mu\text{m}$  at room temperature.

The calculated energy gaps of the well and barrier are 0.783eV and 1.153eV respectively. This gives an energy gap difference of 0.37eV. The predicted electron, heavy hole and light hole masses are  $0.044m_0$ ,  $0.434m_0$  and  $0.056m_0$ , for the well and  $0.0688m_0$ ,  $0.469m_0$  and  $0.097m_0$  for the barrier, where  $m_0$  is the electron rest mass. This calculation gives the 1<sup>st</sup> energy level of the electron, heavy hole and light hole to be 37.8meV, 6.8meV and 36.5meV and a band edge of 828meV. Assuming an exciton

binding energy of 9meV the exciton resonance is 821meV. Therefore the calculated band edge and exciton transitions will be  $1.498\mu\text{m}$  and  $1.515\mu\text{m}$  respectively. The slight difference in experimental and theoretical values of the exciton resonance is probably due to growth fluctuations. An absorption spectra was unavailable for this sample.

**4-13 References**

- 1 S. J. Fancey, G. S. Buller, J. S. Massa, A. C. Walker, C. J. McLean, A. McKee, A. C. Bryce, J. H. Marsh, and R. M. D. L. Rue, "Time-resolved photoluminescence microscopy of GaInAs/GaInAsP quantum wells intermixed using a pulsed laser technique," *J. Appl. Phys.*, **79** (12), pp. 9390-9392, 1996.
- 2 G. S. Buller, J. S. Massa, and A. C. Walker, "All-solid-state microscope-based system for picosecond time-resolved photoluminescence measurements in II-V semiconductors," *Rev. Scient. Instrum.*, **63** (5), pp. 2994-2998, 1992.
- 3 N. K. Dutta, "Calculated absorption, emission, and gain in  $\text{In}_{0.72}\text{Ga}_{0.28}\text{As}_{0.6}\text{P}_{0.4}$ ," *J. Appl. Phys.*, **51** (12), pp. 6095-6100, 1980.
- 4 R. J. Nicholas, S. J. Sessions, and J. C. Portal, *Appl. Phys. Lett.*, **37**, pp. 178, 1980.
- 5 R. W. Martin, S. L. Wong, R. J. Nicholas, A. Smith, M. A. Gibbon, E. J. Thrush, and J. P. Stagg, "Band Offsets in Strained InGaAsP/InGaAsP Quantum-Well Optical Modulator Structures," *Journal De Physique Iv*, **3** (C5), pp. 327-330, 1993.
- 6 S. Adachi, "Material Parameters of  $\text{In}_{1-x}\text{Ga}_x\text{As}_y\text{P}_{1-y}$  and Related Binaries," *Journal of Applied Physics*, **53** (12), pp. 8775-8792, 1982.
- 7 G. Zegrya, (Ioffe Physico Technical Institute, St Petersburg,  
<http://www.ioffe.rssi.ru/SVA/NSM/index.html>).

# Chapter 5

## Carrier Lifetime

### ***5-1 Summary***

In this chapter the carrier lifetime is measured in InGaAsP MQW structures by time resolved photoluminescence. The carrier lifetime was found to be too long to study with pump-probe techniques given the pulse repetition rate of the laser. Carrier sweep-out effects in the p-i-n structures are discussed.

### ***5-2 Introduction***

For the interpretation of the experimental results outlined in the later chapters of this thesis it is important to know the carrier lifetime of the samples.

The carrier lifetime is a fundamental property of semiconductor materials and is of critical importance for the operation of optoelectronic devices. There are two types of carrier relaxation ( $\tau_C$ ), non-radiative ( $\tau_{NR}$ ) and radiative ( $\tau_R$ ), which contribute to the overall carrier lifetime, equation (5.1). Non-radiative decays include processes such as impurities, lattice defects, interface traps and Auger recombination. The term Shockley-Read recombination is used to denote the mechanism of recombination through trapping, where a trap is caused by a foreign atom or structural defect and is assumed to have an energy level in the energy gap. The overall carrier relaxation rate will be a sum of the radiative and non-radiative decays:

$$\frac{1}{\tau_C} = \frac{1}{\tau_{NR}} + \frac{1}{\tau_R} \quad (5.1)$$

Free carriers can also be removed from the wells in an electric field through thermionic emission and tunnelling.

To measure the radiative decay rate, time resolved photoluminescence experiments were performed. This technique optically excited carriers high into the band, followed by relaxation to the n=1 level via intersubband transitions. The radiative decay from the n=1 level is measured by recording the emitted luminescence at the band-gap energy using photon counting techniques.

### **5-3 Shockley-Read recombination**

Shockley-Read recombination is based on the recombination of electrons and holes in semiconductors through the mechanism of trapping<sup>1</sup>. A trap is assumed to have an energy level in the energy gap so that its charge may have either of the two values differing by one electronic charge.

The Shockley-Read recombination rate for a single recombination level is given by:

$$R = \frac{b_n b_p (np - n_0 p_0)}{b_n (n + n_1) + b_p (p + p_1)} N \quad (5.2)$$

where  $b_n$  and  $b_p$  are rate coefficients for the capture of electrons and holes respectively,  $n_1$  and  $p_1$  are the carrier concentrations that would arise if the Fermi level were coincident with the trap level.  $N$  is effective bulk density of recombination centres for a quantum well of thickness  $L$ . For low-level injection ( $p \approx p_0$ ) this becomes  $R \approx b_n N \Delta n$ , where  $\Delta n$  is the excess minority carrier concentration, and for high-level injection, as in our case, ( $n \gg n_0, p \gg p_0, n \approx p, \Delta n \approx \Delta p$ )  $R \approx \frac{\Delta n N b_n b_p}{(b_n + b_p)}$ . In both cases the carrier decay is exponential.

### **5-4 Radiative Recombination**

At room temperature in quantum wells, because essentially all of the excitons are ionised because of the small binding energy of the exciton, free carriers will dominate the radiative recombination.

Band-to-band recombination occurs when an electron falls from its state in the conduction band into the empty state in the valence band, which is associated with the hole. A photon is released with energy equal to the difference between the initial and final energy states of the electron. The radiative recombination coefficient,  $B$ , will depend on the density of the carriers present. The recombination rate due to radiative recombination alone can be expressed as:

$$\frac{1}{\tau} = B(n)n \quad (5.3)$$

Wintner and Ippen<sup>2</sup> calculated the coefficients for 1.55 micron band-gap bulk InGaAsP and found  $B = 1.0 \times 10^{-10} \text{ cm}^3 / \text{s}$ . This radiative decay is a bimolecular process that will result in a non-exponential decay.

### **5-5 Auger recombination**

Auger recombination is a form of non-radiative recombination where an electron and hole recombine and the excess energy is transferred to either an electron or a hole. Consider an initial state of two electrons and one hole. After scattering an electron hole pair is annihilated and the remaining electron is excited to a hot state such as to conserve energy and momentum. Another situation is where one electron and two holes interact to produce a hot hole in either the split off band or the light hole band. These processes are illustrated in Figure 5-1. The Auger rates increase exponentially as the bandgap is decreased. They also increase exponentially as the temperature increases.

These are direct results of the energy and momentum conservation and the carrier statistics. Auger processes do not play much of a role in semiconductors with large band gaps such as GaAs. However in narrower bandgap materials like InGaAsP Auger recombination can become very important at laser carrier densities and can limit the emission from long wavelength semiconductor laser system.

In the absence of recombination at defects and surfaces the carrier lifetime,  $\tau$ , can be written in terms of a radiative recombination coefficient,  $B(n)$ , and an Auger coefficient,  $C$ , as shown in equation (5.4)<sup>3</sup>.

$$\frac{1}{\tau} = B(n)n + Cn^2 \quad (5.4)$$

Wintner and Ippen<sup>2</sup> calculated these two coefficients for 1.55 micron InGaAsP and found  $B = 1.0 \times 10^{-10} \text{ cm}^3/\text{s}$  and  $C = 7.5 \times 10^{-29} \text{ cm}^6/\text{s}$ . The 3D carrier density dependence for these values is plotted in Figure 5-2. The decay times are equal for a carrier density of  $10^{18} \text{ cm}^{-3}$  with a decay time of 13ns. A carrier density above this will result in the observation of Auger recombination. We do not expect to reach these carrier densities, as discussed in section 5-9.

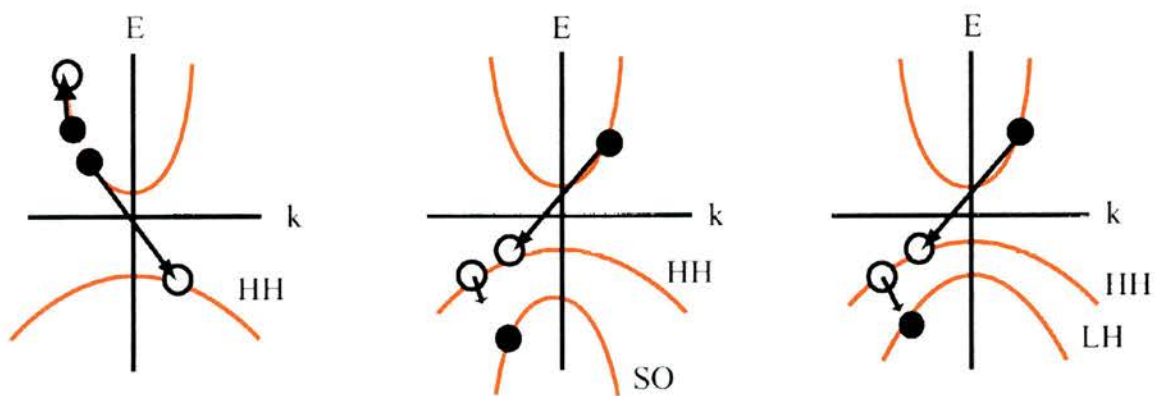


Figure 5-1 Main Auger recombination processes.

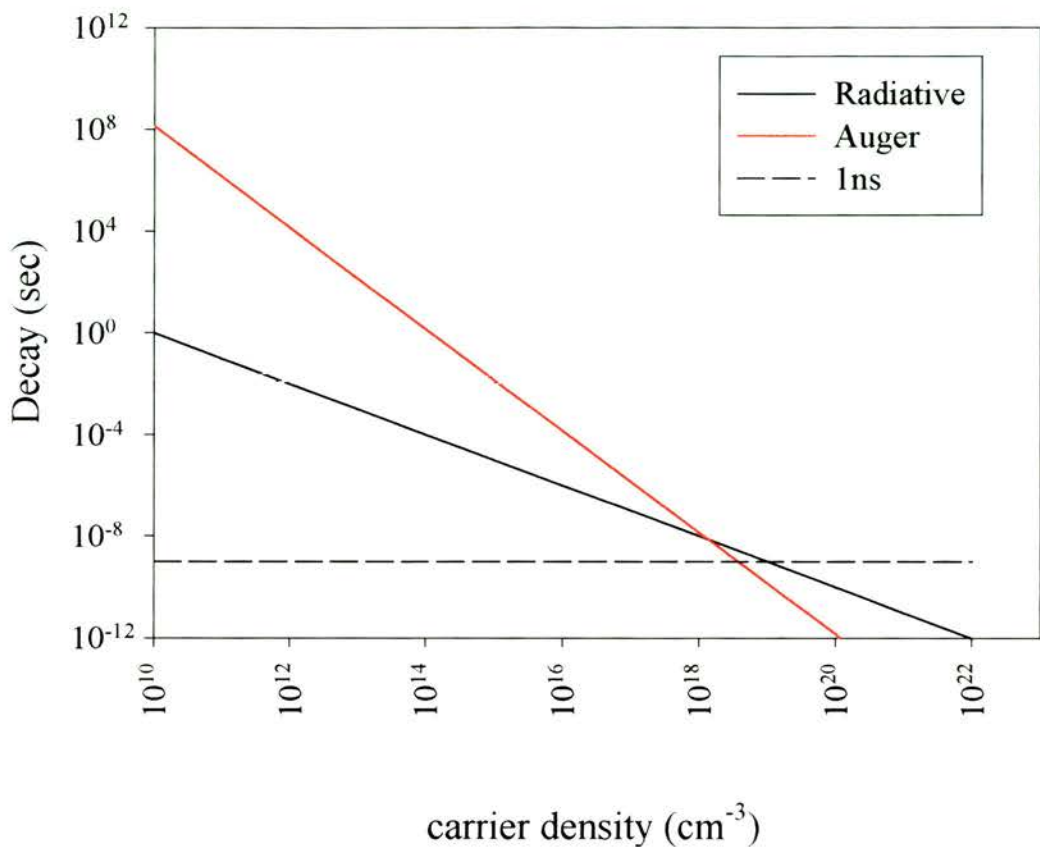


Figure 5-2 Radiative and Auger carrier lifetime as a function of carrier density.

### 5-6 Thermionic emission and tunnelling

After optical excitation, a thermalised distribution results very rapidly by carrier-carrier scattering with no net energy change. Some carriers in the distribution will be “hot” with energies above the top of the well. If there is a field across the wells created by a p-i-n structure then the carriers above the barrier height will be swept out towards the electrodes. The theory of thermionic emission can be adapted for quantum well structures to give an emission time of:

$$\tau_{th} = \left( \frac{2\pi m^* L^2}{kT} \right)^{1/2} \exp \left( \frac{E_b - E - eF \cdot L/2}{kT} \right) \quad (5.5)$$

where  $m^*$  is the effective mass,  $L$  the well width,  $kT$  the Boltzmann factor,  $E_b$  the barrier height,  $E$  the energy of the bound state and  $F$  the electric field across the well. For the InGaAsP samples in this thesis the thermonic emission times for electrons are calculated to be 10s of picoseconds and for the holes around 50 nanoseconds.

Carriers can also escape from the wells by tunnelling through the barriers when a field is present. The quantum tunnelling time across a potential barrier  $V$  is given by<sup>4</sup>:

$$\tau_T = k \exp \left( -\frac{4}{3hF} \sqrt{2m} \left[ (V - E - Fb)^{3/2} - (V - E)^{1/2} \right] \right) \quad (5.6)$$

where  $b$  is the barrier width.

Cavailles et al<sup>5</sup> measured both electron and hole escape times from a GaAs-AlGaAs quantum well in an electric field at room temperature and concluded that non-resonant tunnelling was a small component compared to thermonic emission and recombination. Thermally activated tunnelling may be possible.

### **5-7 Experimental set-up**

It was found that the carrier lifetime could not be measured with the Ti-Sapphire pumped OPO. Carriers were still present in the wells at 12ns, the repetition time of the laser system, so there occurred a large signal in the pump-probe scans before the ‘zero delay’ position.

Therefore, time resolved photoluminescence techniques were used. These experiments were carried out at Heriot Watt University, where the apparatus was designed and operated by Jason Smith and Gerald Buller.

The experimental set up is outlined in chapter 4. Originally a laser diode source of 750nm was used to excite the carriers. However it was found that this resulted in absorption into the barriers with no relaxation to the bottom of the wells before recombination. Therefore, a signal could not be obtained at 1.5 microns. The excitation was changed to a 1.3 micron Q-switched InGaAsP laser diode with 10ps pulse width and pulse energy of 4pJ at a repetition rate of 1kHz. This excites carriers below the bandgap of the barriers, to obtain photoluminescence at 1.5 microns. Only wavelengths between 1.5 and 1.55 microns were transmitted to the detector by use of optical bandpass filters.

The single photon detection system incorporated an InGaAs avalanche photodiode detector held in a cryostat at 77K. This was operated slightly below the breakdown voltage of 29V. In order to be sensitive to the excitation wavelength and measure the instrumental response bandpass filters were removed from the system. In this case neutral density filters must be used to prevent saturation of the detector.

The instrumental response is shown in Figure 5-3. A low dark noise count was achievable with the system described in Chapter 4 by cooling the detector to 77K. The

resolution was measured at 330ps at this temperature, which allowed a good trade-off between acquisition time and noise.

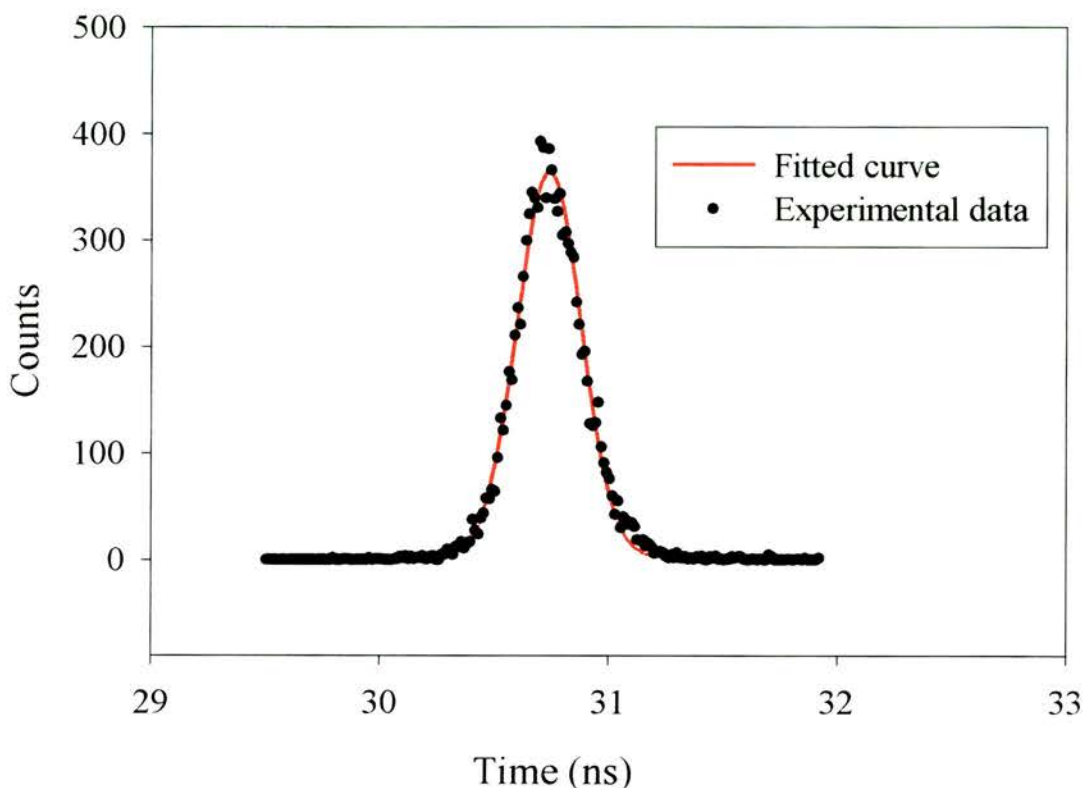


Figure 5-3 Instrumental response of the InGaAs detector. The fitted curve is a

$$\text{Gaussian, } y = 2.4 + 362 \exp\left(-5\left(\frac{x-30.7}{0.139}\right)^2\right)$$

**5-8 Result for sample MR1168 (undoped)**

The result of the time resolved photoluminescence for the undoped sample, MR1168, at room temperature is shown, plotted on a logarithmic scale, in Figure 5-4. Note the very long recovery time. This is much larger than typical values in GaAs materials. This indicates a good quality material for light emitting devices.

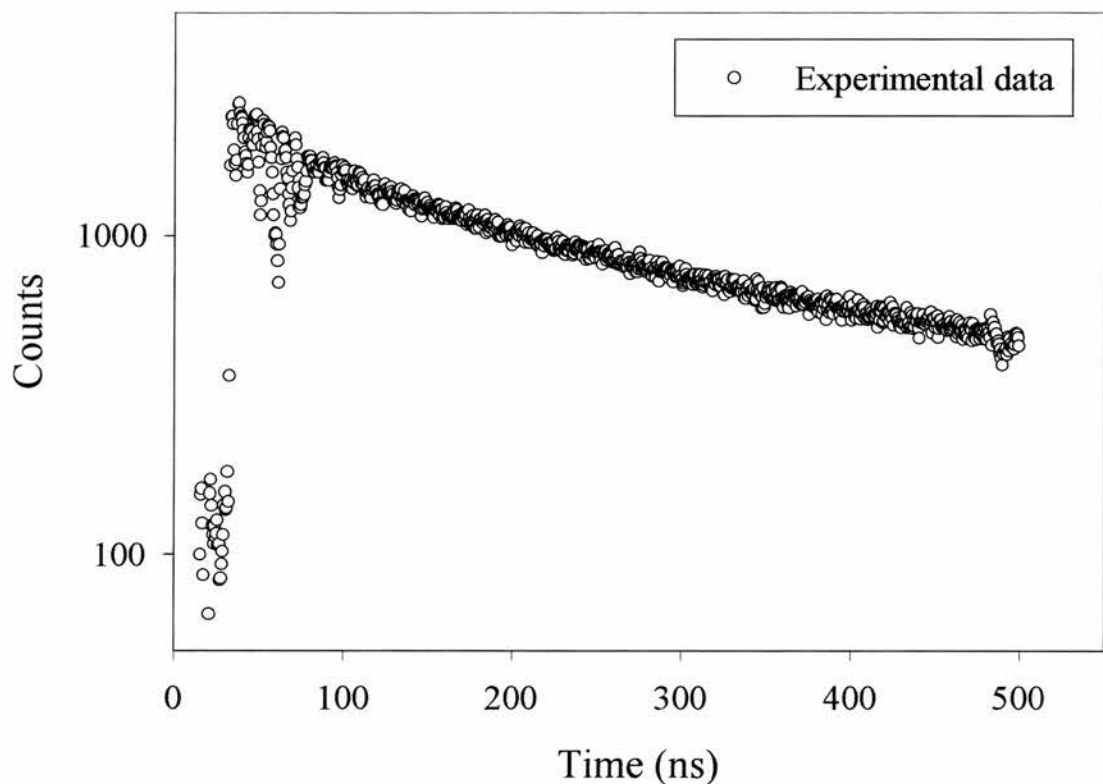


Figure 5-4 Photoluminescence decay for sample MR1168.

### 5-9 Discussion for MR1168 (undoped)

The result of the undoped sample as shown in Figure 5-4 does not exhibit a clear exponential decay. The 1/e point occurs at 220ns, which was found to slightly change spatially across the sample. There is no evidence of any interface recombination or thermonic emission, which would have exponential decays.

Bimolecular or Auger recombination could have a significant role in the lifetime. Therefore the time resolved photoluminescence decay for MR1168 was fitted with both an Auger and a biomolecular form of decay, as described in equation (5.4). These are shown in Figure 5-5.

The Auger decay does not fit the experimental data. However, the bimolecular decay provides a good theoretical fit. From Figure 5-2 it can be seen that for carrier densities less than  $10^{18} \text{ cm}^{-3}$  radiative decay is predicted to be dominant over Auger recombination.

The 1.3 micron excite laser delivers pulse energy of 4pJ to a 30 micron FWHM spot size. With the assumption that the absorption coefficient is  $10^4 \text{ cm}^{-1}$ , this gives an estimated carrier density of  $3.6 \times 10^{16} \text{ cm}^{-3}$ . Equation(5.3) is used to calculate the coefficient  $B$ .

$$3.6 \times 10^{16} = 1 / (B \times 2.20 \times 10^{-7}) \quad (5.7)$$

This gives  $B$  on the order of  $1 \times 10^{-10} \text{ cm}^3/\text{s}$ . Wintner and Ippen<sup>2</sup> calculated the coefficients for 1.55 micron InGaAsP and found  $B = 1.0 \times 10^{-10} \text{ cm}^3/\text{s}$ . The TRPL experimental result agrees well with the previously measured value.

Therefore the mechanism that governs the recombination in this sample is most likely to be radiative decay.

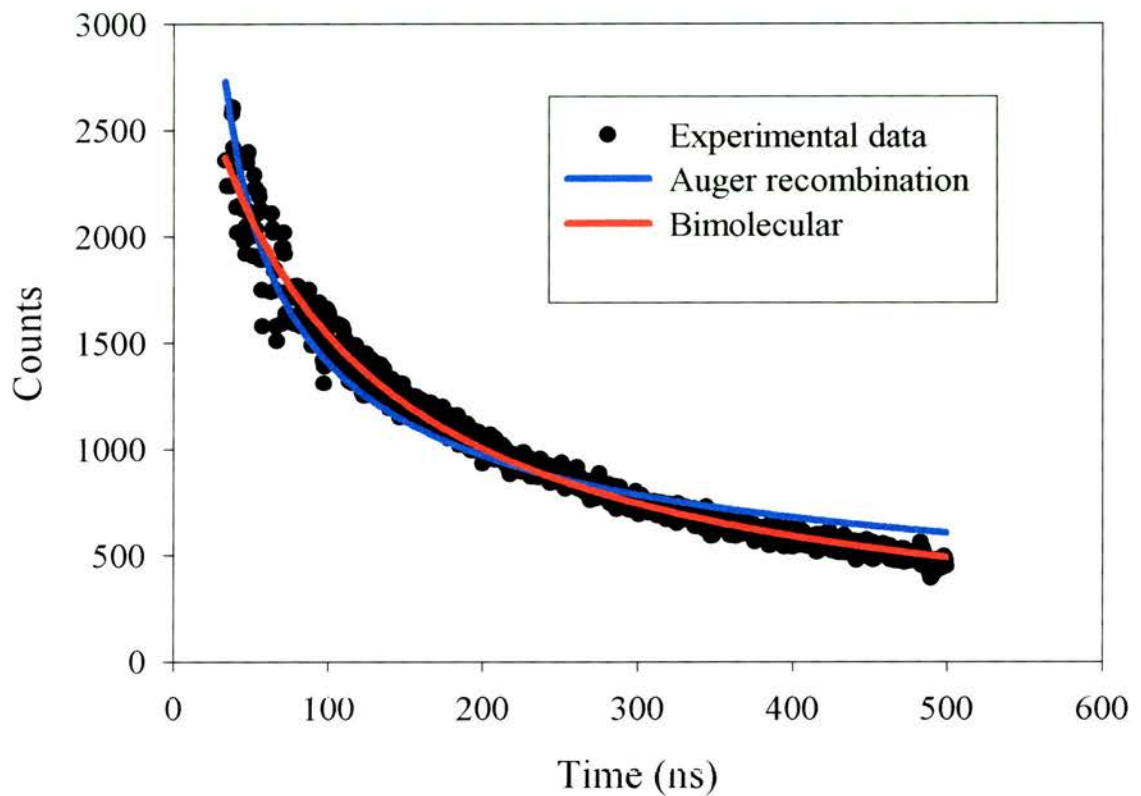


Figure 5-5 TRPL of MR1168 with Auger and Bimolecular fits.

### 5-10 Results for the p-i-n structure samples

Samples MR534, MR535, MR610, MR611 and MR850 are p-i-n structures. Time resolved photoluminescence (TRPL) measurements were performed on these five samples at room temperature. The results are shown in Figures 5-6 to 5-10, plotted on a logarithmic scale and fitted with exponential decays. Samples MR534 and MR535 were fitted with a single exponential decay and MR610, MR611 and MR850 with double decays.

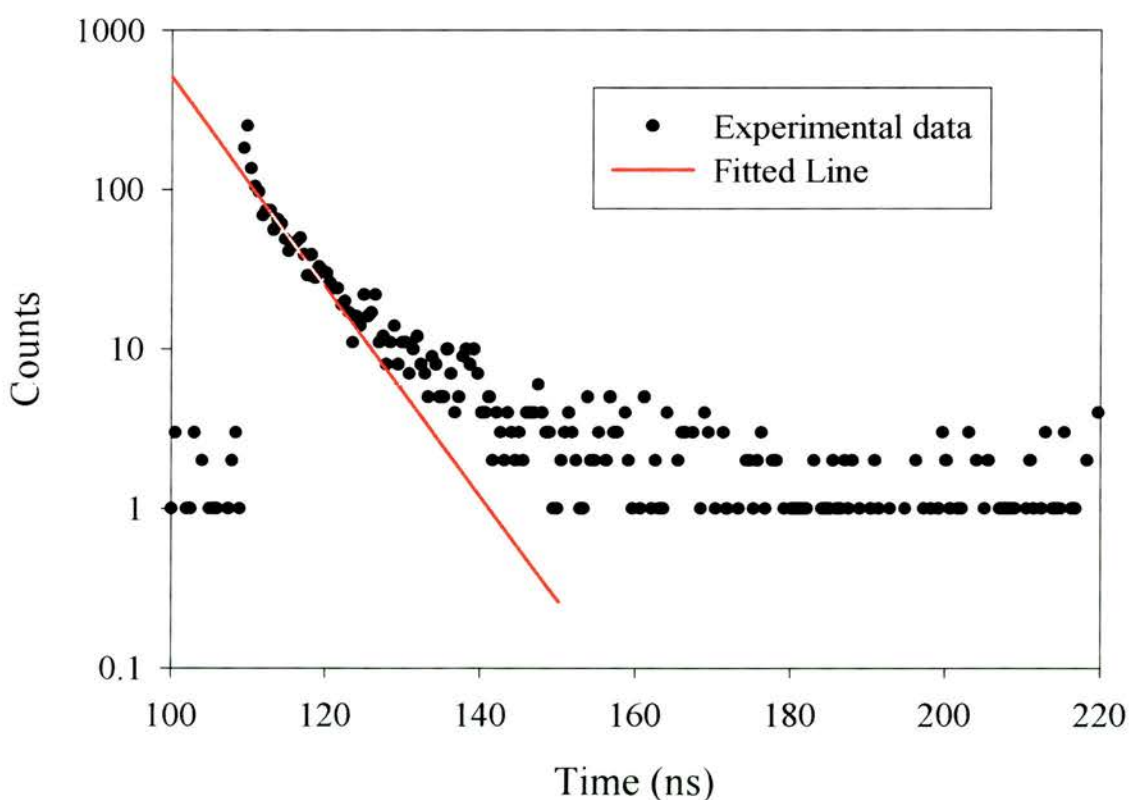


Figure 5-6 Photoluminescence decay for sample MR534. The fitted decay has a time constant of 6.6ns.

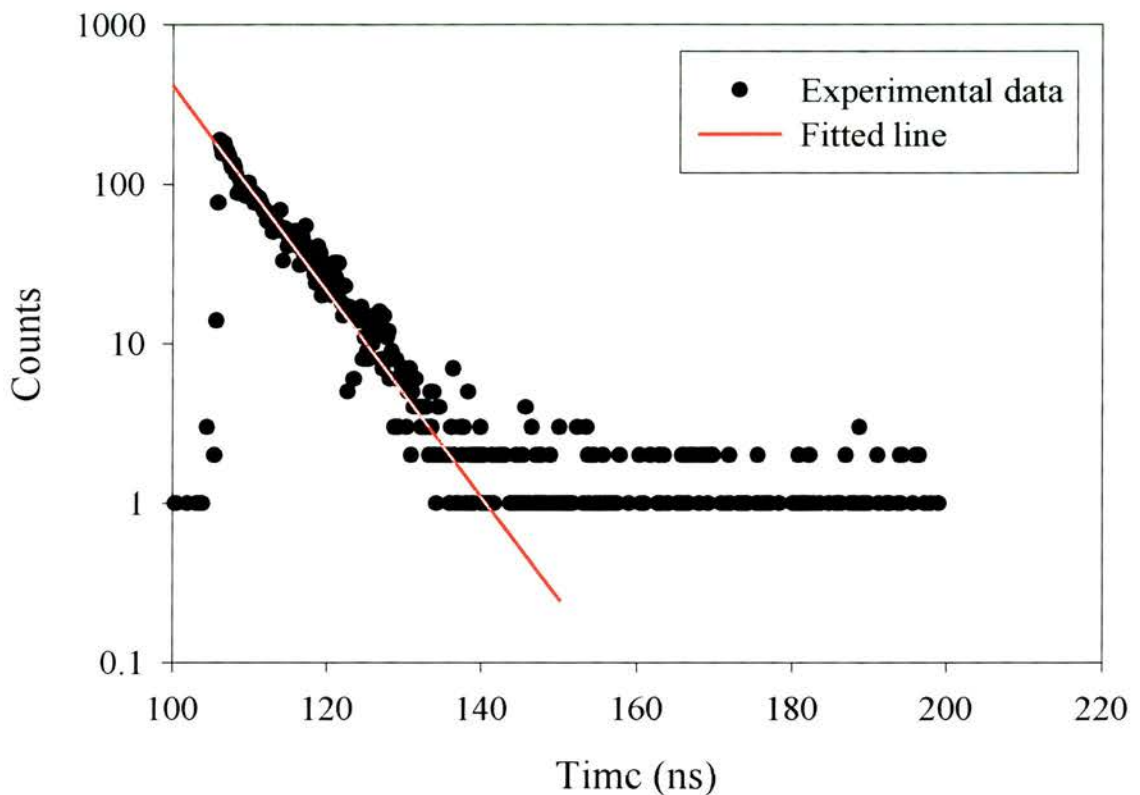


Figure 5-7 Photoluminescence decay for sample MR535. The fitted decay has a time constant of 6.7ns.

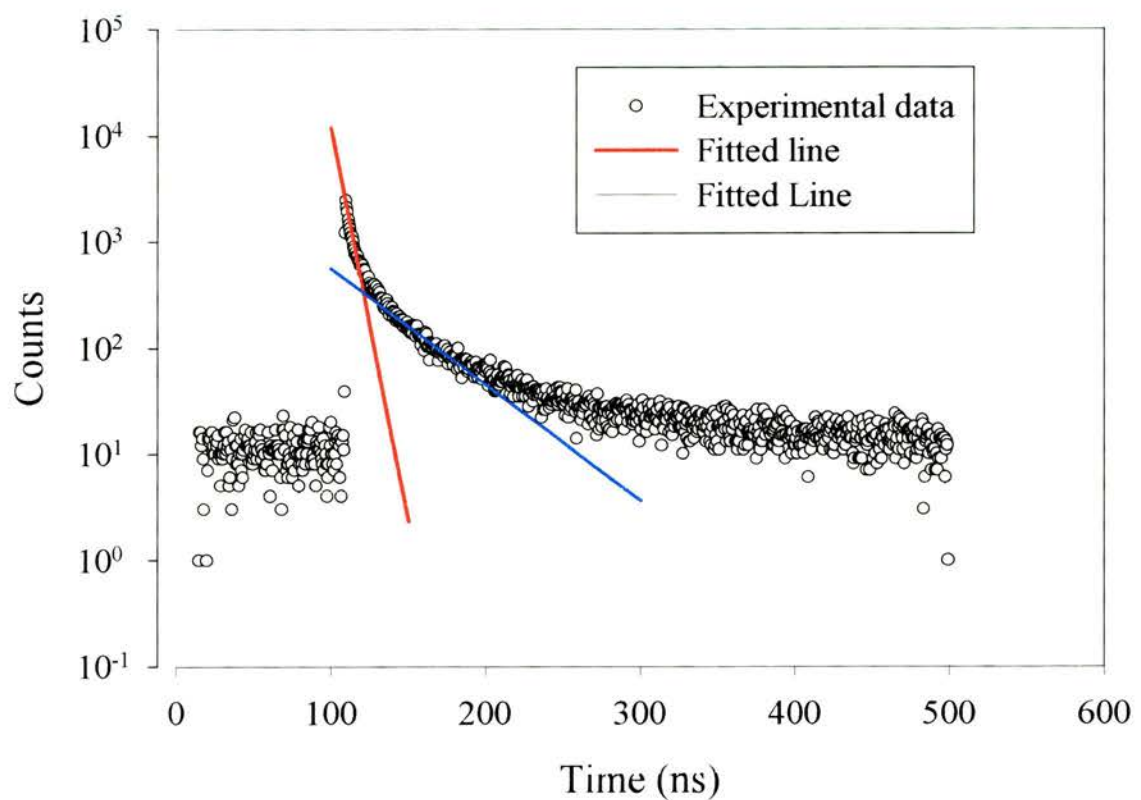


Figure 5-8 Photoluminescence decay for sample MR610. The fitted decay has two time constants of 5.8ns and 39.7ns.

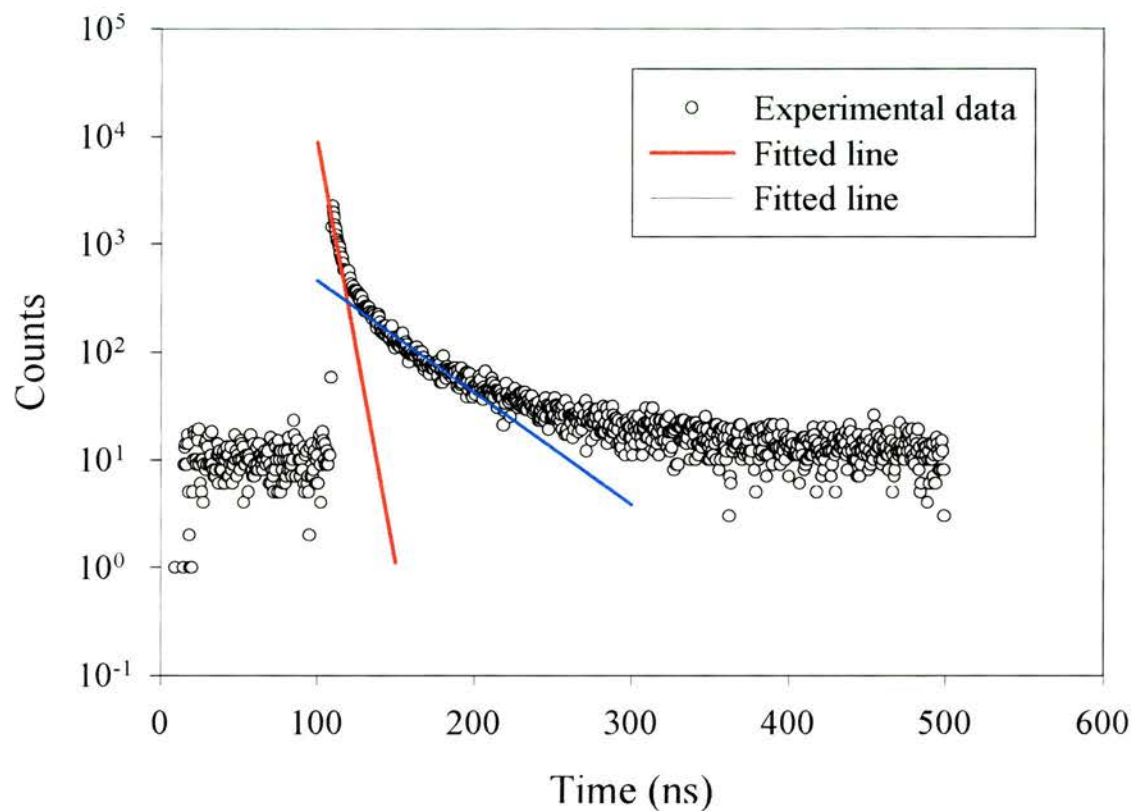


Figure 5-9 Photoluminescence decay for sample MR611. The fitted decay has two time constants of 5.57 ns and 41.8 ns.

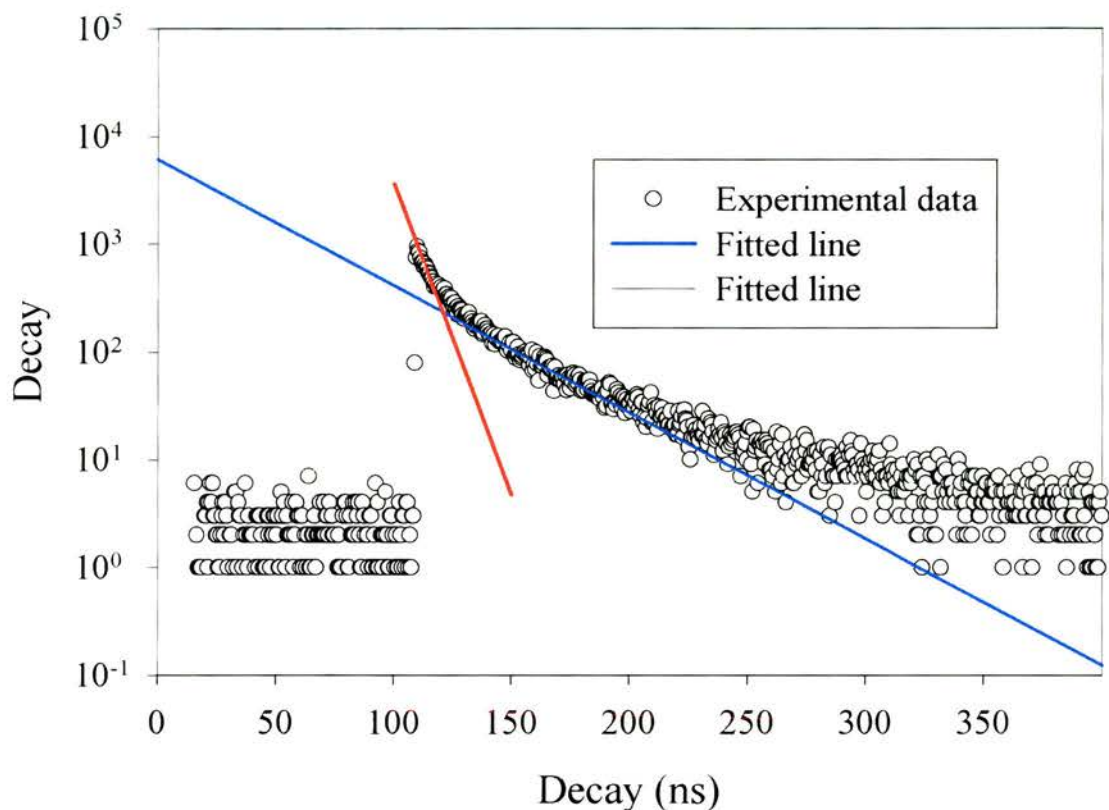


Figure 5-10 Photoluminescence decay for sample MR850. The fitted decay has two time constants of 7.5ns and 37ns.

### ***5-11 Discussion for p-i-n structures***

The carrier lifetimes of the doped samples are summarised in Table 5-1. MR534 and MR535 both exhibit one decay constant of 6.6 and 6.7 ns respectively. Samples MR610, MR611 and MR1168 have decays of two exponential components. MR610 decays with 5.8ns and 39.7ns. MR611 decays with 5.6ns and 41.8ns. MR850 decays with 7.5ns and 37ns. All the samples exhibit the slower component around 6ns.

Carrier sweep-out due to inbuilt fields, tunnelling and recombination through interfaces and defects are the possible contributors. In the undoped sample, MR1168, the recombination was attributed to radiative recombination, as discussed in section 5.9. This sample did not give evidence for recombination through Shockley-Read or tunnelling mechanisms. The only difference between sample MR1168 and the set discussed in this section is the doping. MR1168 is undoped whereas MR534, MR535, MR610, MR611 and MR850 are p-i-n structures. This leads to a field across the wells, which will sweep out any carriers that have escaped from the wells. Therefore the decays of the p-i-n structures, being considerably shorter than that of MR1168 (220ns), are attributed to these sweep-out effects.

The shorter component of the TRPL decays for the p-i-n structure samples are plotted against well width in Figure 5-11. There is a small trend towards increasing lifetime with increasing well width. The times are similar to those obtained by Burr et al where a room temperatures sweep out time of 3.9ns was measured in InGaAsP MQWs<sup>6</sup>. The electron thermionic emission time has been calculated to be on the order of 10s of picoseconds, section 5-6. However the hole escape time is much longer, on the order of nanoseconds. The resulting charge separation will result in an electric field opposing the in-built field caused by the p-i-n structure. This field screening will have the effect of increasing the electron sweep out time and producing non-exponential behaviour.

Therefore the short lifetime components are attributed to the electron thermionic emission and subsequent sweep-out. Applying an external field across the samples would confirm whether this is the mechanism involved for these lifetimes. This would involve the fabrication of devices which was not possible in the timeframe of this work.

Samples MR610, MR611 and MR850 have a longer lifetime component of 40, 42 and 37ns respectively. The well width dependence of this component is shown in Figure 5-12. The lifetimes are similar, and no conclusive well width dependence can be drawn.

The calculated hole thermionic emission times give a value of 66ns for a 9.0nm well and 25ns for a 5.5nm well. The theoretical predictions of hole thermionic emission times agree well with the experimentally observed decay times.

Therefore, the shorter components of the TRPL decays of the p-i-n structures are proposed to be electron sweep-out and the longer components due to hole sweep-out.

Sample	Well width (nm)	1 <sup>st</sup> electron confinement energy (meV)	Carrier lifetime (ns)	
MR534	6.5	62	6.6	
MR535	9.0	43	6.7	
MR610	6.5	67	5.8	40
MR611	5.5	78	5.6	42
MR850	9	40	7.5	37

*Table 5-1 Summary of the carrier lifetimes.*

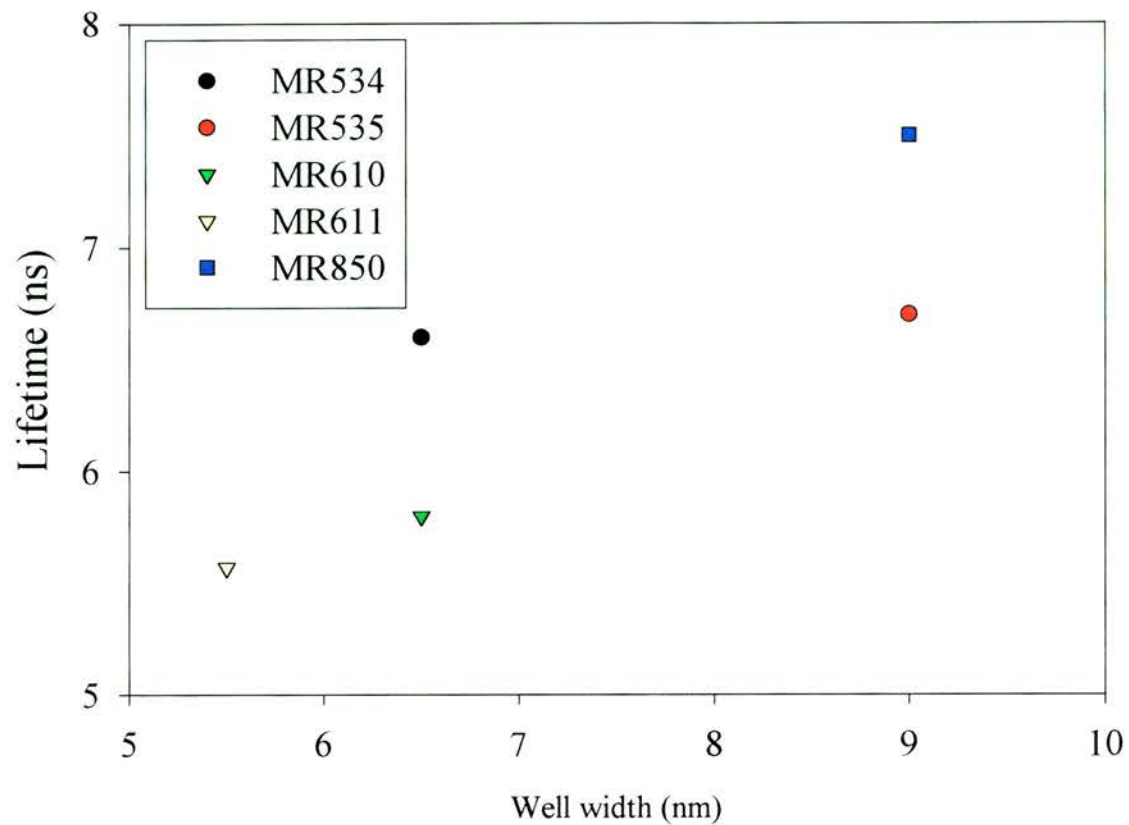


Figure 5-11 Short carrier lifetime component as a function of well width.

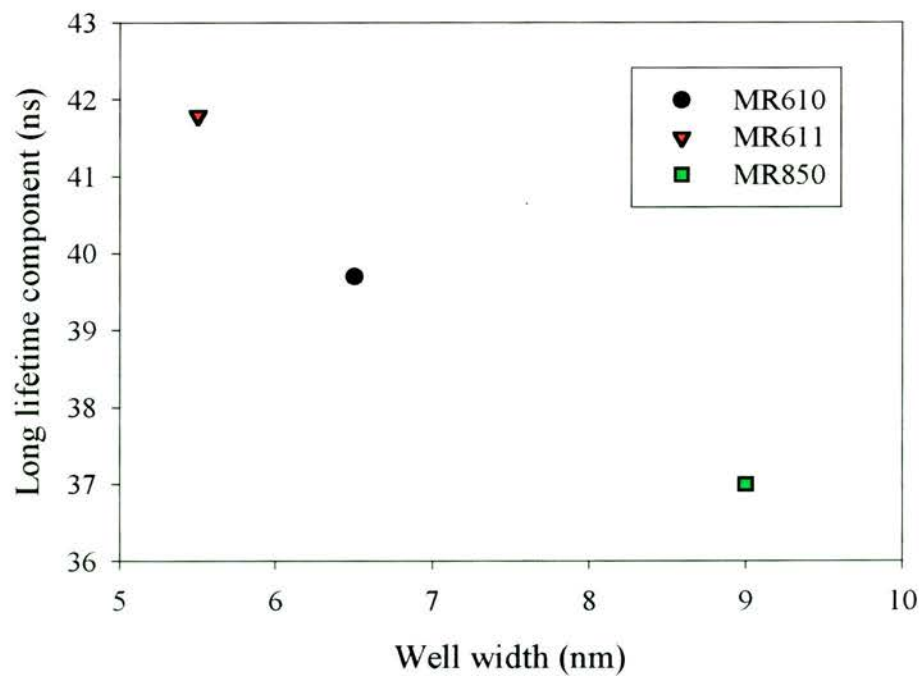


Figure 5-12 Long carrier lifetime component as a function of well width.

### **5-11-1 Conclusion**

In conclusion, knowledge of the carrier lifetime for each sample is important for the following results in this thesis. For four of the samples the lifetime is considerably longer than the repetition time of the OPO system. The other two have lifetimes that, although shorter, will still mean the existence of carriers 12ns after excitation. For example, a lifetime of 7ns will lead to 18% of the carriers remaining after 12ns. Therefore in all cases there is a build up of carriers. In a pump-probe configuration the probe does not examine an empty state when it arrives slightly before the pump pulse as there are still carrier left over from the previous pump pulse, which occurred 12ns previously.

**5-12 Bibliography**

- 1 W. Shockley and J. W.T. Read, "Statistics of the recombination of holes and electrons," *Phys. Rev.*, **87** (5), pp. 835-842, 1952.
- 2 E. Wintner and E. P. Ippen, "Nonlinear carrier dynamics in  $\text{Ga}_x\text{In}_{1-x}\text{As}_y\text{P}_{1-y}$  compounds," *Appl. Phys. Lett.*, **44** (10), pp. 999-1001, 1984.
- 3 G. P. Agrawal and N. K. Dutta, *Semiconductor lasers*, 2nd ed. (International Thomson Publishing, London, 1993).
- 4 T. B. Norris, X. J. Song, W. J. Schaff, L. F. Eastman, G. Wicks, and G. A. Mourou, "Tunneling Escape Time of Electrons from a Quantum Well under the Influence of an Electric Field," *Appl. Phys. Lett.*, **54** (1), pp. 60-62, 1989.
- 5 J. A. Cavailles, D. A. B. Miller, J. E. Cunningham, P. LiKamWa, and A. Miller, "Simultaneous measurements of electron and hole sweep-out from quantum wells and modelling of photoinduced field screening dynamics," *IEEE J. Quant. Electron.*, **28** (10), pp. 2486-2497, 1992.
- 6 E. Burr, J. Song, and A. J. Seeds, in *60ps Recovery Time in an InGaAsP Quaternary Multiple Quantum Well Saturable Absorber Employing Carrier Sweep-Out*, Nice, 2000.

# Chapter 6

## Spin relaxation

### ***6-1 Summary***

In this chapter key spin relaxation mechanisms are introduced. The spin relaxation times are measured at room temperature for a range of InGaAs(P) samples of varying well width. These are then compared with the results obtained for GaAs and the dominant spin mechanism discussed.

### ***6-2 Introduction***

In bulk InGaAsP the light and heavy hole transitions are degenerate at  $k=0$  as discussed in chapter 2. However, in quantum wells this degeneracy is lifted and it becomes possible to create 100% spin polarised electrons with circularly polarised light. After excitation, these electrons will then relax by various mechanisms to produce equal numbers in both the spin up and spin down states. This excitation was initially demonstrated in a series of experiments between 1967 and 1971<sup>1-4</sup>.

One way in which we can examine this spin relaxation is to utilise the spin dependent nature of phase space filling, a mechanism of exciton saturation that arises from the Pauli exclusion principle. As the carrier density increases, the low lying  $k$  states start to fill up. Excitons are created from these states so their phase space filling precludes the possibility of creating more excitons. Analysis of the temporal dependence of the PSF allows us to determine the spin relaxation.

### 6-3 Spin relaxation mechanisms

There are two general types of spin relaxation in metals and semiconductors<sup>5</sup>. The first mechanism arises from the mixing of states with opposite spin. This is due to spin-orbit interaction,  $\mathbf{k} \cdot \mathbf{p}$  interaction and the break-up of spin degeneracy owing to a lack of inversion symmetry. The second involves magnetic interactions that connect states of opposite sign and may directly result in spin-flip.

The two mechanisms described here that depend on band structure effects are D'Yakonov and Perel (DP) and Elliot and Yafet (EY). The Bir, Aronov and Pikus (BAP) mechanism depends upon magnetic interactions.

#### 6-3-1 D'yakonov and Perel mechanism

In an asymmetric structure Kramer's degeneracy,  $E(k_{\parallel}, \uparrow) = E(-k_{\parallel}, \downarrow)$ , is always conserved, however, the spin degeneracy,  $E(k_{\parallel}, \uparrow) = E(k_{\parallel}, \downarrow)$ , is broken as a consequence of spatial inversion<sup>6</sup>. The DP mechanism is based on this effect.

The breakdown of the spin degeneracy results in a spin-splitting of the conduction band which is equivalent to the existence of a pseudo-magnetic field that causes a precession of the electron spins. The energy of the electron will then depend on the component of its spin in the direction of the vector,  $\boldsymbol{\kappa}$ .  $\boldsymbol{\kappa}$  is related to the momentum,  $\mathbf{p}$ , by:

$$\begin{aligned}\kappa_x &= p_x (p_y^2 - p_z^2), \\ \kappa_y &= p_y (p_z^2 - p_x^2), \\ \kappa_z &= p_z (p_x^2 - p_y^2)\end{aligned}\tag{6.1}$$

This energy splitting can be written as<sup>7</sup>:

$$\bar{h}\Omega = 2\alpha\kappa \left(2m_c^*\right)^{-3/2} E_g^{-1/2}\tag{6.2}$$

where  $\Omega$  is the frequency of precession of the spin in the magnetic field directed along  $\kappa$ .  $\alpha$  is a numerical coefficient having the dimensions of the spin-orbit splitting and  $m_c^*$  is the effective mass of the electron in the conduction band.

Scattering of the electron changes its momentum, which leads to a rotation of its precession axis. If the product of the precession frequency and the momentum relaxation time,  $\tau_p$ , is much less than unity then there will be many rotations before the spin relaxes. In this case the average value of the square of the angle of spin rotation,  $\overline{\varphi^2}$ , during a time interval,  $t \gg \tau_p$ , can be written in the form:

$$\overline{\varphi^2} = (\Omega \tau_p)^2 \frac{t}{\tau_p} \quad (6.3)$$

The ratio  $t/\tau_p$  gives the number of flips of the precession axis during the time  $t$ , and  $\Omega \tau_p$  the angle of spin rotation during the time interval between the flips. For the spin relaxation time ( $t = \tau_s$ ) the average square spin,  $\overline{\varphi^2}$ , will be one. This gives:

$$\frac{1}{\tau_s} = \alpha \overline{\Omega^2} \tau_p \quad (6.4)$$

where:

$$\overline{\Omega^2} = \frac{16}{35} \alpha^2 \frac{\varepsilon^2}{\hbar^2 E_g} \quad (6.5)$$

with  $\alpha$  dimensionless coefficient.

In three and two dimensions, we can apply the Hamiltonian of the electron in the conduction band:

$$H = \frac{p^2}{2m} + \frac{\hbar}{2}(\sigma \Omega) \quad (6.6)$$

with  $\sigma$  the Pauli matrix. For the three dimensional case this gives<sup>8</sup>:

$$\frac{1}{\tau_s} = \frac{2}{3} \Omega^2 \tau_c \quad (6.7)$$

where  $\tau_c$  is the effective collision time taking into account the angle of the interaction responsible for the relaxation process. From this equation we can see that as the collision rate increases ( $\tau_c$  decreases) this mechanism becomes less effective. This is because the spins do not have time to precess significantly before the next randomising collision. For a non-degenerate carrier distribution in a two dimensional case of structure <001>, D'yakonov and Kachorovskii (DK)<sup>9</sup>, and Bastard and Ferreira<sup>10</sup> calculated the effect of bulk inversion asymmetry in the quantum wells and obtained:

$$\frac{1}{\tau_s} = \frac{2(\alpha E_1 / \hbar)^2}{E_g k_B T} \int_0^\infty \varepsilon \tau_v(\varepsilon) \exp\left[-\frac{\varepsilon}{k_B T}\right] d\varepsilon \quad (6.8)$$

In this case the effective magnetic field lies parallel to the well. Equation (6.8) shows that the spin flip is more efficient for narrower wells as long as  $E_1$ , the first electron energy, increases with decreasing well width,  $L$ . For infinite wells  $E_1$  is proportional to  $1/L^2$  so, ignoring the energy dependence of  $\tau_v$ , we can approximate equation (6.8) to:

$$\frac{1}{\tau_s} \propto \frac{1}{E_g L^4} \quad (6.9)$$

On comparison of the spin relaxation rates for bulk and quantum well semiconductors DK found the enhancement is given by<sup>9</sup>:

$$\frac{1}{\tau_{s_{2D}}} = \frac{4}{(k_f L)^4} \frac{1}{\tau_{s_{3D}}} \quad (6.10)$$

It has been found that the DK theorem differs by a factor of ten from experimental measurement.

This is because they assume that  $k_{\parallel} \ll \frac{\pi}{L}$ , where  $L$  is the thickness of the wells and  $k_{\parallel}$

the in-plane momentum of the quantum well state that is  $k_B T$  above the band edge.

This is not satisfied for common well widths at room temperature.

Lau et al<sup>11</sup> considered both the inversion symmetry and the spin-orbit coupling in order to calculate the spin-splitting. They found that:

$$\frac{1}{\tau_s} = \frac{1}{n} \int D(E) f(E) [1 - f(E)] \sum_l \tau_l(E) \Omega_l^2(E) dE \quad (6.11)$$

where  $l$  is the angular index of the field component,  $f(E)$  the Fermi distribution,  $D(E)$  the density of states,  $n$  the electron density,  $\Omega$  the effective magnetic field and  $\tau_l^{-1}$  the scattering rate defined by:

$$\tau_l^{-1} = \int_0^{2\pi} \sigma(\theta, E) (1 - \cos(\theta)) d\theta \quad (6.12)$$

where  $\sigma(\theta, E)$  is the scattering cross section found from the mobility. A fourteen band nanostructure model is used calculate  $\Omega^2(E)$ . They find that this model agrees well with experimental results for GaAs multiple quantum wells.

The DP mechanism is thought to be dominant for low acceptor impurity concentration and/or high temperatures. Heavy doping or high carrier-carrier scattering would make this process less effective (see Equation (6.7)). In quantum wells, the effect is enhanced due to the increased spin-orbit splitting of the conduction band. This gives greater local electric fields hence accelerating the precessions that cause the spins to flip.

### 6-3-2 Elliot and Yafet mechanism

Elliot<sup>12</sup> and Yafet<sup>13</sup> considered the effect of spin orbit coupling on normal electron-phonon and electron-impurity scattering. The mechanism they proposed is a

consequence of mixing of the valence band wavefunctions into conduction band wavefunctions away from  $k=0$ . This mixing allows electrons to spin flip due to momentum scattering from optical and acoustic phonons and/or impurities. Fishman and Lampel<sup>14</sup> measured the spin-relaxation time of photo-created conduction electrons in p-type GaAs as a function of temperature by using optical pumping methods. They showed that:

$$\frac{1}{T_1(\varepsilon)} \sim \left( \frac{\eta}{1+\eta} \right)^2 \left( \frac{\varepsilon}{E_G} \right)^2 \frac{1}{\tau_p(\varepsilon)} \quad (6.13)$$

where  $1/T_1(\varepsilon)$  is the relaxation rate at a given kinetic energy,  $\varepsilon$ , and  $\eta$  is the ratio of the spin-orbit coupling to the energy gap,  $E_G$ . The momentum relaxation time is denoted by  $\tau_p(\varepsilon)$ . The spin relaxation rate increases with an increasing momentum relaxation rate, contrary to the DP mechanism.

It has been suggested that the EY mechanism will contribute to the electron spin relaxation at high temperatures and/or high hole concentrations.

### 6-3-3 Bir, Aronov and Pikus mechanism

The BAP mechanism is based on the magnetic interaction between an electron and hole where the spins are flipped on the event of a collision. The probability of this is determined by the exchange interaction of the electrons and holes described by the Hamiltonian:

$$H_{exch} = A_{exch} V \mathbf{J} \cdot \mathbf{S} \delta(\mathbf{r}) \quad (6.14)$$

where  $V$  is the crystal volume,  $\mathbf{J}$  is the hole angular momentum operator,  $\mathbf{S}$  is the electron spin and  $\mathbf{r}$  is the relative distance between the electron and hole.

The spin relaxation time is then given as<sup>14</sup>:

$$\frac{1}{T_1(\varepsilon)} = N_l \sigma_l v \quad (6.15)$$

where  $N_l$  is the concentration of holes contributing to the electron-spin relaxation,  $\sigma_l$  can be interpreted as a spin-flip cross section and  $v$  is the electronic velocity,  $(2\varepsilon/m^*)^{1/2}$ .

The enhancement of the BAP mechanism in quantum wells as compared to bulk is given by<sup>15</sup>:

$$\frac{1}{\tau_{s_{2D}}} = \frac{3\pi}{2k_f L} \frac{1}{\tau_{s_{3D}}} \quad (6.16)$$

From equation (6.15) we can see that the BAP mechanism is important when excited electrons are surrounded by a high concentration of holes so is dominant in heavily p-doped semiconductors and at low temperatures.

In quantum wells there is an increased electron-hole interaction enhancing the probability of a BAP mechanism.

### **6-3-4 Dominant mechanisms in quantum well semiconductors**

At low temperatures, Damen et al<sup>15</sup> measured a spin relaxation time of 150 ps in a p-doped GaAs quantum well. This was four times shorter than the value obtained for the bulk material. From this comparison, they proposed that the BAP mechanism was dominant at low temperatures due to the increased exchange interaction in quantum wells.

At room temperature the DP mechanism is considered dominant in GaAs quantum wells. Studies by Roussignol<sup>16</sup> and Tackeuchi<sup>17,18</sup> show a well-width dependence of the spin relaxation equivalent to equation (6.9). To eliminate sample dependent effects Perozzi<sup>19</sup> and Cameron<sup>20</sup> studied a number of samples with a single well width.

Cameron concluded that the spin relaxation at room temperature is independent of sample quality and that the predominant scattering results from LO phonons.

Tackeuchi<sup>21</sup> measured the spin relaxation in room temperature InGaAs/InP quantum wells at 1.55 microns and found that it was an order of magnitude faster than in the bulk case. Tackeuchi argued that the EY and not DP mechanism was dominant in this case<sup>22</sup>.

Hyland<sup>23</sup> measured the spin relaxation for InGaAs(P) multiple quantum wells with a 650fs KCL:Tl<sup>0</sup>(1) colour-centre laser. The results presented argued that the spin relaxation rate agreed with the predictions of the DP mechanism. This was reasoned by taking into account the band-gap dependence as well as the well width. Results were fitted to the DK prediction of the relaxation rate being directly proportional to the square of the electron energy.

This chapter extends the work of Hyland by using a different laser source for increased noise reduction, a dynamical model taking into account the excitation and investigating two extra samples.

#### ***6-4 Dynamical model of the spin relaxation***

Figure 6-1 shows a schematic diagram of a five level model representing free carrier and exciton states for each spin case and a common ground state. The free carrier and exciton recombination rates are represented by  $\Gamma_1$  and  $\Gamma_2$  respectively and the exciton ionisation by  $\Gamma_3$ . The spin relaxation rates are denoted by  $\Gamma_{s1}$  and  $\Gamma_{s2}$ . The rates of excitation of the spin-up and spin-down states are represented by  $G^+(t)$  and  $G^-(t)$ , which are the opposite circular polarisations as stated in the selection rules, Figure 2-5.

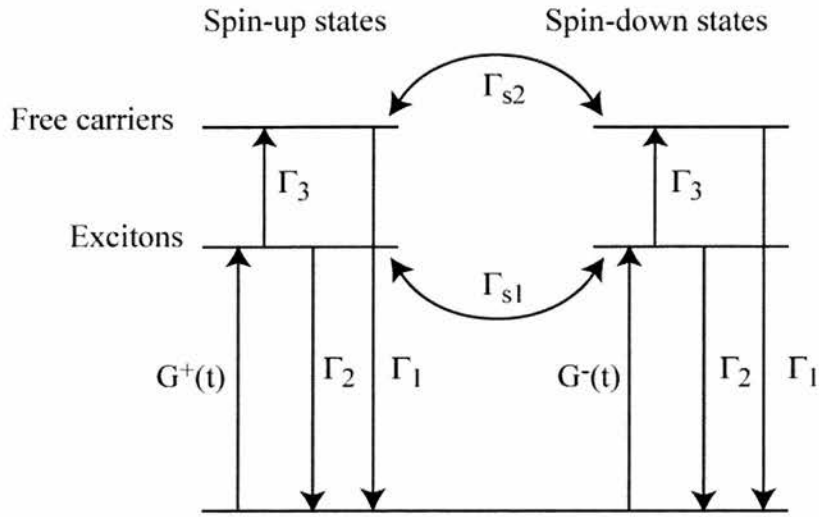


Figure 6-1 Dynamical model of the selection rules.

The exciton and free carrier populations are represented by  $n_{ex}^+$ ,  $n_{ex}^-$ ,  $n_{fc}^+$  and  $n_{fc}^-$  for the spin-up and down states. The evolution of these states can be given by:

$$\begin{aligned}\frac{dn_{ex}^+}{dt} &= -(\Gamma_2 + \Gamma_3 + \Gamma_{s1})n_{ex}^+ + \Gamma_{s1}n_{ex}^- + G^+(t) \\ \frac{dn_{ex}^-}{dt} &= \Gamma_{s1}n_{ex}^+ - (\Gamma_2 + \Gamma_3 + \Gamma_{s1})n_{ex}^- + G^-(t) \\ \frac{dn_{fc}^+}{dt} &= \Gamma_3n_{ex}^+ - (\Gamma_1 + \Gamma_{s2})n_{fc}^+ + \Gamma_{s1}n_{fc}^- \\ \frac{dn_{fc}^-}{dt} &= \Gamma_3n_{ex}^- + \Gamma_{s2}n_{fc}^+ - (\Gamma_1 + \Gamma_{s2})n_{fc}^-\end{aligned}\tag{6.17}$$

A Gaussian profile is assumed for the excitation intensity profile:

$$\begin{aligned}G^+(t) &= g_0^+ \exp\left(-\frac{t^2}{\Delta t_0^2}\right) \\ G^-(t) &= g_0^- \exp\left(-\frac{t^2}{\Delta t_0^2}\right)\end{aligned}\tag{6.18}$$

where  $g_0^\pm$  and  $\Delta t_0$  are the intensity coefficient and duration of the pump pulses.

Equation (6.17) can be transformed from a five to a three level system by stating:

$$\begin{aligned}
 \sigma_{ex} &= n_{ex}^+ + n_{ex}^- \\
 \sigma_{fc} &= n_{fc}^+ + n_{fc}^- \\
 \delta_{ex} &= n_{ex}^+ - n_{ex}^- \\
 \delta_{fc} &= n_{fc}^+ - n_{fc}^-
 \end{aligned} \tag{6.19}$$

Combining (6.19) into (6.17) we have:

$$\begin{aligned}
 \frac{d\sigma_{ex}}{dt} &= -(\Gamma_2 + \Gamma_3)\sigma_{ex} + G^+(t) + G^-(t) \\
 \frac{d\sigma_{fc}}{dt} &= \Gamma_3\sigma_{ex} - \Gamma_1\sigma_{fc}
 \end{aligned} \tag{6.20}$$

and

$$\begin{aligned}
 \frac{d\delta_{ex}}{dt} &= -(\Gamma_2 + \Gamma_3 + 2\Gamma_{s1})\delta_{ex} + G^+(t) - G^-(t) \\
 \frac{d\delta_{fc}}{dt} &= \Gamma_3\sigma_{ex} - (\Gamma_1 + 2\Gamma_{s2})\delta_{fc}
 \end{aligned} \tag{6.21}$$

Taking the populations to be zero at  $t = -\infty$  the solutions to these equations are:

$$\begin{aligned}
 \sigma_{ex}(t) &= (g_0^+ + g_0^-)K_{(\Gamma_2 + \Gamma_3)}(t) \\
 \sigma_{fc}(t) &= (g_0^+ + g_0^-)[K_{\Gamma_1}(t) - K_{(\Gamma_2 + \Gamma_3)}(t)]
 \end{aligned} \tag{6.22}$$

and

$$\begin{aligned}
 \delta_{ex} &= (g_0^+ - g_0^-)K_{(\Gamma_1 + \Gamma_3 + 2\Gamma_{s1})}(t) \\
 \delta_{fc} &= (g_0^+ - g_0^-)[K_{(\Gamma_1 + 2\Gamma_{s2})}(t) - K_{(\Gamma_2 + \Gamma_3 + 2\Gamma_{s1})}(t)]
 \end{aligned} \tag{6.23}$$

where

$$K_\Gamma(t) = \frac{\sqrt{\pi}}{2} \Delta t_0 \exp\left(-\Gamma t + \frac{\Gamma^2 \Delta t_0^2}{4}\right) \left[ 1 + \operatorname{erf}\left(\frac{2t - \Gamma \Delta t_0^2}{2\Delta t_0}\right) \right] \tag{6.24}$$

Assuming that the strength of saturation and transmission change is proportional to the instantaneous population density, the transmission of the probe is given by the integration of the saturation effects over the duration of the probe pulse. The screening,

$s_{fc}$ , and phase space filling,  $p_{fc}$ , effects determine the amount of interaction between the populations and the probe pulse.

The transmission of the probe is then proportional to:

$$\Delta T(t) \propto \int_{-\infty}^{+\infty} G^+(\tau - t) [p_{ex} n_{ex}^+(\tau) + (s_{fc} + p_{fc}) n_{fc}^+(\tau) + s_{fc} n_{fc}^-(\tau)] d\tau \quad (6.25)$$

The saturation effect is present for both the spin up and spin down states for the free carriers. The phase space filling effects are only present in the case of the spin side that the circular polarised probe is sampling, in this case spin-up. The screening effects for the exciton have previously been found to be negligible so we only have a phase-space filling term<sup>23</sup>.

As the recombination and spin relaxation rates are much smaller than the ionisation rate, we can consider them negligible in cases where there are additions with the ionisation rate. Applying this, equation (6.25) simplifies to:

$$\begin{aligned} \Delta T(t) \propto & p_{ex} g_0^+ K_{\Gamma_3}^I(t) + s_{fc} (g_0^+ + g_0^-) [K_{\Gamma_1}^I(t) - K_{\Gamma_3}^I(t)] \\ & + p_{fc} \left[ \frac{1}{2} (g_0^+ + g_0^-) K_{\Gamma_1}^I(t) - g_0^+ K_{\Gamma_3}^I(t) + (g_0^+ + g_0^-) K_{2\Gamma_{s2}}^I(t) \right] \end{aligned} \quad (6.26)$$

where

$$K_\Gamma^I(t) = \exp(-\Gamma t) \left[ 1 + \operatorname{erf} \left( \frac{t - \Gamma \Delta t_0^2}{\sqrt{2} \Delta t_0} \right) \right] \quad (6.27)$$

Looking at the spin relaxation only and assuming a pulse width of 1ps the spin decay can be fitted with the function:

$$\Delta T(t) = 2A \exp(-2\Gamma_{s2} t) \left[ 1 + \operatorname{erf} \left( \frac{t - 2\Gamma_{s2}}{\sqrt{2}} \right) \right] \quad (6.28)$$

with  $t = t' - t_0$  where  $t'$  is the measured time and  $t_0$  the time at zero delay.

### **6-5 Spin relaxation experimental details**

Spin relaxation experiments were carried out using the experimental set-up as described in Figure 4-1, Chapter 4. Time resolved experiments were carried out with quarter wave plates that provided circular polarisations.

The two beam configurations used in this experiment were pump and probe of the same circular polarisation (SCP) and the opposite circular polarisation (OCP), Figure 6-2.

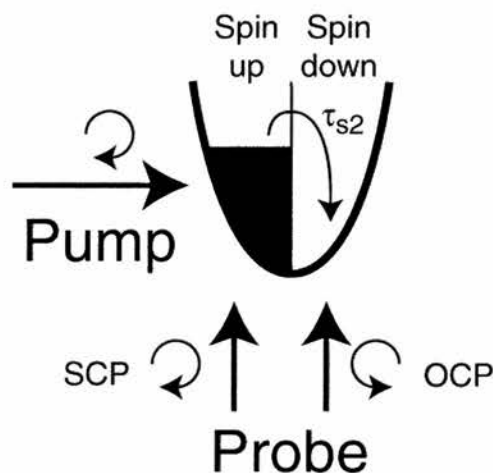


*Figure 6-2 Schematic representation of the SCP and OCP pump and probe configurations.*

In both cases, the circularly polarised pump pulse produces only one spin state due to the lifting of the HH/LH degeneracy encompassed in the selection rules. In the SCP case the probe pulse then examines this excited state and sees an increase in transmission due to phase space filling. As the spins relax the enhanced contribution due to phase space filling decreases. This leads to a decrease in the transmission until the spins have randomised.

In the case of a probe pulse of opposite circular polarisation, there is initially no contribution to the exciton saturation from phase space filling and only the coulomb based effects are evident. As the spins from the excited state relax, phase space filling

becomes evident and the transmission increases until the population of the two spin states equalise over time due to spin relaxation.

Once the populations of the two spin states are equal then the two orthogonal configurations will see the same change in transmission.

### ***6-6 Results***

Same and opposite circular configuration experiments were performed on the six samples, MR534, 535, 610, 611, 850 and 1168 and are shown in Figure 6-3, Figure 6-5, Figure 6-7, Figure 6-9, Figure 6-11 and Figure 6-13.

Examining the data at zero delay for the same and opposite polarisations, we can separate out the effects of phase space filling and Coulomb screening.

The peak at zero delay is due to a mixture of exciton ionisation and coherence. At room temperature, the excitons ionise within 250fs. Coherence effects are also sometimes visible at a delay time approximately equivalent to the propagation thickness of the sample. This is due to reflections of the pump beam within the sample.

The signal before zero delay is non-zero. This is due to the long carrier lifetimes of the samples. The repetition time of 12ns is smaller than the carrier lifetime so there are still carriers in the wells at the time when the next pulse arrives. This leads to an equilibrium state on top of which we measure the spin relaxation.

The difference between the two polarisation cases was taken and fitted as described in the dynamical model section, 6-4. This is shown in Figure 6-4, Figure 6-6, Figure 6-8, Figure 6-10, Figure 6-12 and Figure 6-14. The spin relaxation times are summarised in Table 6-1, along with the well width and first electron confinement energy.

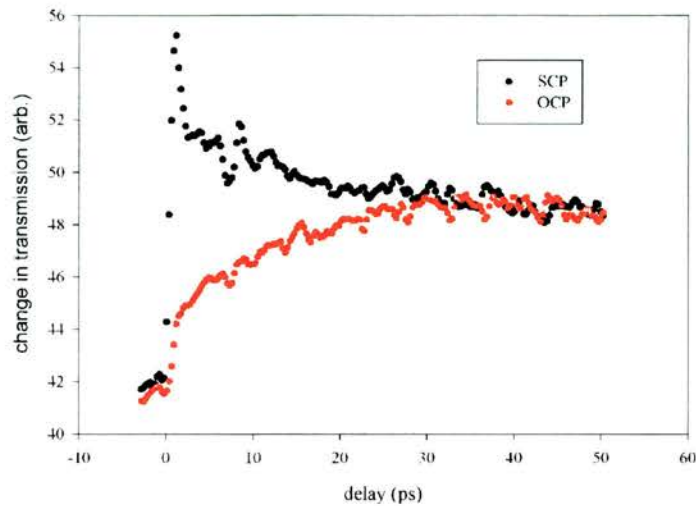


Figure 6-3 Change in transmission of sample MR534 at the heavy hole exciton as a function of probe pulse delay time.

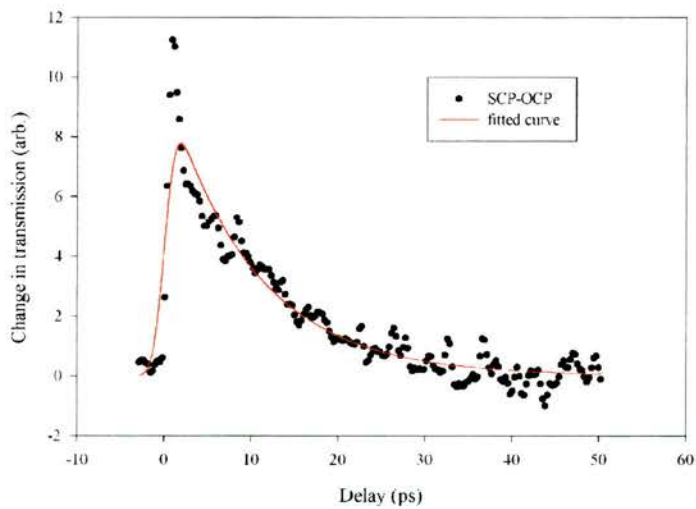


Figure 6-4 Difference between SCP and OCP traces and theoretical fit for the spin relaxation in sample MR534.

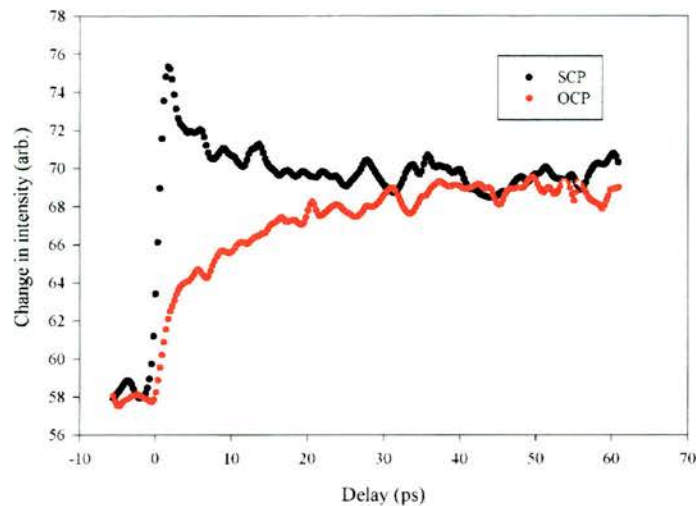


Figure 6-5 Change in transmission of sample MR535 at the heavy hole exciton as a function of probe pulse delay time.

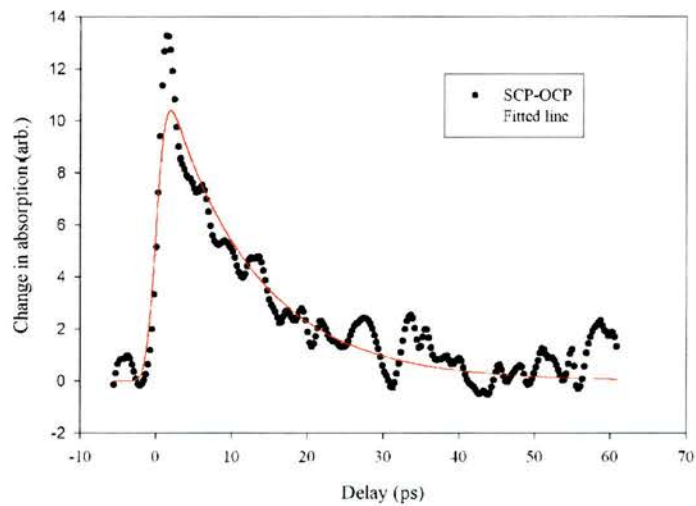


Figure 6-6 Difference between SCP and OCP traces and theoretical fit for the spin relaxation in sample MR535.

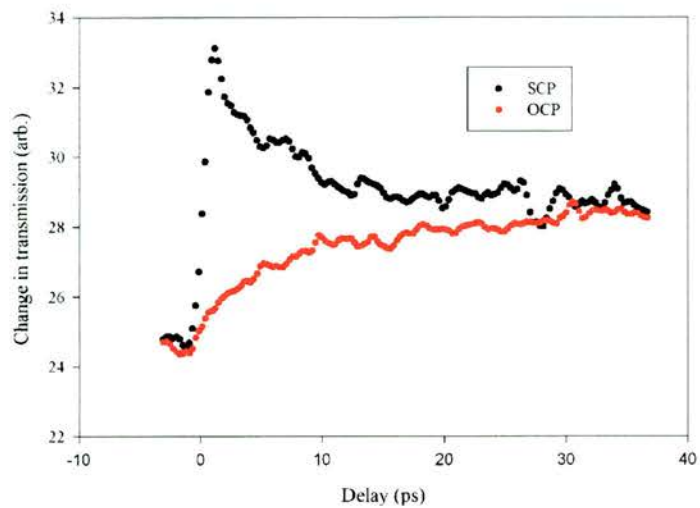


Figure 6-7 Change in transmission of sample MR610 at the heavy hole exciton as a function of probe pulse delay time.

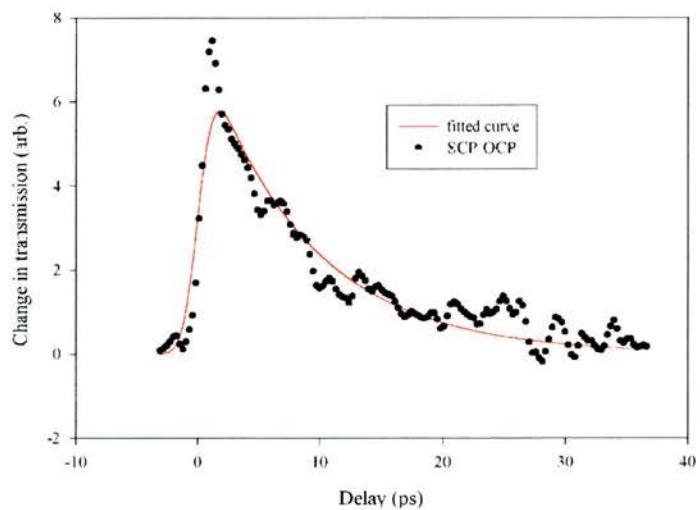


Figure 6-8 Difference between SCP and OCP traces and theoretical fit for the spin relaxation in sample MR610.

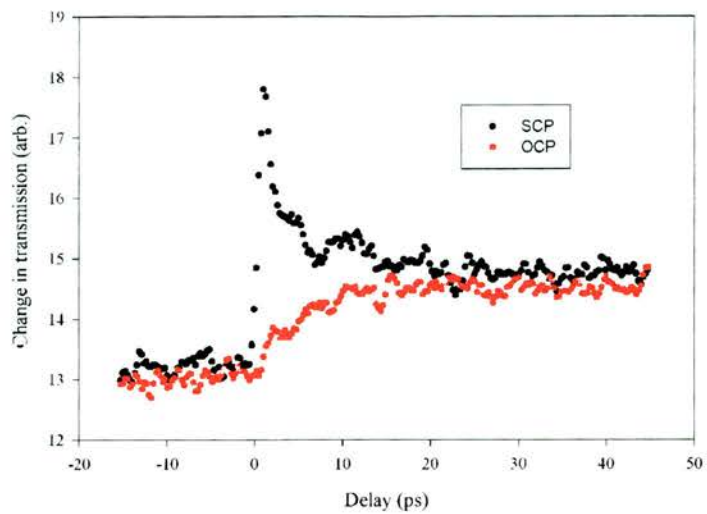


Figure 6-9 Change in transmission of sample MR611 at the heavy hole exciton as a function of probe pulse delay time.

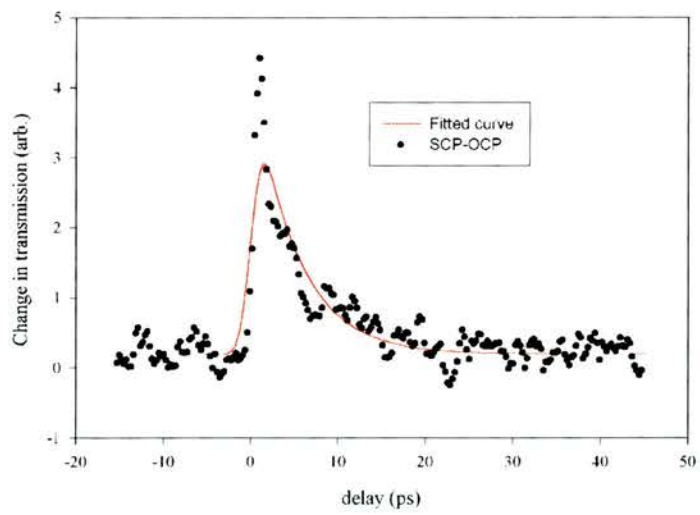


Figure 6-10 Difference between SCP and OCP traces and theoretical fit for the spin relaxation in sample MR611.

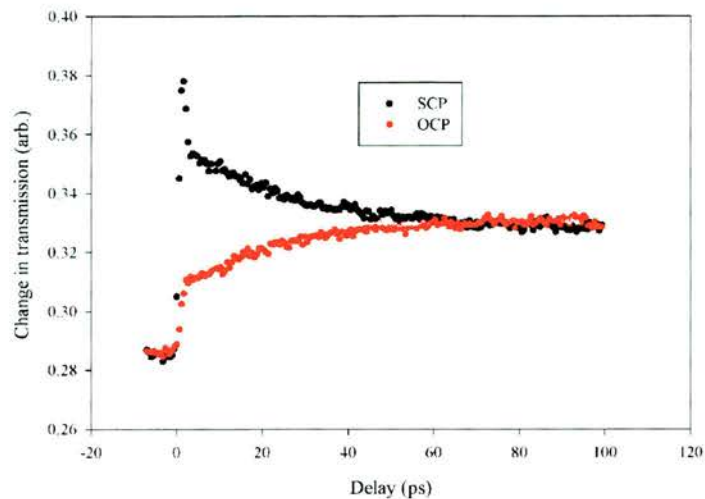


Figure 6-11 Change in transmission of sample MR850 at the heavy hole exciton as a function of probe pulse delay time.

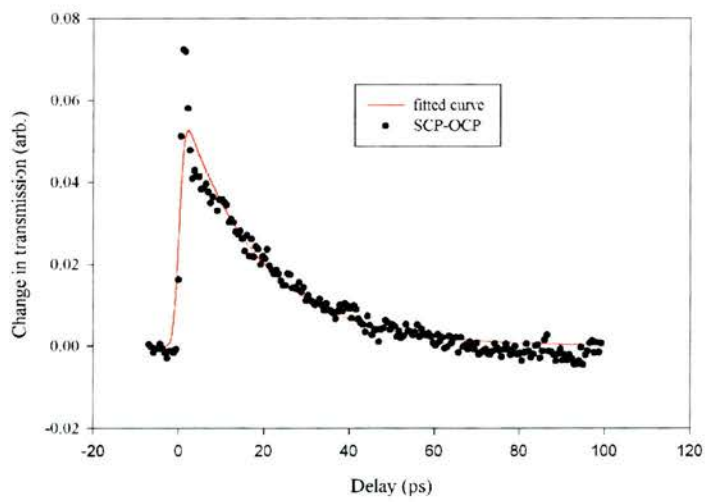


Figure 6-12 Difference between SCP and OCP traces and theoretical fit for the spin relaxation in sample MR850.

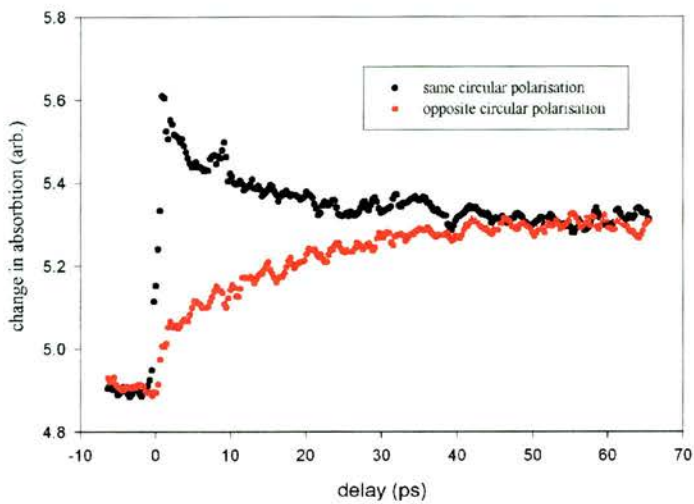


Figure 6-13 Change in transmission of sample MR1168 at the heavy hole exciton as a function of probe pulse delay time.

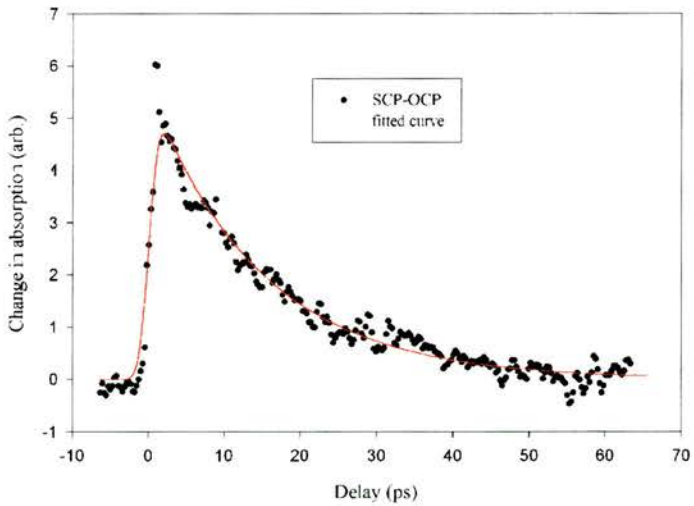


Figure 6-14 Difference between SCP and OCP traces and theoretical fit for the spin relaxation in sample MR1168.

Sample	Well Width (nm)	1 <sup>st</sup> electron confinement energy (meV)	Relaxation time (ps)
534	6.5	62	20
535	9.0	43	23
610	6.5	67	17
611	5.5	78	10
850	9.0	40	36
1168	10.0	38	30

*Table 6-1 Spin relaxation times*

### **6-7 Discussion**

To determine the spin relaxation mechanism we look for the variance in relaxation rate with confinement energy. The first electron confinement energy,  $E_{1e}$ , takes into account many factors including the well width, depth and alloy concentration. Therefore, the spin relaxation rate is plotted against  $E_{1e}$ , Figure 6-15. It is immediately evident that there is an increase in relaxation rate for increasing confinement energy.

GaAs has been extensively studied at room temperature by Tacheuchi, Grevatt and Cameron<sup>18,20,24</sup> and the theoretical prediction of the DP mechanism calculated by Flatte' was found to agree with the experimental results. The band gap of GaAs is larger than that of InGaAsP and InGaAs (1.35eV, 0.783eV and 0.75eV respectively), so to allow direct comparison the spin relaxation rates are plotted against the first electron

confinement energy divided by the band gap for all three material systems. This is shown in Figure 6-16. It can be seen that the InGaAsP points fit along the same line as the GaAs points. From this we draw the conclusion that the dominant spin relaxation mechanism is the same for both systems.

Flatte et al<sup>25</sup> calculated the spin relaxation times for the InGaAs(P) samples according to their theoretical model. It was found that for an electron mobility of  $30,000\text{cm}^2/\text{Vs}$  (see chapter 8) the DP model gives predictions of close to 10ps. If the electron mobility was around  $6700\text{cm}^2/\text{Vs}$  this gives theoretical times of 50ps.

This would suggest that the dominant mechanism does arise from the spin-splitting of the conduction band (the D'yakonov Perel mechanism). However, the actual proportion of the spin relaxation due to this cannot be determined. It is likely that there are also strong effects due to the Elliott-Yafet process as both mechanisms are drawn from bandstructure effects.

We cannot determine by how much the DP mechanism is dominant or the contributions of the other processes.

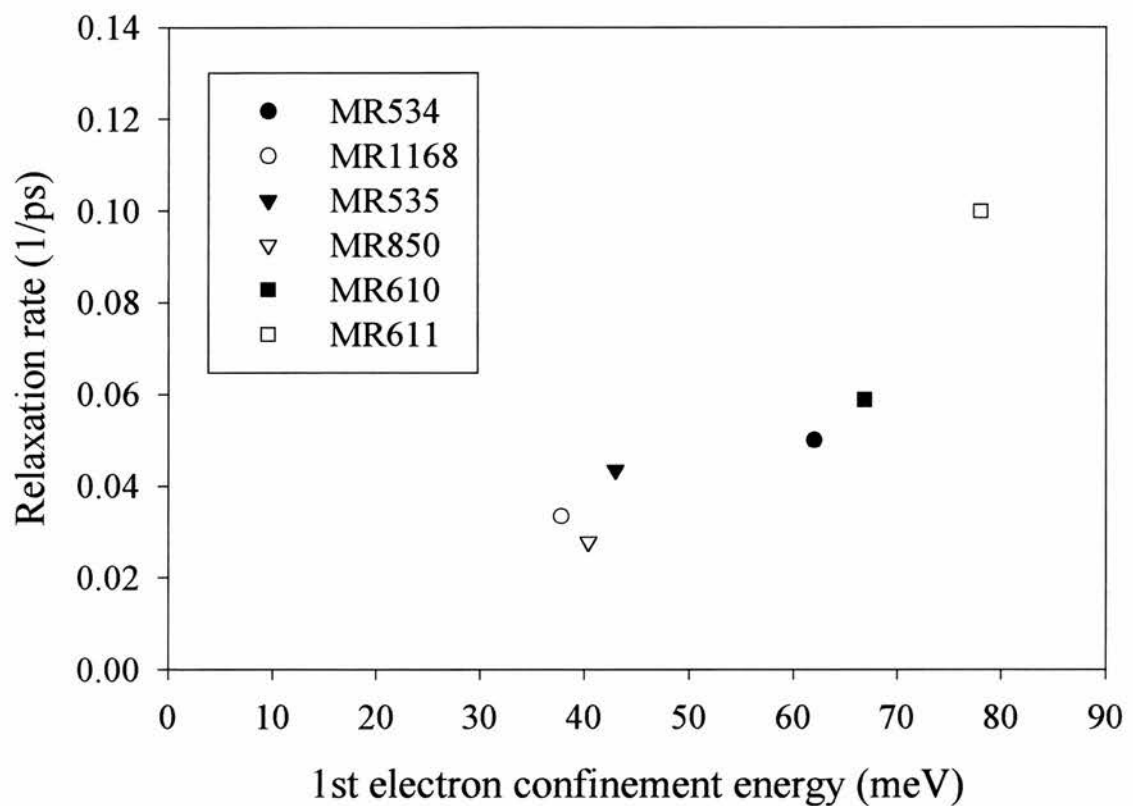


Figure 6-15 Relaxation rate against 1<sup>st</sup> electron confinement energy for the six InGaAsP sample.

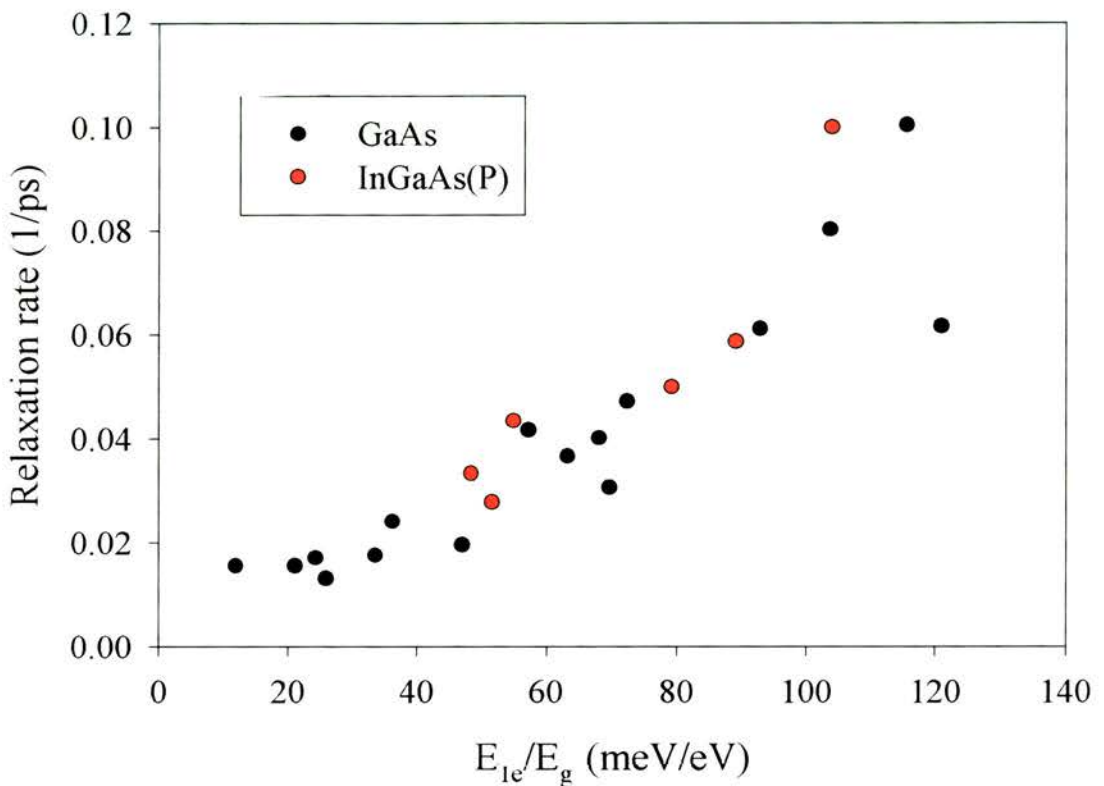


Figure 6-16 Spin relaxation rate as a function of the first electron confinement energy divided by the energy gap for the InGaAs(P) samples along with results obtained by Tackeuchi, Grevatt and Cameron for GaAs MQWs.

### **6-8 Conclusion**

The spin relaxation times for six InGaAs(P) samples have been measured. It is found that the results fit well with those for GaAs when the band-gaps of each sample are taken into account. Flatte et al have made detailed theoretical calculations of the D'yakonov and Perel spin relaxation mechanism and found this to agree with the experimental results assuming an electron mobility of  $30,000\text{cm}^2/\text{Vs}$ .

The InGaAsP samples originated from different wafers and the GaAs samples were from a range of sources. The consistency of results suggests that the interface and impurity scattering is not the main source for the collisions which result in spin-flip. It is concluded that phonon scattering is the most likely source.

The ability to predict the spin relaxation times from sample growth will prove very useful in the development in devices that utilise the electron spin. In particular, all-optical polarisation switches (as shown in the next chapter) could be engineered to produce switches of varying recovery times and optimised for the telecommunications industry. The recent emergence of the field of spintronics, where electron spins are being used to control, store and manipulate information<sup>23,26-29</sup>, highlights the importance of this work.

**6-9 Bibliography**

- 1 G. Lampel, "Nuclear dynamic polarization by optical electronic saturation and optical pumping in semiconductors," *Phys. Rev. Lett.*, **20** (10), pp. 491-493, 1968.
- 2 R. R. Parsons, "Band-to-band optical pumping in solids and polarized photoluminescence," *Phys. Rev. Lett.*, **23** (20), pp. 1152-1154, 1969.
- 3 D. Z. Garbuzov, A. I. Ekimov, and V. I. Safarov, "Measurement of the lifetime and of the spin-relaxation time of electrons in semiconductors by the optical-orientation method," *JETP Lett.*, **13**, pp. 24-26, 1971.
- 4 B. I. Zakharchenya, V. G. Fleisher, R. I. Dzhioev, Y. P. Veshchunov, and I. B. Rusanov, "Effect of optical orientation of electron spins in a GaAs crystal," *JETP Lett.*, **13**, pp. 137-139, 1971.
- 5 E. J. Johnson, R. J. Seymour, and R. R. Alfano, in *Semiconductors probed by ultrafast laser spectroscopy, Vol. II*, edited by R. R. Alfano (Acad. Press, Inc, Orlando, 1984), p. 199-241.
- 6 G. Goldoni and A. Fasolino, "Spin splitting in asymmetric double quantum-wells - a mechanism for spin-dependent hole delocalization (Vol 69, Pg 2567, 1992)," *Phys. Rev. Lett.*, **70** (13), pp. 2051-2051, 1993.
- 7 M. I. D'Yakonov and V. I. Perel, "Spin orientation of electrons associated with the interband absorption of light in semiconductors," *Sov. Phys. JETP*, **33** (5), pp. 1053-1059, 1971.
- 8 M. I. D'Yakonov and V. I. Perel, "Spin relaxation of conduction electrons in noncentrosymmetric semiconductors," *Sov. Phys. Solid State*, **13** (12), pp. 3023-3026, 1972.

- 9 M. I. D'yakonov and V. Y. Kachorovskii, "Spin Relaxation of Two-Dimensional Electrons in Noncentrosymmetric Semiconductors," *Sov. Phys. Semicond.*, **20** (1), pp. 110-112, 1986.
- 10 G. Bastard and R. Ferreira, "Spin-flip scattering times in semiconductor quantum-wells," *Surf. Sci.*, **267** (1-3), pp. 335-341, 1992.
- 11 W. H. Lau, J. T. Olesberg, and M. E. Flatte, "Electron spin coherence times in bulk and quantum well zincblende semiconductors," *cond-mat/0004461*, 2000.
- 12 R. J. Elliott, "Theory of the effect of spin-orbit coupling on magnetic resonance in some semiconductors," *Phys. Rev.*, **96** (2), pp. 260-279, 1954.
- 13 Y. Yafet, "g factors and spin-lattice relaxation of conduction electrons," *Solid State Phys.*, **14**, pp. 1-98, 1963.
- 14 G. Fishman and G. Lampel, "Spin relaxation of photoelectrons in p-type gallium arsenide," *Phys. Rev. B*, **16** (2), pp. 820-831, 1977.
- 15 T. C. Damen, L. Vina, J. E. Cunningham, and J. Shah, "Subpicosecond spin relaxation dynamics of excitons and free carriers in GaAs quantum wells," *Phys. Rev. Lett.*, **67** (24), pp. 3432-3435, 1991.
- 16 P. Roussignol, P. Rolland, R. Ferreira, C. Delalande, G. Bastard, A. Vinattieri, L. Carraresi, and M. Colocci, "Time resolved spin-polarisation spectroscopy in GaAs/AlGaAs quantum wells," *Surf. Science*, **267** (360-364), 1992.
- 17 A. Tackeuchi, S. Muto, T. Inata, and T. Fujii, "Direct observation of picosecond spin relaxation of excitons in GaAs/AlGaAs quantum wells using spin-dependent optical nonlinearity," *Appl. Phys. Lett.*, **56** (22), pp. 2213-2215, 1990.

- 18 A. Tackeuchi, Y. Nishikawa, and O. Wada, "Room-temperature electron spin dynamics in GaAs/AlGaAs quantum wells," *Appl. Phys. Lett.*, **68** (6), pp. 797-799, 1996.
- 19 M. T. Perozzo, Thesis, University of Central Florida, 1995.
- 20 R. S. Britton, T. Grevatt, A. Malinowski, R. T. Harley, P. Perozzo, A. R. Cameron, and A. Miller, "Room temperature spin relaxation in GaAs/AlGaAs multiple quantum wells," *Appl. Phys. Lett.*, **73** (15), pp. 2140-2142, 1998.
- 21 A. Tackeuchi, O. Wada, and Y. Nishikawa, "Electron Spin Relaxation in InGaAs/InP Multiple-Quantum Wells," *Appl. Phys. Lett.*, **70** (9), pp. 1131-1133, 1997.
- 22 A. Tackeuchi and O. Wada, "Electron spin relaxation dynamics in InGaAs/InP multiple quantum wells," *Jpn. J. Appl. Phys.*, **37**, pp. 98-99, 1998.
- 23 J. T. Hyland, Thesis, University of St Andrews, 1999.
- 24 A. R. Cameron, Thesis, University of St Andrews, 1996.
- 25 M. Flatte, *Spin relaxation in InGaAs(P)*; E-mail; 7 June 2000.
- 26 R. Takahashi, Y. Kawamura, and H. Iwamura, "Ultrafast 1.55 Micron All-Optical Switching Using Low-Temperature-Grown Multiple Quantum Wells," *Appl. Phys. Lett.*, **68** (2), pp. 153-155, 1996.
- 27 J. T. Hyland, G. T. Kennedy, A. Miller, and C. C. Button, "Picosecond all-optical polarization switching in InGaAsP MQW's at 1.52  $\mu\text{m}$ ," *IEEE Photonics Technol. Lett.*, **10** (10), pp. 1419-1421, 1998.
- 28 D. D. Awschalom and J. M. Kikkawa, "Electron spin and optical coherence in semiconductors," *Physics Today*, **52** (6), pp. 33-38, 1999.

- 29 D. D. Awschalom and N. Samarth, "Electron precession and coherence in magnetic quantum structures: Room-temperature spin memory," *Solid State Commun.*, **107** (11), pp. 663-672, 1998.

## Chapter 7

### All optical spin polarisation switch

#### 7-1 Summary

In this chapter an all-optical polarisation switch is presented. It is shown that the results depend on carrier-enhanced birefringence in the InGaAsP samples.

#### 7-2 Introduction

As the telecommunication industry is rapidly expanding, the demand for switches capable of high bit rates is becoming even more evident. The switching devices must be able to work at room temperature with recoveries of less than 10ps and contrast ratios of at least 13dB. Ideal operation would be at 1.3 or 1.5 microns to enable easy integration into the current communications network. Simplicity of fabrication and compactness are also very desirable features.

Several methods of producing optical switching have been investigated. Microelectronic mechanical based systems have been reported to be the dominant factor in the current optical switch market<sup>1</sup>, with the demonstration of multi-wavelength small-tilt micromirror based 2x2 fiber optic switch array structures using fixed mirrors and fiber interconnections<sup>2</sup>. However, mechanical systems are slow in comparison to switching times that can be achieved utilising optical nonlinearities.

Optical nonlinearities associated with excitons in quantum wells can be used in different ways to achieve optical switching. Carrier confinement produces enhanced absorption features in quantum wells compared to bulk semiconductors such that optical nonlinearities can be significantly enhanced.

Examples of optical switching through non-resonant optical nonlinearities are systems which utilise the optical stark effect or  $\chi^{(2)}$  and  $\chi^{(3)}$  effects in waveguides. The optical stark effect is a shift of the exciton resonance caused by the electric field of a light beam in a semiconductor, which is particularly pronounced in multiple quantum wells (MQWs). This ultrafast nonlinearity has been reported to enable consecutive switching events spaced 1.7 ps apart but is at the expense of very high optical intensities<sup>3,4</sup>. Non-resonant switching in waveguides requires an intensity dependent refractive index,  $n(I)$ , which leads to an intensity dependent propagation wavevector. This means that changing the power of one or both of them can alter interference conditions between two coherent beams. Switches with one input beam are based on the optical Kerr effect, a result of  $\chi^{(3)}$ , and a number of configurations can achieve the desired phase shifts<sup>5</sup>. One high power beam can also be used to create a phase shift in a low power beam by cross-phase modulation and then switching by interference. Also, four-wave mixing utilises wavelength conversion and is designed for wavelength division multiplexing systems but this suffers from two-photon absorption effects.

Resonant optical nonlinearities in semiconductors occur when the photon energy coincides with the energy of an interband, intraband or excitonic transition. One switching device that uses these nonlinearities is the etalon, which consists of a nonlinear material inside a resonator. Gibbs and Miller first reported optical switching in 1979 using a semiconductor based Fabry-Perot etalon<sup>6,7</sup>. The value of the refractive index and/or absorption coefficient, and hence the cavity resonance condition, depends on the light intensity within the cavity. Using this effect, switching speeds of 3ps with a 35nm bandwidth and contrast ratio of 15dB have been demonstrated using low temperature grown GaAs in an asymmetric device<sup>8</sup>. An extension of this is the use of the quantum confined stark effect (QCSE) in self-electro-optic devices (SEED's)<sup>9,10</sup>.

This effect depends on an electric field across the QW's within a p-n structure and the recovery time depends on carrier sweep-out and the RC time constant of the circuit.

This device combines the photoconductive properties with optical modulator operation associated with the excitons. Absorption saturation is normally limited by carrier recombination, but low temperature growth of GaAs based structures has achieved sub-picosecond timescales at the expense of material quality and excitonic properties<sup>11</sup>.

Carrier sweep-out is an alternative method of speeding-up recovery.

Resonant at 1.55 microns, Takahashi et al developed a low temperature grown reflective all optical polarization switch that utilizes an ultrafast nonlinear mirror using Be doped strained MQWs. Based on photoresponse this device achieved a switching window of 1.5ps<sup>12</sup>.

Spin polarisaed optical nonlinearities offer an alternative option for ultrafast all-optical switching at moderate optical powers as discussed in this chapter. An InGaAs multiple quantum well etalon structure was developed by Nishikawa et al<sup>13</sup> to utilize the effects of spin polarization on linearly polarized light. They demonstrated an all-optical spin polarization switch exhibiting a 7ps time constant with a 4ps switching pulse and an on/off ration of 4:1 at room temperature. J. Hyland<sup>14,15</sup> extended these results to InGaAsP multiple quantum wells with room temperature switching times of 5 to 20 ps at 1.52 microns.

An alternative approach based on carrier spin polarisation has been pioneered recently by Awschalom<sup>16,17</sup>. In this case the spin coherence of excitons is exploited in magnetic fields to control ultrashort pulses for enhanced spin memory. Baumberg<sup>18</sup> demonstrated coherent control of ultrashort pulses using excitons in quantum wells held at low temperatures.

### ***7-3 An all-optical polarisation switch at 1.5 microns***

It is possible to use the effects of spin polarisation to create an all-optical polarisation switch which has the potential for use in soliton pulse control.

As described previously in Chapter 6, excitation with circularly polarised light resonant with the heavy hole exciton creates 100% spin polarisation in a quantum well structure due to the interband selection rules and the lifting of the degeneracy of the heavy and light holes. Due to exciton saturation there will then be a difference in absorption for subsequent left and right circularly polarised light. As a causal consequence of this there will also be a difference in the refractive indices for the two circular components.

Therefore, by exciting with circularly polarised light and probing with linearly polarised light resonant with the heavy hole exciton, a polarisation rotation of the probe may be expected because the two circular components of the probe will depend on the different spin states. After transmission through the sample the two circular components of the probe will have different amplitudes and there will be a phase difference between them because of the absorptive and refractive circular dichroism. Consequently the net result will be elliptical polarisation with a rotation of the major axis.

To create an all-optical switch, an analyser is placed in the path of the probe after the sample cross-polarised with the initial beam. Only when there is a net spin polarisation will there be transmission through the analyser. Therefore we can create a polarisation switch that decays with the spin relaxation time. Ideally, we would like to have minimum ellipticity and a rotation of 90 degrees.

The experimental set-up for the all-optical polarisation switch modifies Figure 4-1 by removing a quarter wave plate from the probe beam, Figure 7-1, to create the configuration of a circular polarised pump and a linear polarised probe. A polarising

beamsplitter is inserted in to the probe beam after the sample and rotated so that there is minimum transmission of the initial probe beam.

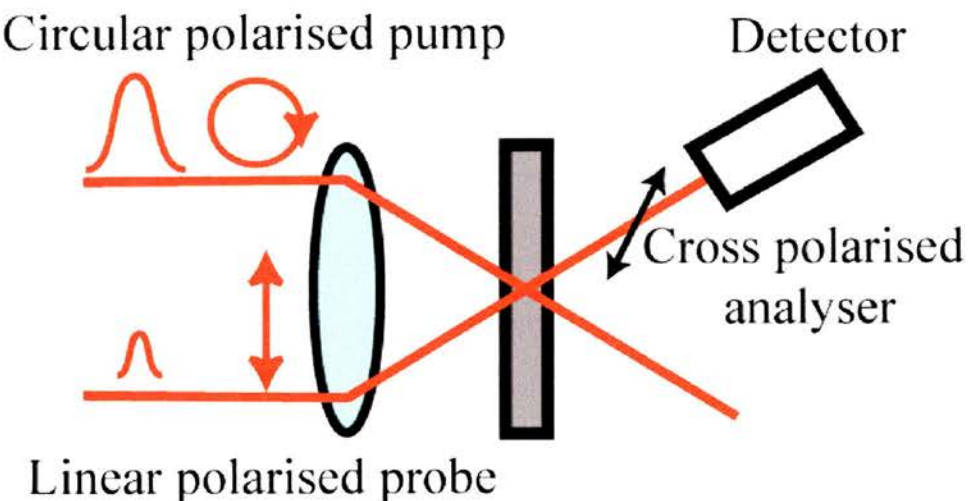


Figure 7-1 Experimental set-up for the polarisation switch.

## 7-4 Results

### 7-4-1 All optical polarisation switch

An all-optical polarisation switch is demonstrated for samples MR850 and MR1168. A complete analysis was performed on the undoped sample MR1168 since interpretation of the results is less complicated.

A typical switch signal for sample MR850 is shown in Figure 7-2, with an increase in signal at zero delay, which then decayed to the original state after the spin relaxation time. This gives an all-optical switch operating on picosecond timescales. However, it was found that the orientation of the circular polarisation of the pump pulse greatly affected the switch signal. This is shown in Figure 7-3 for sample MR850 and Figure 7-4 for MR1168. For one circular polarisation the switch performed as expected, with an increase in signal at zero delay, which then decayed to the original state after the spin relaxation time. The other circular polarisation of the pump pulse gave a decrease in signal, decaying back to the initial value with the spin relaxation time. The two results can be thought of as an effective positive and negative switch.

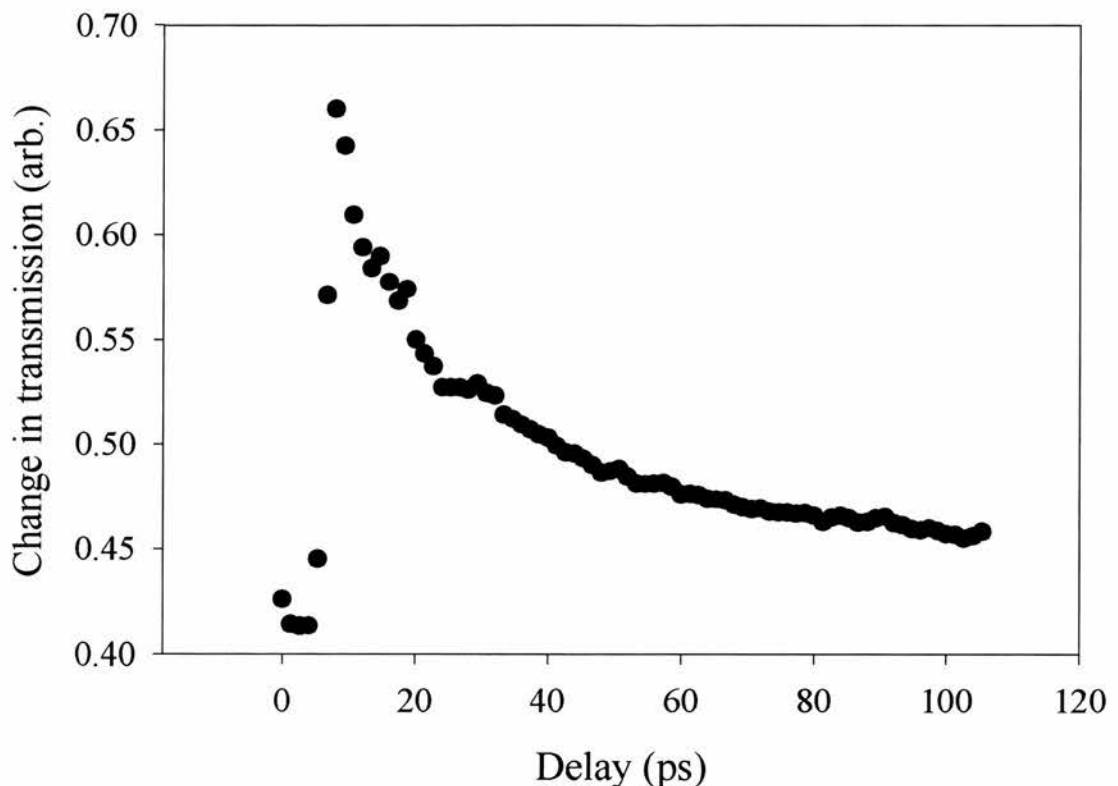


Figure 7-2 Change of transmission for sample MR850 demonstrating an all-optical polarisation switch for sample MR850.

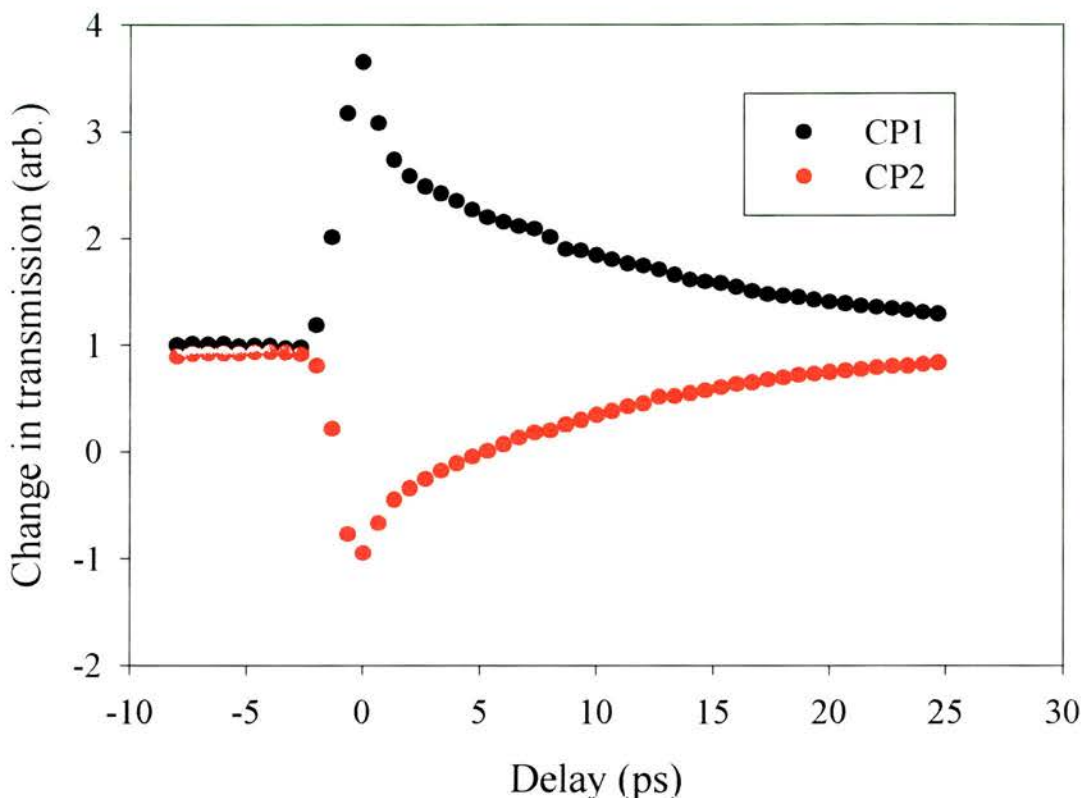


Figure 7-4 Change of transmission as a function of delay for sample MR1168 showing a 30ps switch. CP1 and CP2 are the two orientations of the circular polarisation of the pump pulse. One circular polarisation gives an effective positive switch, and the other an effective negative switch.

### 7-4-2 Experimental analysis of switch

To examine what was occurring in the switch configuration for sample MR1168, the analyser was rotated around the initial crossed polarised position. This gave  $\text{sinc}^2$  signals, Figure 7-5, before and after zero delay for both circular polarisations of the pump pulse. Both pump configurations gave the same result before zero delay but were distinctly different afterwards.

To study the minor axis of the ellipse, the analyser was rotated and at each angular step a delay scan was taken. This gave time delay scans for a range of angles for both circular polarisations. A cross section of this series of results was taken to give the intensity as a function of angle for each delay step. These were then fitted with a  $\text{sinc}^2$  function and the minimum intensity and angle at which this occurred was found for each delay. These values were plotted against delay to give a temporal picture of the absolute value of the minor axis of the ellipse and the orientation angle of the polarisation, Figure 7-6 and Figure 7-7.

The insertion of a half wave plate centred at 1.55 microns into the probe beam, rotationally positioned so as not to alter the angle of polarisation caused the positive switch to become the negative switch and vice versa, i.e. to flip. Rotation of the half wave plate and consequentially the analyser did not cause the switch to flip, nor did rotation of the sample alone.

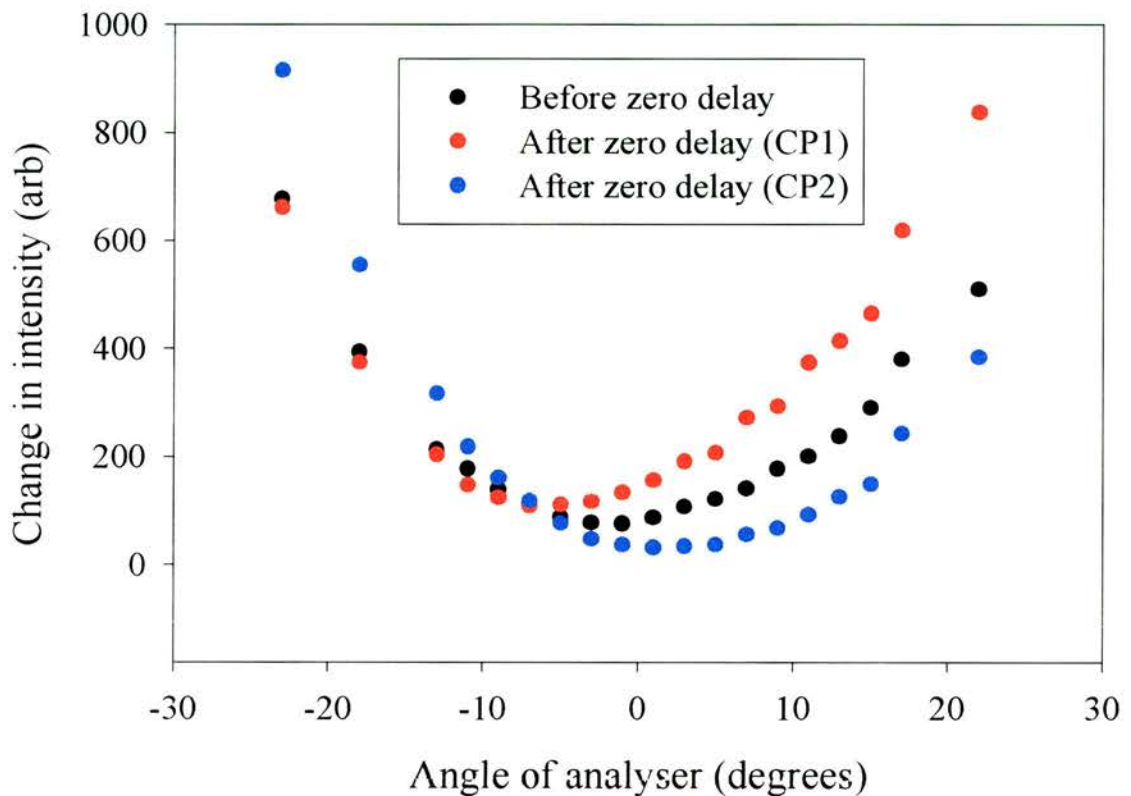


Figure 7-5 Change in transmission as a function of angle for before zero delay and after zero delay for both pump polarisations, sample MR1168.

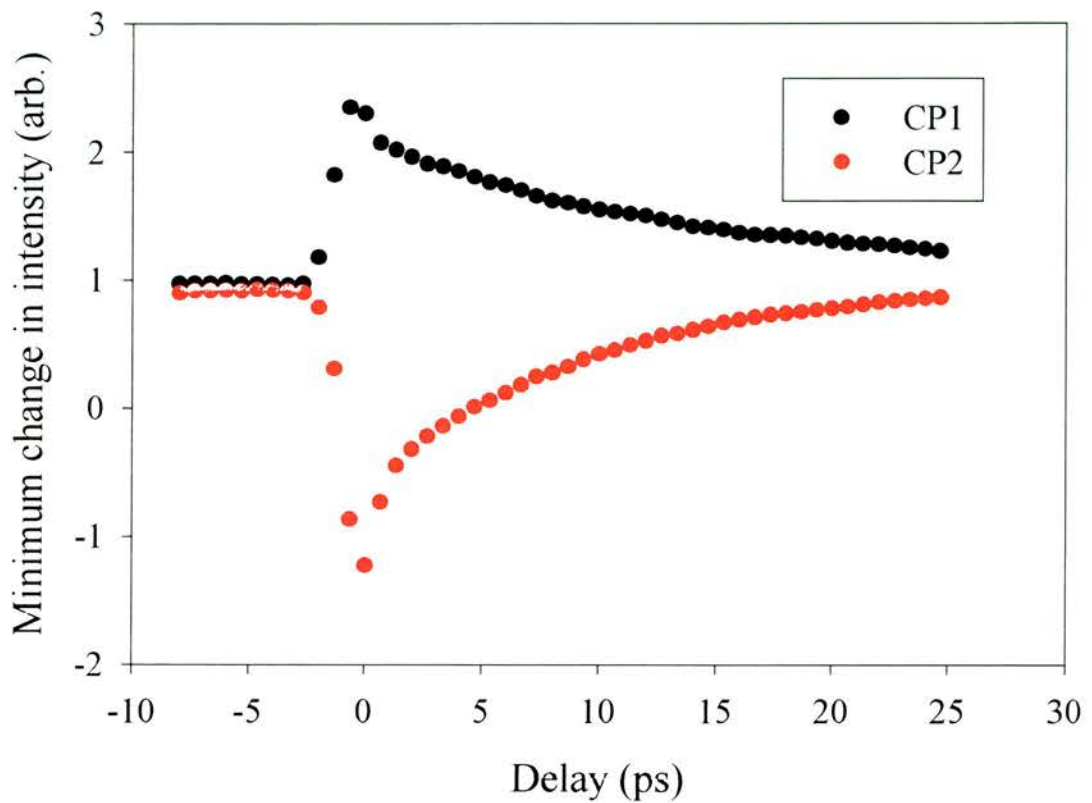


Figure 7-6 Minimum change in intensity as a function of delay for both circular polarisations, CP1 and CP2, for sample MR1168. This gives a measure of the absolute value of the minor axis of the ellipse.

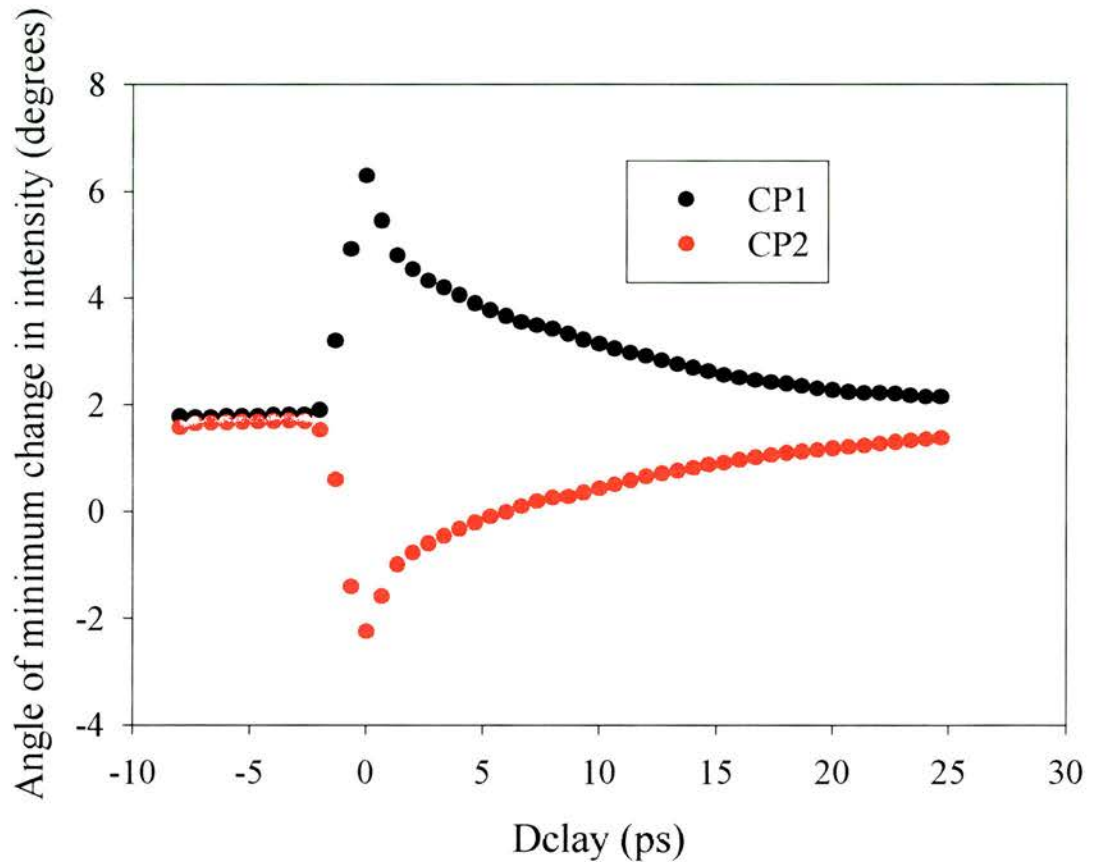
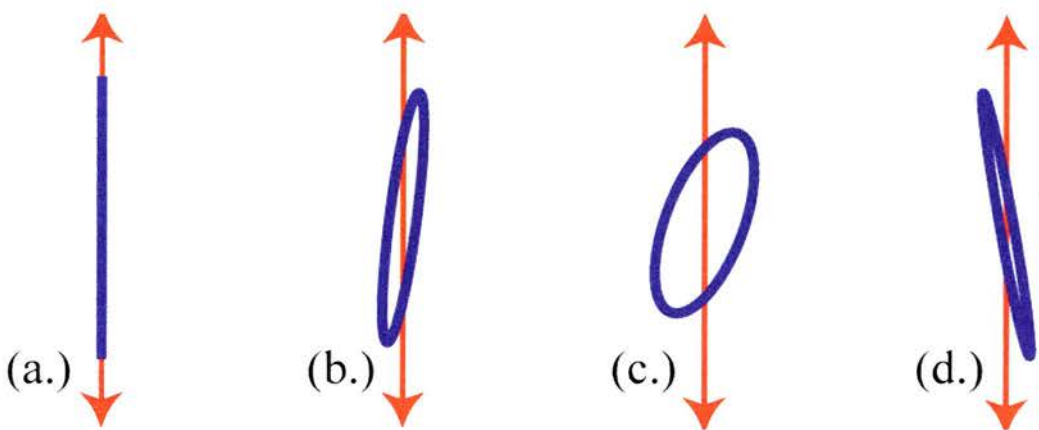


Figure 7-7 Angle of the minimum change in intensity as a function of angle for both circular polarisations of the pump pulse, CP1 and CP2, for sample MR1168. This gives a measure of the rotation of the minor axis of the ellipse.

### 7-5 Analysis

From Figure 7-6 and Figure 7-6 we can see that there is a rotation and increase in ellipticity before zero delay, 12 ns after the previous pulse. The effective positive switch increases the ellipticity and rotates the polarisation in the same direction. The effective negative switch has a decrease in ellipticity and rotates the polarisation in the opposite direction. This is schematically summarised in Figure 7-8. The initial polarisation will not be 100% linearly polarised due to reflections from and transmissions through the optical components.



*Figure 7-8 Schematic representation of the change in polarisation of the probe beam, (a.) before sample, (b.) before zero delay (12ns), (c.) after zero delay for one circular polarisation of pump (positive switch), (d.) after zero delay for the other circular polarisation of the pump (negative switch).*

These results could be explained by a long-lived spin relaxation component, a long-lived circular dichroism or a long-lived birefringence.

A long-lived spin relaxation has not been evident in any of the previous experiments, using the same OPO, detector and samples and outlined in Chapter 6.

A long-lived circular dichroism could come from a helix structure or an asymmetry in the spin relaxation times. InGaAsP is a cubic III-V semiconductor so there is no inbuilt

helix. For the spin relaxation time to be different for spin up to down than for spin down to up, therefore causing an inbuilt optical activity, there would have to be the existence of an asymmetry in the bandstructure. This is unlikely as even though the conduction band splits for the spin up and down states it is balanced on each side of  $k=0$ . We have  $E \uparrow(k) \neq E \downarrow(k)$  but  $E \uparrow(k) = E \downarrow(-k)$ . Any optical activity effects would not be dependent on the rotation of the sample.

It is unlikely that the sample is birefringent again due to the cubic structure. However, the quantum wells are grown on a very small wedge (0.03 degrees) so it is possible that this introduces birefringent effects into the sample.

Therefore, an experimental investigation of the rotational effects of the sample was performed.

### **7-6 Experimental set-up to determine the birefringence**

The birefringence was examined by using a one-beam experiment. Linear polarisation was passed through the sample and an analyser cross-polarised with the initial beam, Figure 7-9. The transmitted signal was measured as the sample was rotated.

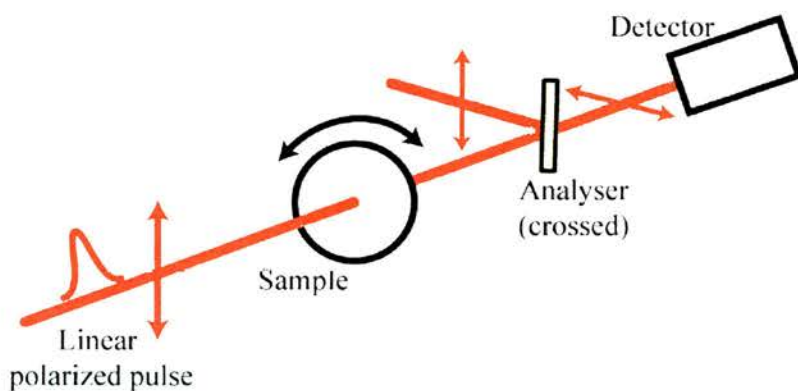


Figure 7-9 Experimental set-up to measure the birefringence of the sample.

The effect of excited carriers on the birefringence was measured by rotating the sample whilst in the switch configuration, Figure 7-1, at a constant time before zero delay (12ns).

### ***7-7 Birefringence results***

For the one beam experiment, the transmission through the analyser as the sample was rotated is shown in Figure 7-10. It is shown that there was a very distinct change in signal indicating a built-in birefringence.

The power dependency was measured at the positions of the sample where there is a maximum and a minimum signal from Figure 7-10. The relation of output power to input power is found to be linear as shown in Figure 7-11.

In the switch configuration, the transmission before zero delay is plotted as a function of the angle of the sample in Figure 7-12. The signal experiences a significant change as the sample is rotated.

Also in this configuration the scatter from the pump was investigated to look for any structural symmetry. It was found that at eight angles of the sample rotation there occurred a peak in the scatter, Figure 7-13. The scatter is the light from the pump beam that falls onto the detector. This is measured by blocking the probe beam and chopping the pump.

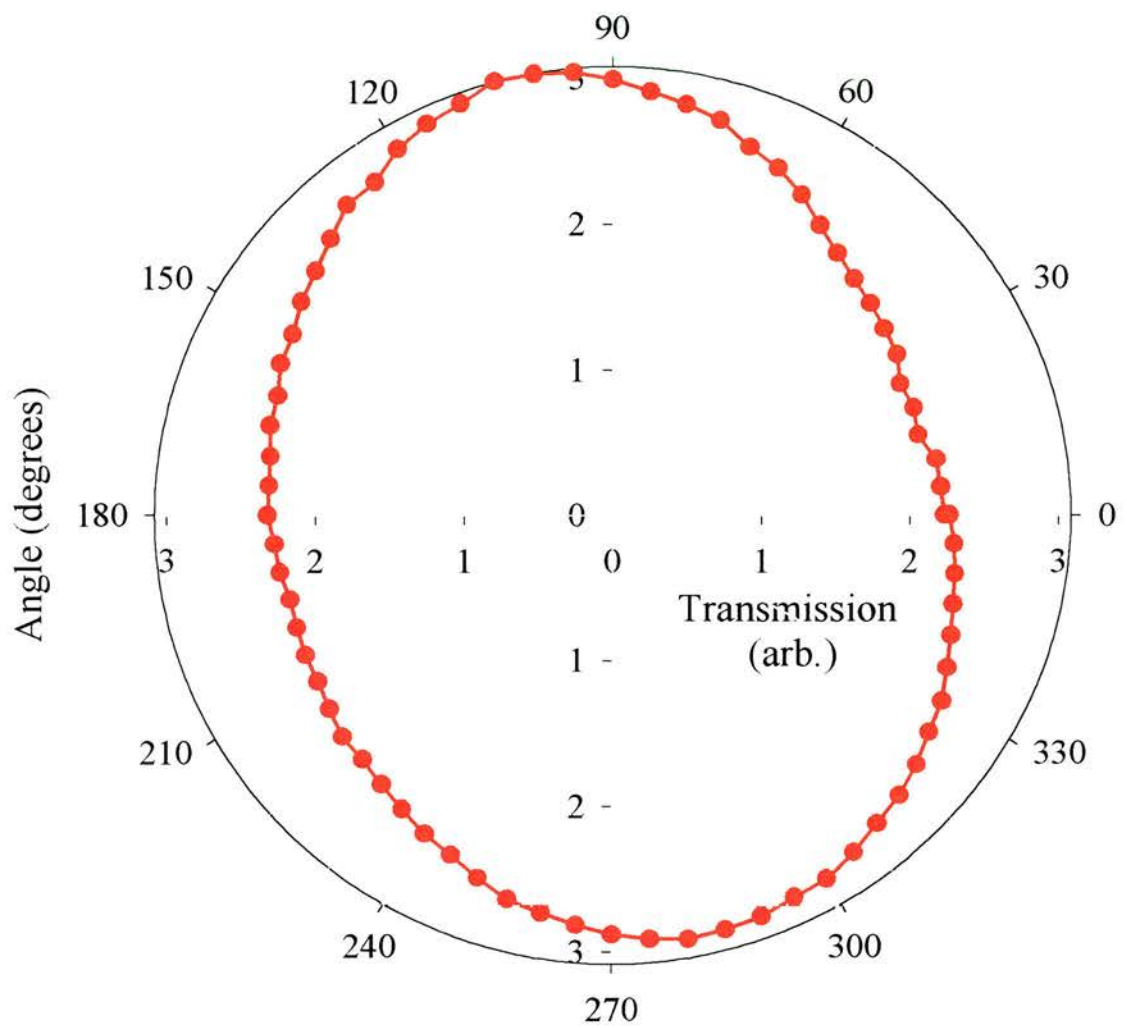


Figure 7-10 Transmission of a linear polarised beam through the sample and an analyser cross-polarised with the initial beam as a function of the angle of sample

MR1168.

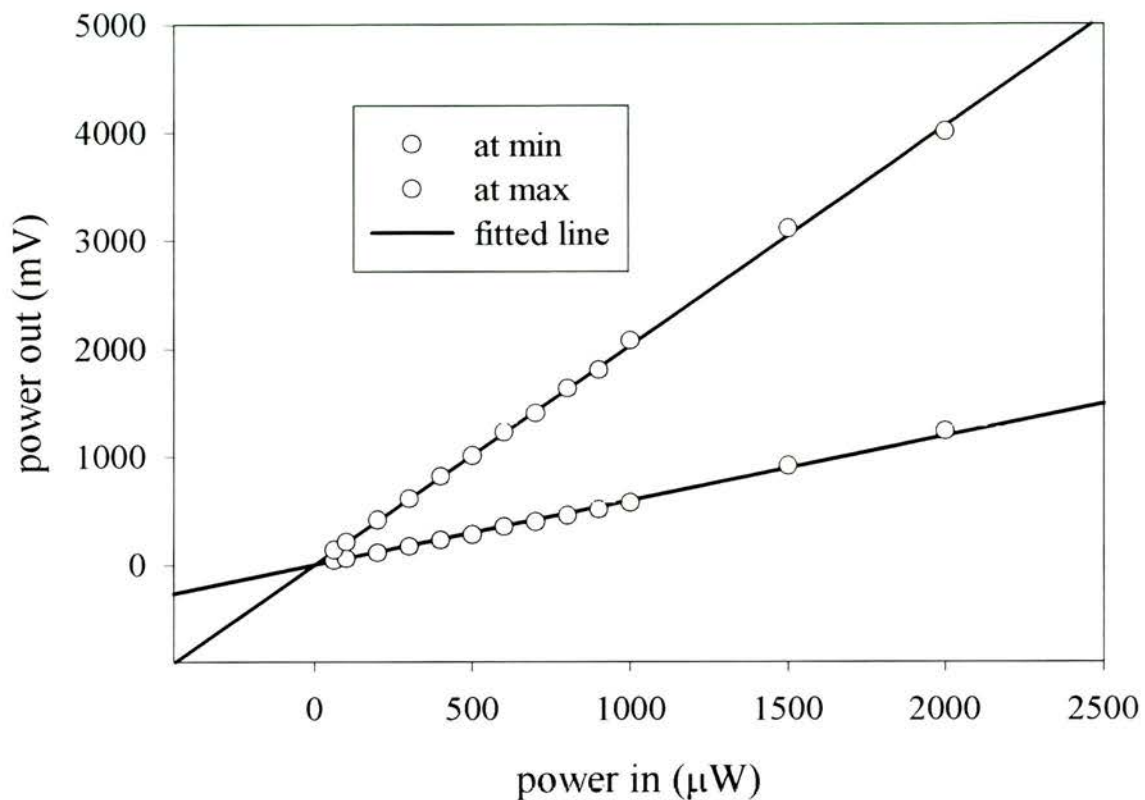


Figure 7-11 Power measured on the detector at the minimum and maximum signal through the analyser (when the sample was rotated) as a function of the input power.

The fitted lines are  $y=0.6x$  and  $y=2x$ .

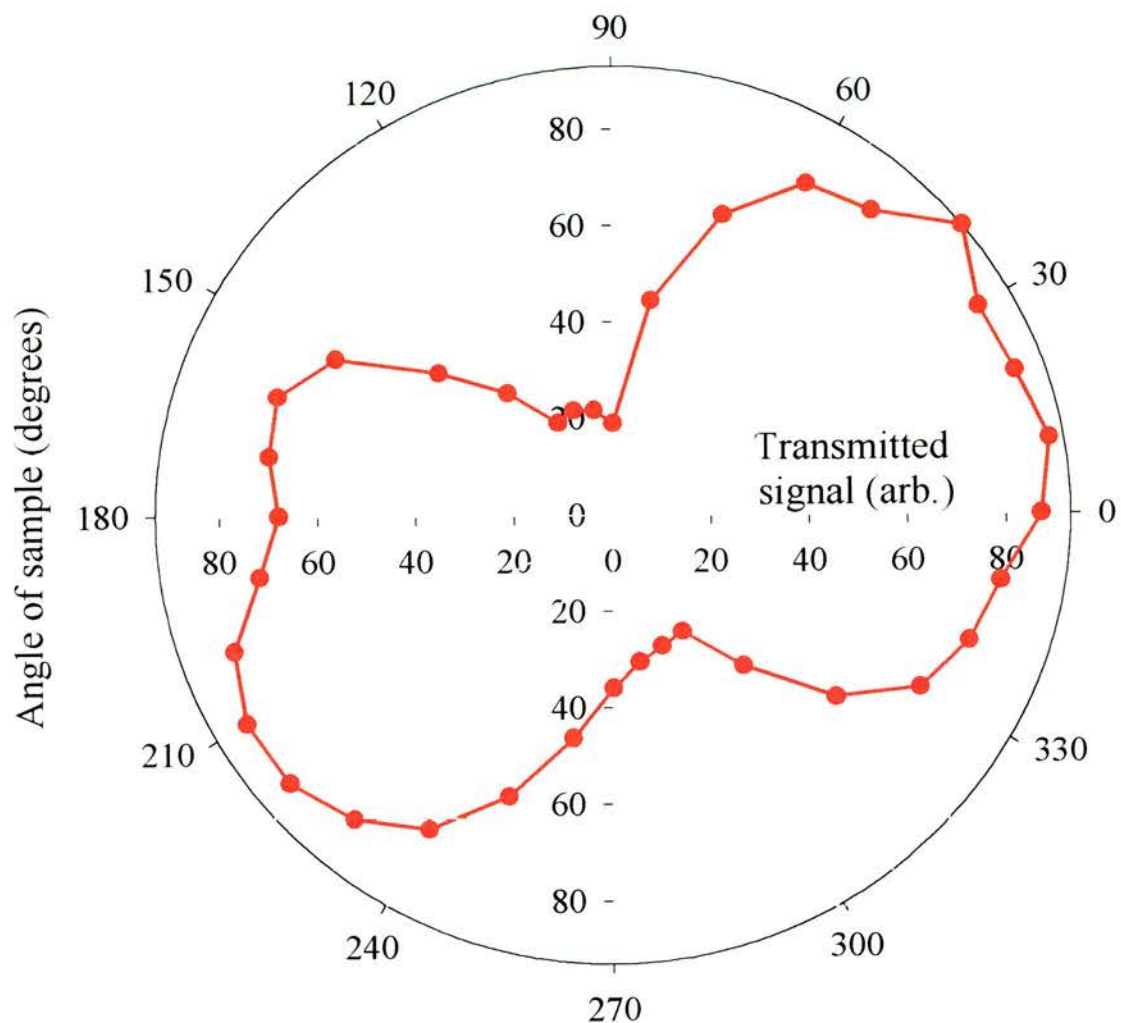


Figure 7-12 Transmitted signal of switch before zero delay as a function of the angle of sample MR1168.

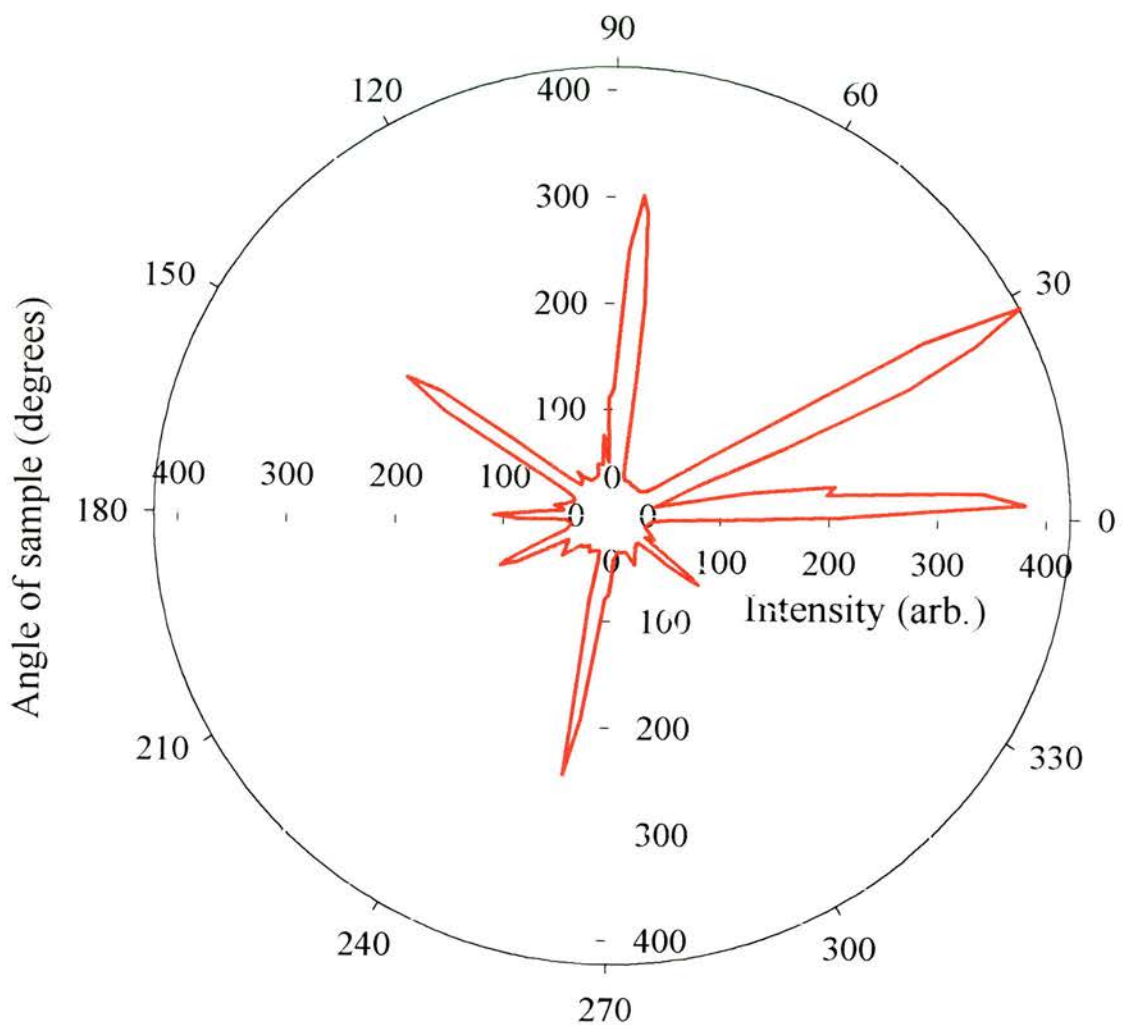


Figure 7-13 Intensity of pump scatter for sample MRI1168 as a function of the rotational angle of the sample.

### ***7-8 Combination of the switch and birefringence***

The results shown above conclude that there is an induced birefringence in the sample.

It is possible that this comes from the growth angle of the quantum wells. The small wedge (0.03 degrees) could be causing a form of stripe pattern. It is proposed that the long lifetime of the carriers enables observation of induced birefringence. This arises from the situation where there are still carriers in the wells from the previous pulse when the next pulse arrives and these carriers are increasing the ‘stripy’ effects in the sample.

In the all-optical switch configuration, the effective positive and negative switch findings are a consequence of the combined effects of the birefringence and the spin polarisation.

### ***7-9 Model of combination of spin polarisation and birefringence***

A mathematical model was produced in order to confirm that birefringence was the cause of the previously discussed results. This is based on the effects that a component with optical activity and/or birefringence would have on polarised light. A half waveplate and an analyser could also be included in the system.

Figure 7-14 shows the result of the situation where the pump induces a birefringence change in the sample and an analyser is included. The optical activity will go positive if pumped with one circular polarisation and negative when pumped with the other. It can be seen that, starting from zero optical activity, the signal will go positive or negative depending on the pump polarisation. Moreover, the signal at zero optical activity, i.e. no spin polarisation, is non-zero. This is only possible if the initial beam has a very slight ellipticity, in this case 0.01%. This agrees with the experimental results where the

optical activity increases at zero delay and then decays to nothing after the spin relaxation time.

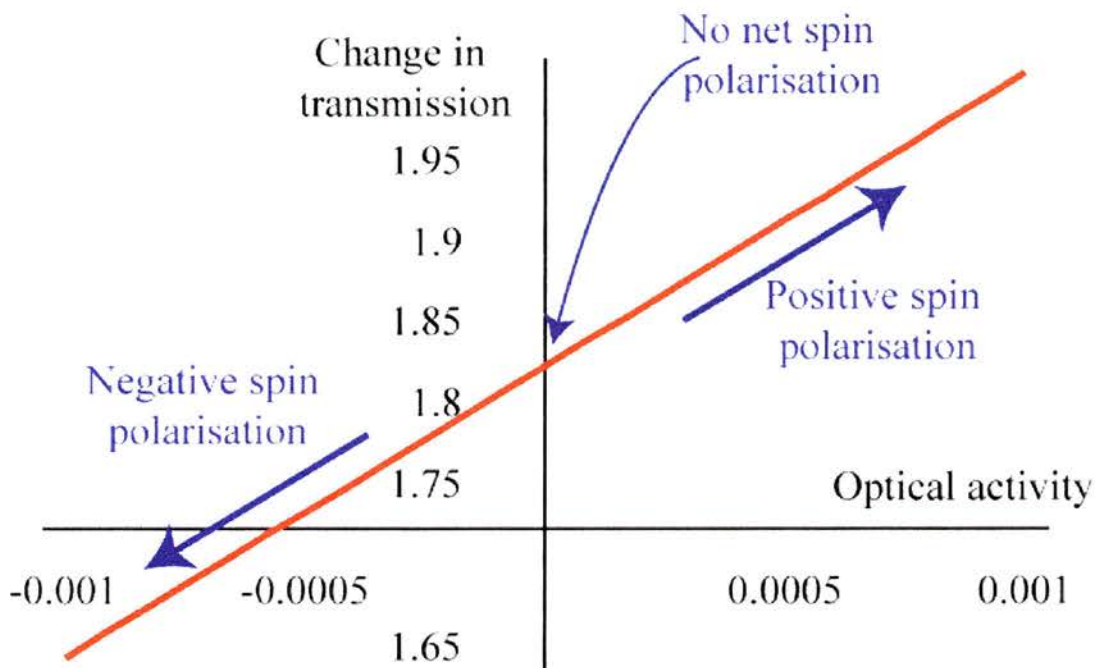


*Figure 7-14 Plot of the effects of an induced birefringence due to the pump. The change in transmission is shown as a function of the optical activity.*

The effect of sample rotation was modelled and the results are shown in Figure 7-15. This confirms that as the sample is rotated there is a change in the signal through the analyser but the switch doesn't flip, i.e. the positive switch doesn't become the negative switch and vice versa.

Figure 7-16 shows the model results for the change in transmission with and without a halfwave plate. Inserting a half wave plate theoretically causes the switch result to flip. When the half waveplate is rotated by  $\beta$  and therefore the analyser by  $2\beta$  this does not cause any change in the signal. These theoretical model graphs agree with the experimental results outlined earlier.

When the birefringence was set to zero in the model and only optical activity considered there was no change in the signal as the sample was rotated.

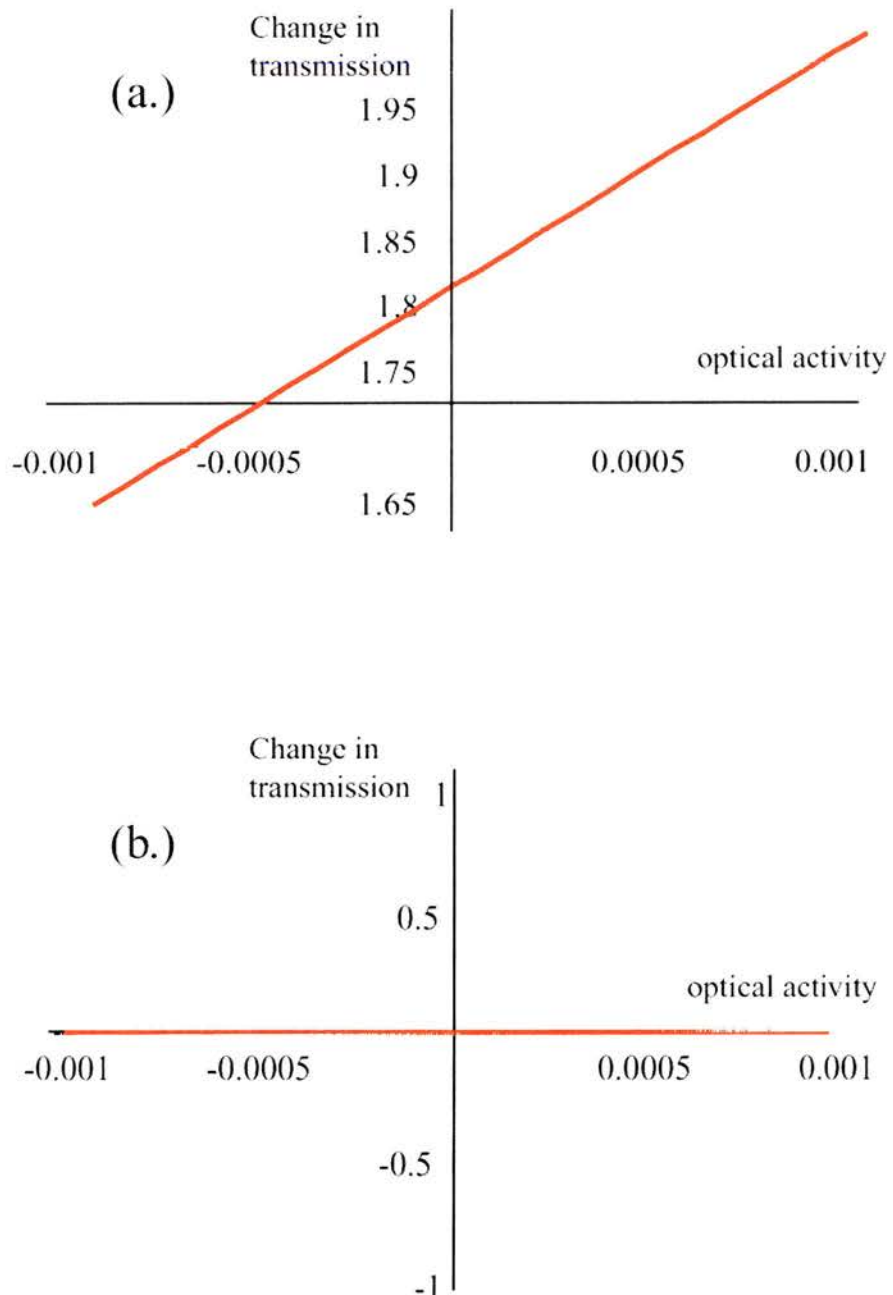


Figure 7-15 Model of the change in transmission as the sample is rotated where the change in rotation is plotted against optical activity. (a.) Sample positioned at 0 and 180 degrees. (b.) Sample positioned at 90 and 270 degrees.

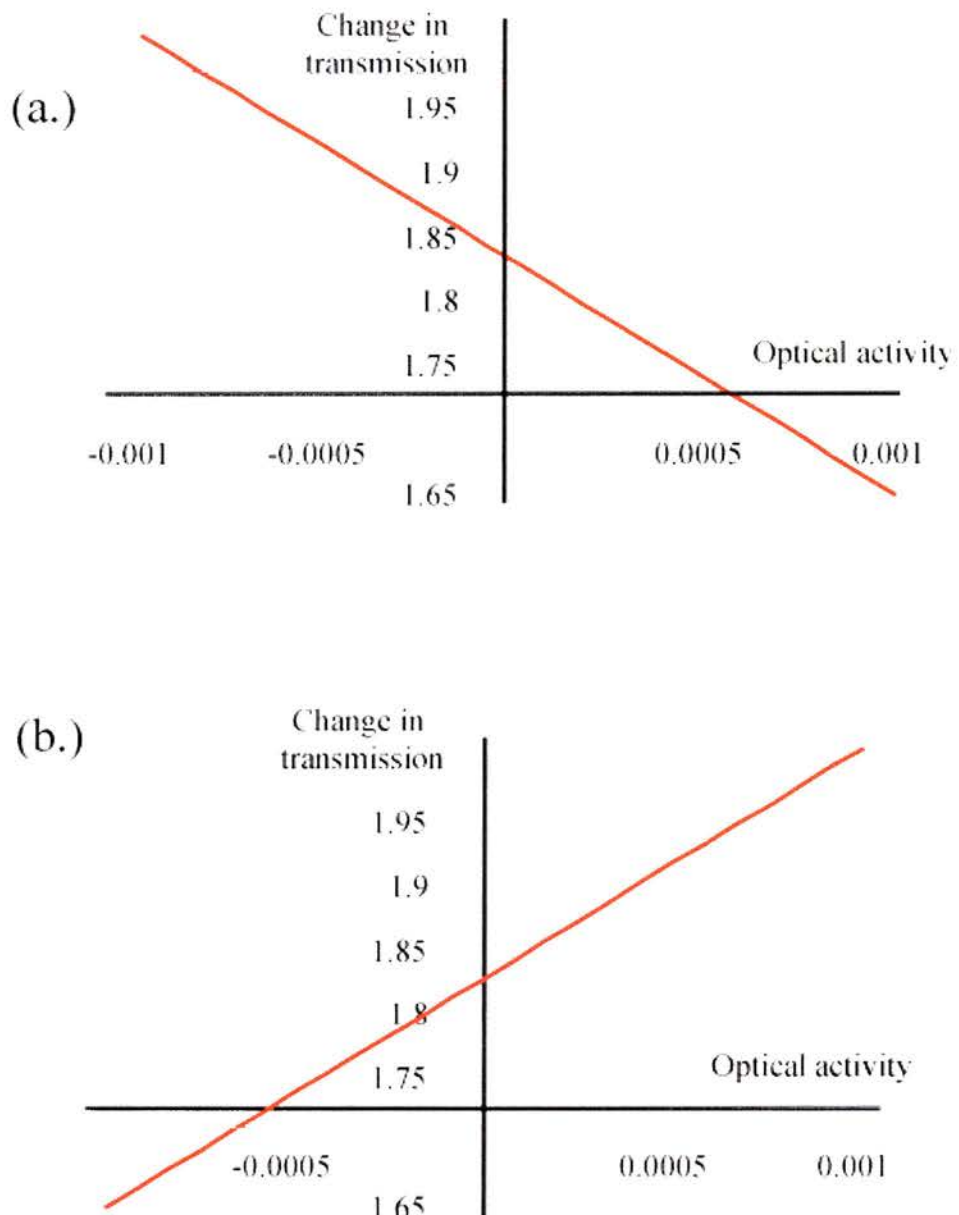


Figure 7-16 Change in transmission as a function of optical activity (a.) without a half waveplate and (b.) with a half waveplate in the probe beam.

### **7-10 Conclusion**

An all-optical polarisation switch has been demonstrated in InGaAs(P) MQW's at room temperature. Recovery times on the order of tens of picoseconds at 1.5 microns have been demonstrated.

A surprising birefringence effect has been discovered which results in an effective positive and negative switch. The creation of a two-state switch operating in this wavelength regime poses great opportunities in the communications industry.

The orientation of the switch is dependent on the circular polarisation of the pump beam. The insertion of a half wave plate enables the switch to be flipped from effective positive to negative and vice versa. The experimental results have been found to agree with mathematical modelling.

The symmetry of the crystal lattice in a zinc blende structure should not enable the production of birefringence. Therefore, the existence of birefringence in sample MR1168 was unexpected. The most probable explanation is that the birefringence comes from the growth angle of the samples. A wedged substrate is used to enable the growth of InGaAsP quantum wells. This creates a stripe pattern in the samples. From Figure 7-13 we can see that there is a grating effect causing increased scatter at eight angles of the sample over a full rotation. This implies a structural effect.

When the carriers are excited they fall into these steps and this introduces an asymmetry. We propose that the birefringence is enhanced due to the excited carriers in the wells being aligned along the steps. This is observed in these samples due to the long carrier lifetime, as there are still a large number of excited carriers left over from the previous pulse when the next pulse arrives.

### 7-11 Bibliography

- 1 S. Clavenna, "Optical switching evolves beyond device market," *Laser Focus World*, pp. 10, Supp. April 2000.
- 2 N. A. Riza and S. Sumriddetchkajorn, "Small-tilt micromirror-device-based multiwavelength three-dimensional 2x2 fiber optic switch structures," *Optical Engineering*, **39** (2), pp. 379-386, 2000.
- 3 A. M. Kanan, P. LiKamWa, MitraDutta, and J. Pamulapati, "1.7-ps consecutive switching in an integrated multiple-quantum-well Y-junction optical switch," *IEEE Photonics Technology Letters*, **8** (12), pp. 1641-1643, 1996.
- 4 P. LiKamWa and A. M. Kanan, "Ultrafast all-optical switching in multiple-quantum-well Y-junction waveguides at the band gap resonance," *IEEE Journal of Selected Topics in Quantum Electronics*, **2** (3), pp. 655-660, 1996.
- 5 G. I. Stegeman and A. Miller, in *Photonics in Switching - Background and components; Vol. I*, edited by J. E. Midwinter (Academic Press, Inc., London, 1993), p. 81-146.
- 6 H. M. Gibbs, S. L. McCall, T. N. C. Venkatesan, A. C. Grossard, A. Pasner, and W. Weigmann, "Optical bistability in semiconductors," *Appl. Phys. Lett.*, **35**, pp. 451-453, 1979.
- 7 D. A. B. Miller, S. D. Smith, and J. Johnston, "Optical bistability and signal amplification in a semiconductor crystal: Applications of new low-power nonlinear effects in InSb," *Appl. Phys. Lett.*, **35**, pp. 658-660, 1979.

- 8 H. S. Loka and P. W. E. Smith, "Ultrafast all-optical switching with an asymmetric Fabry-Perot device using low-temperature-grown GaAs: Material and device issues," *IEEE J. of Quantum Electron.*, **36** (1), pp. 100-111, 2000.
- 9 D. A. B. Miller, D. S. Chemla, T. C. Damen, A. C. Gossard, W. Wiegmann, T. H. Wood, and C. A. Burrus, "Band-Edge Electroabsorption in Quantum Well Structures: The Quantum-Confinement Stark Effect," *Phys. Rev. Lett.*, **53** (22), pp. 2173-2176, 1984.
- 10 D. A. B. Miller, "Quantum-Well Self-Electro-Optic Effect Devices," *Opt. and Quant. Elect.*, **22**, pp. S61-S98, 1990.
- 11 D. Hulin, A. Mysyrowicz, A. Antonetti, A. Migus, W. T. Masselink, H. Morkoc, H. M. Gibbs, and N. Peyghambarian, "Ultrafast all-optical gate with subpicosecond On and OFF response time," *Appl. Phys. Lett.*, **56**, pp. 993-995, 1986.
- 12 R. Takahashi, Y. Kawamura, and H. Iwamura, "Ultrafast 1.55 Micron All-Optical Switching Using Low-Temperature-Grown Multiple Quantum Wells," *Appl. Phys. Lett.*, **68** (2), pp. 153-155, 1996.
- 13 Y. Nishikawa, A. Tackeuchi, M. Yamaguchi, S. Muto, and O. Wada, "Ultrafast All-Optical Spin Polarisation Switch Using Quantum-Well Etalon," *IEEE J. of Selected Topics in Quant. Elect.*, **2** (3), pp. 661-667, 1996.
- 14 J. T. Hyland, G. T. Kennedy, A. Miller, and C. C. Button, "Picosecond all-optical polarization switching in InGaAsP MQW's at 1.52  $\mu\text{m}$ ," *IEEE Photonics Technol. Lett.*, **10** (10), pp. 1419-1421, 1998.
- 15 J. T. Hyland, Thesis, University of St Andrews, 1999.

- 16 D. D. Awschalom and N. Samarth, "Electron precession and coherence in magnetic quantum structures: Room-temperature spin memory," *Solid State Commun.*, **107** (11), pp. 663-672, 1998.
- 17 D. D. Awschalom and J. M. Kikkawa, "Electron spin and optical coherence in semiconductors," *Physics Today*, **52** (6), pp. 33-38, 1999.
- 18 A. P. Heberle, J. J. Baumberg, E. Binder, T. Kuhn, K. Kohler, and K. H. Ploog, "Coherent control of exciton density and spin," *IEEE Journal of Selected Topics in Quantum Electronics*, **2** (3), pp. 769-775, 1996.

## Chapter 8

# Transient Grating Studies

### ***8-1 Summary***

This chapter describes amplitude and polarisation transient grating experiments. The ambipolar and electron diffusion coefficients are deduced for an InGaAsP MQW sample.

### ***8-2 Introduction***

The design and operation of quantum well devices depends on knowledge of the carrier transport within the wells. One technique that has been used extensively to probe these properties is time resolved, degenerate four-wave mixing (DFWM)<sup>1-3</sup>. The use of three input beams consisting of ultrashort pulses resonant with the heavy hole exciton allows monitoring of the spatial dynamics of optically excited free carriers and excitons. Amplitude and spin gratings formed by two excite beams of parallel or crossed polarisation can be used to determine room temperature ambipolar and electron diffusion coefficients ( $D_a$  and  $D_e$ ) respectively. The ambipolar diffusion coefficient represents the combined diffusion of electrons and holes.

The amplitude grating method has been employed previously to study ambipolar diffusion in bulk samples of silicon<sup>4</sup>, germanium<sup>5</sup>, GaAs<sup>6</sup>, InP<sup>6</sup>, Cd compounds<sup>7,8</sup> and ZnSe<sup>9</sup>. InAs/GaAs MQWs<sup>10</sup> and InAs/GaAs hetero-nipi structures at room temperature and InGaAs/GaAs superlattices<sup>11</sup> at low temperatures have also been studied by this method.

Both amplitude and polarisation gratings have been used to investigate in-well carrier transport properties of GaAs/AlGaAs MQWs at room temperature<sup>2,3,12</sup>. An ambipolar

diffusion coefficient of  $13.3 \text{ cm}^2/\text{s}$  and electron diffusion coefficient of  $127 \text{ cm}^2/\text{s}$  were determined.

Line-width measurements from nearly degenerate FWM have measured the ambipolar diffusion coefficient for a strained InGaAsP semiconductor optical amplifier (SOA) operating at 1.3 microns as  $8.0 \text{ cm}^2/\text{s}$ <sup>13</sup>. Light induced grating measurements of bulk-like epitaxial layers at 1.5 microns have determined a value of  $7.4 \text{ cm}^2/\text{s}$ <sup>14</sup>.

### ***8-3 Amplitude Gratings***

#### **8-3-1 Formation of an amplitude grating**

In the forward travelling geometry of a transient grating two pulses of equal intensity and the same linear polarisation are co-incident on a sample at angles of  $\theta$  and  $-\theta$  from the normal. They interfere to give a squared sinusoidal intensity modulation along the wells as shown in Figure 8-1. Carrier generation will produce a modulation of the optical properties to form a temporal grating. If a third pulse is then incident perpendicular to the grating it will be diffracted with an angle  $\phi$  with an efficiency dependent on the nonlinear optical interaction.

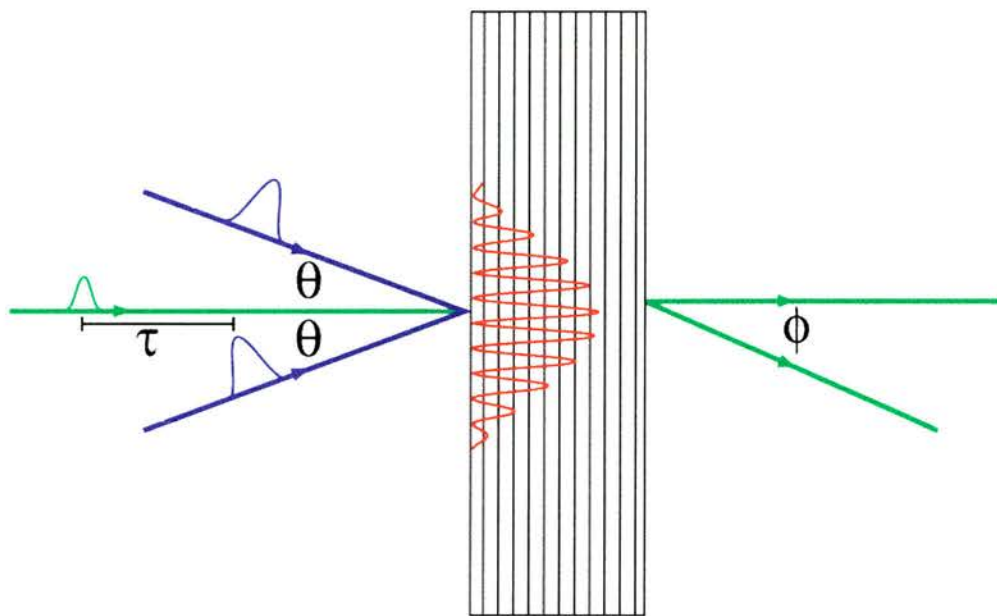


Figure 8-1 Incident angles for grating experiments.

This deflected angle will depend on the grating period,  $\Lambda$ . In order to calculate the grating period we consider two plane waves crossing at angle  $2\theta$ , Figure 8-2.

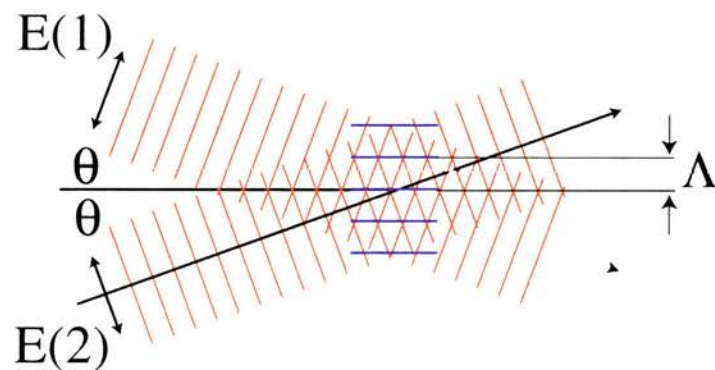


Figure 8-2 Calculation of the grating period.

For a given wavelength,  $\lambda$ , the grating spacing will then be given by:

$$\Lambda = \frac{\lambda}{2 \sin \theta} \quad (8.1)$$

and the diffraction angle,  $\phi$ , by:

$$\sin \phi = \frac{\lambda}{\Lambda} = 2 \sin \theta \quad (8.2)$$

### 8-3-2 Amplitude grating decay

If the creation of the grating is due to ultrashort pulses then the grating itself will be time dependent. When resonant with the heavy hole exciton absorption feature the resulting brief interference pattern produces a temporal modulation of the free-carriers. This modulation will decay through carrier recombination and diffusion. Since equal densities of electrons and holes are present this will be ambipolar. A third time-delayed probe pulse will be diffracted from the grating due to the excitonic optical nonlinearities induced by the carriers.

The diffraction efficiency,  $\eta$ , for a thin sinusoidal grating is given by a first-order Bessel function:

$$\eta = \left| J_1 \left( \frac{2\pi n_{eh}}{\lambda} + \frac{i\sigma_{eh}}{2} \right) N \left( \frac{1 - \exp(-\alpha l)}{\alpha} \right) \right|^2 \exp(-\alpha l) \quad (8.3)$$

where  $\alpha$  is the average absorption coefficient,  $l$  is the sample thickness,  $N$  is the density of carriers at the peak of the fringe and  $n_{eh}$  is defined by:

$$n_{eh} = \frac{\Delta n}{N} \quad (8.4)$$

where  $\Delta n$  and  $N$  are the change in refractive index and density of optically generated electron-hole pairs respectively.

For moderate diffraction efficiencies and including only the refractive terms, (8.3) reduces to:

$$\eta = \left( \frac{\pi n_{eh} N l_\alpha}{\lambda} \right)^2 \exp(-\alpha l) \quad (8.5)$$

The diffraction efficiencies are proportional to the square of the modulation depth of the refractive index. Therefore, if the grating decay is characterised by a rate constant,  $\Gamma$ , the diffraction efficiency decays at twice this rate,  $2\Gamma$ :

$$\eta = \exp(-2\Gamma t) \quad (8.6)$$

The use of ultrashort pulses enables assumption of instantaneous excitation at  $t=0$ . The following decay of the initial carrier distribution,  $N(0,0)$ , is characterised by the recombination and diffusion lifetimes,  $\tau_R$  and  $\tau_D$ :

$$N(x,t) = \frac{N(0,0)}{2} \left[ 1 + 1 \cos\left(\frac{2\pi x}{\Lambda}\right) \exp\left(-\frac{t}{\tau_D}\right) \right] \exp\left(-\frac{t}{\tau_R}\right) \quad (8.7)$$

The continuity of excess carriers along the wells is:

$$\frac{\partial N(x,t)}{\partial t} = D_a \nabla^2 N(x,t) - \frac{N(x,t)}{\tau_R} \quad (8.8)$$

Substituting (8.7) into (8.8) gives:

$$\frac{4\pi^2 D_a}{\Lambda^2} - \frac{1}{\tau_D} = 0 \quad (8.9)$$

Grating decay occurs due to a combination of diffusion and recombination:

$$\Gamma = \frac{1}{\tau_D} + \frac{1}{\tau_R} \quad (8.10)$$

Substituting (8.10) into (8.9) gives a grating decay:

$$\Gamma = \frac{4\pi^2 D_a}{\Lambda^2} + \frac{1}{\tau_R} \quad (8.11)$$

Therefore, plotting the diffraction efficiency decay rate,  $2\Gamma$ , against  $\frac{8\pi^2}{\Lambda^2}$  gives a gradient which is equal to the ambipolar diffusion coefficient.

## 8-4 Spin Gratings

### 8-4-1 Formation of a spin grating

Two intersecting beams of opposite polarisation will result in uniform light amplitude. However, the electric field polarisation will be spatially modulated across the excitation region. For equal excitation intensities, the polarisation changes through linear to circular to orthogonal to circular of the opposite sense and back to linear across the surface of the sample. The modulation period is dependent on the angle of the two beams.

The electric field modulation  $E(x)$  along the polarisation grating can be expressed in terms of two circularly polarised components<sup>12</sup>:

$$E(x) = E_0 \left[ \sin\left(\frac{\pi x}{\Lambda}\right) e^{\frac{-i\pi}{4}} \frac{\hat{x} + i\hat{y}}{\sqrt{2}} + \cos\left(\frac{\pi x}{\Lambda}\right) e^{\frac{i\pi}{4}} \frac{\hat{x} - i\hat{y}}{\sqrt{2}} \right] + c.c \quad (8.12)$$

where  $\Lambda$  is the grating spacing and  $\hat{x}$  and  $\hat{y}$  are unit vectors describing the polarisation directions of the incident beams. Therefore, a nonlinearity that is sensitive to circular polarisation will create a grating from two oppositely polarised beams.

Interband selection rules<sup>15</sup> as discussed in section 2-4-3 allow the formation of 100% spin polarized electrons when circularly polarised light is resonant with the heavy hole exciton. Therefore, a polarisation grating will also result in the formation of an electron spin grating. A linearly polarised probe, which is a combination of left and right circularly polarised light, will then be deflected from this grating because of the spin dependent PSF component of the exciton saturation. The spin grating can decay by diffusion and spin relaxation,  $\tau_s$ . Due to the fast hole spin relaxation, the holes will be uniform in both concentration and spin on picosecond timescales so that only the electron diffusion,  $D_e$ , need be considered.

### 8-4-2 Spin grating decay

The difference in the population of spin up and spin down excitons and free carriers can be defined as  $\delta_{ex}$  and  $\delta_{fc}$  respectively. In order to model what is happening we must consider the continuity equations for these spin differences (Chapter 6):

$$\frac{d\delta_{ex}}{dt} = D_e \nabla^2 \delta_{ex} - \left( \frac{1}{\tau_2} + \frac{1}{\tau_3} + \frac{2}{\tau_s} \right) \delta_{ex} + G^+ - G^- \quad (8.13)$$

$$\frac{d\delta_{fc}}{dt} = D_e \nabla^2 \delta_{fc} + \frac{1}{\tau_3} \delta_{ex} - \left( \frac{1}{\tau_1} + \frac{2}{\tau_s} \right) \delta_{fc} \quad (8.14)$$

where  $D_e$  is the electron diffusion coefficient,  $\tau_1$  and  $\tau_2$  are the free carrier and exciton recombination times,  $\tau_3$  is the exciton ionisation time and  $\tau_s$  is the spin relaxation time. Assuming the intensity profile of the excitation is Gaussian, the excitations of the two circular polarisations  $G^+$  and  $G^-$  can be expressed as:

$$G^\pm = g_0 \exp\left(-\frac{t^2}{\Delta t_0^2}\right) \left(1 \pm \cos \frac{2\pi x}{\Lambda}\right) \quad (8.15)$$

Also assuming that the difference in recombination times of the free carriers and excitons is negligible and therefore denoted by  $\tau_R$ , the solutions of (8.13) and (8.14) are the form:

$$\begin{aligned} \delta_{ex}(x, t) &= a \cos\left(\frac{2\pi x}{\Lambda}\right) \exp\left(-t\left(\frac{1}{\tau_R} + \frac{1}{\tau_3} + \frac{2}{\tau_s} + \frac{4D_e\pi^2}{\Lambda^2}\right)\right) \\ &\times \left[ 1 + \operatorname{erf}\left(\frac{2t - \left(\frac{1}{\tau_R} + \frac{1}{\tau_3} + \frac{2}{\tau_s} + \frac{4D_e\pi^2}{\Lambda^2}\right)\Delta t_0^2}{2\Delta t_0}\right) \right] \end{aligned} \quad (8.16)$$

$$\begin{aligned}
 \delta_{fc}(x,t) = & b \cos\left(\frac{2\pi x}{\Lambda}\right) \exp\left(-t\left(\frac{1}{\tau_R} + \frac{2}{\tau_s} + \frac{4D_e\pi^2}{\Lambda^2}\right)\right) \\
 & \times \operatorname{erf}\left(\frac{2t - \left(\frac{1}{\tau_R} + \frac{2}{\tau_s} + \frac{4D_e\pi^2}{\Lambda^2}\right)\Delta t_0^2}{2\Delta t_0}\right) \\
 = & -c \cos\left(\frac{2\pi x}{\Lambda}\right) \exp\left(-t\left(\frac{1}{\tau_R} + \frac{1}{\tau_3} + \frac{2}{\tau_s} + \frac{4D_e\pi^2}{\Lambda^2}\right)\right) \\
 & \times \operatorname{erf}\left(\frac{2t - \left(\frac{1}{\tau_R} + \frac{1}{\tau_3} + \frac{2}{\tau_s} + \frac{4D_e\pi^2}{\Lambda^2}\right)\Delta t_0^2}{2\Delta t_0}\right)
 \end{aligned} \tag{8.17}$$

Erf is the general error function that is shown graphically in Figure 8-3 and is given by:

$$Erf = \frac{2}{\sqrt{\pi}} \int_0^z e^{-t^2} dt \tag{8.18}$$

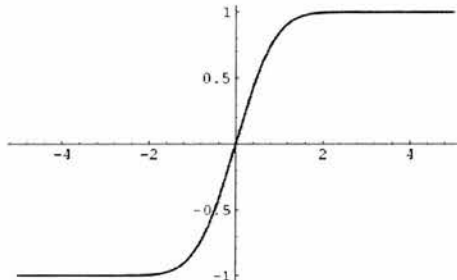


Figure 8-3 The Erf function

The diffraction efficiency is proportional to the square of the carrier density (for carrier density see equation (8.7)), therefore:

$$\eta \propto (a_{ex}\delta_{ex}(\max) + a_{fc}\delta_{fc}(\max))^2 \tag{8.19}$$

where  $a_{ex}$  and  $a_{fc}$  are constants.

$\tau_3$ , the ionisation time, is very small compared to the relaxation times. This means that all the Erf function terms in equations (8.16) and (8.17) can be simplified to Gaussian peaks. This comes from mathematical simplifications of this step-like function.

Therefore, the square root decay of the spin grating can then be fitted with a Gaussian peak plus the product of an exponential and an erf function.

### ***8-5 Experimental set-up***

The experimental set-up used for degenerate four wave mixing experiments is described in Chapter 3. For the creation of an amplitude grating the two excitation beams are linearly polarised. In the spin grating case, a half-wave plate rotates one of the pump beams to allow the production of two orthogonal polarised pump beams. In both cases, a linearly polarised probe beam is used to monitor the grating decay. The sample used for this experiment was MR1168.

## ***8-6 Results***

### ***8-6-1 Two beam interference***

The coherence width of the pulses can be investigated by using a two-beam interference configuration. Only one of the pump beams is set to be incident on the sample. Consequently, the probe will be diffracted as it is temporally passed through the pump pulse for the time that the pulses are coherent.

As the probe is scanned through the pump its diffracted intensity is measured. This is shown in Figure 8-4. The coherence width of the pulse was found to be 1.5ps. This is in agreement with the value from the intensity autocorrelation of the OPO, reported in section 3-9.

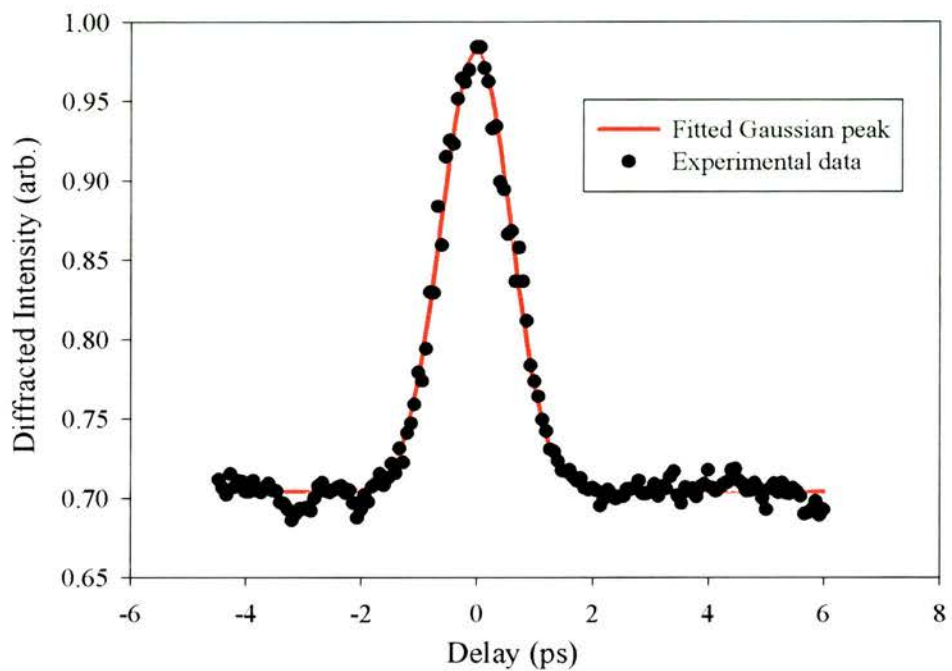


Figure 8-4 Two beam diffraction of the OPO.

### 8-6-2 Time resolved amplitude gratings

With the two pump beams creating an amplitude grating, the intensity of the diffracted probe signal was monitored as a function of delay for a range of gratings. The grating period was changed by altering the angle between the two excite beams. Results were taken for gratings spacings of 4, 4.4, 4.5, 4.7, 5.1, 5.2, 5.3, 6.0 and 6.3 microns. The measured signals were fitted with exponential decays.

Figures 8-5, 8-6 and 8-7 show the decay of the diffracted signal for grating periods of 6.3, 4.7 and 4 microns with fitted decay times of 530, 370 and 285 ps respectively.

All the decay times were found to be significantly less than the recombination time, which was on the order of nanoseconds (chapter 5). This implies that the grating decay was only caused by the carrier diffusion along the wells.

The diffraction efficiency,  $2\Gamma$ , was plotted against  $8\pi^2/\Lambda^2$  as shown in Figure 8-8. A straight line fit to the data gives a gradient of the ambipolar diffusion coefficient and a y intersection of  $2/\tau_R$  (see Equation (8.11)). We see that the intersection is effectively zero, consistent with the long recombination time.

The amplitude grating was probed by both orientations of linear and circular polarisations. The decay was found to be the same in each case, Figure 8-9, confirming that this grating is only due to amplitude modulation and the decay dominated by ambipolar diffusion

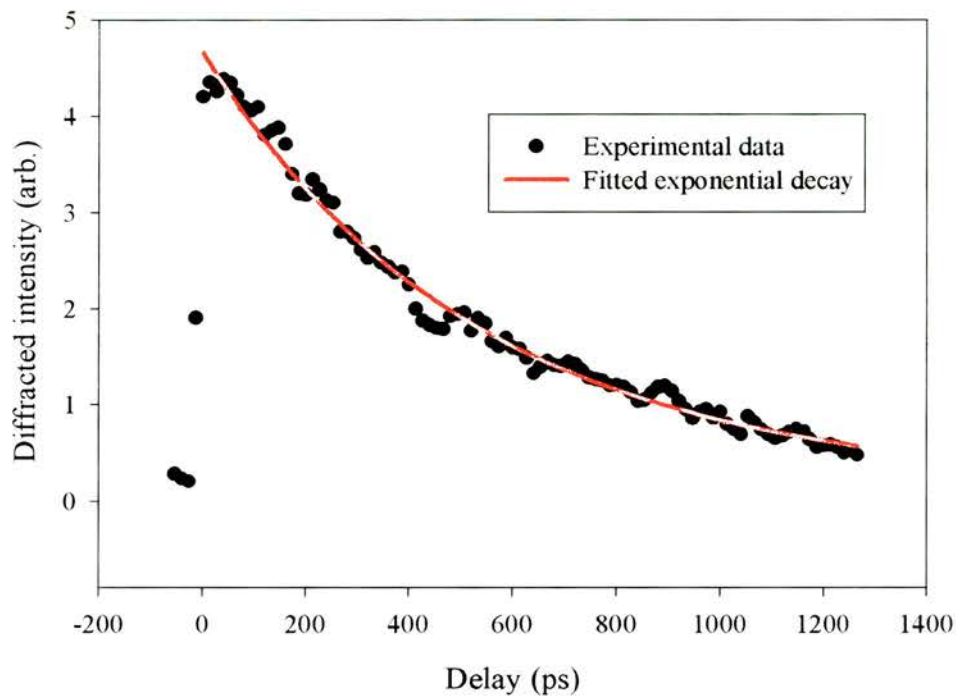


Figure 8-5 Diffraction intensity for a 6.3 micron grating with 530 ps decay time.

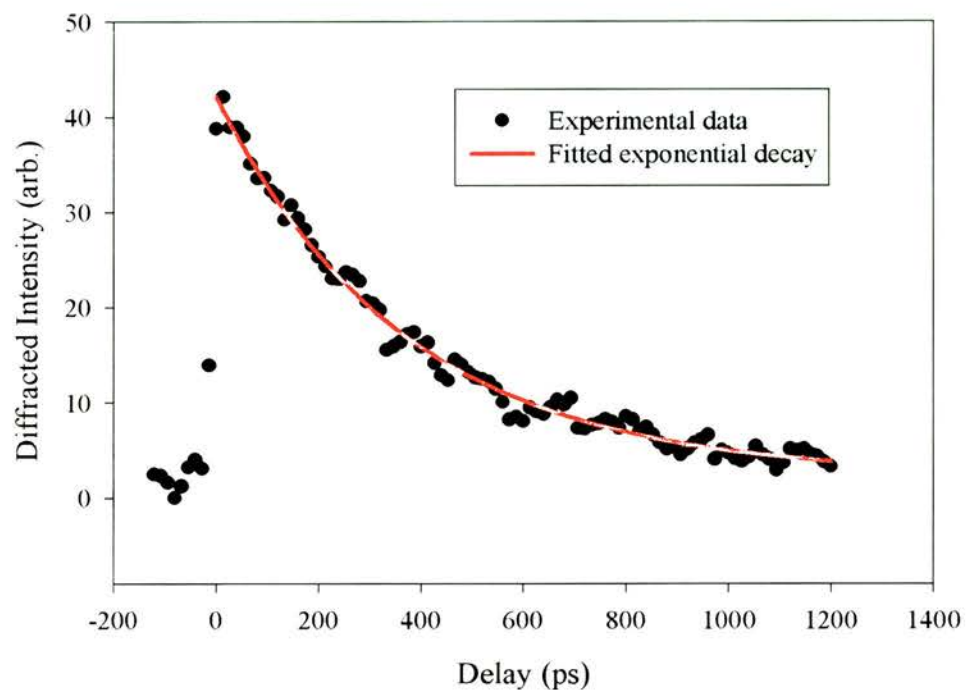


Figure 8-6 Diffraction intensity for a 4.7 micron grating with 370 ps decay time.

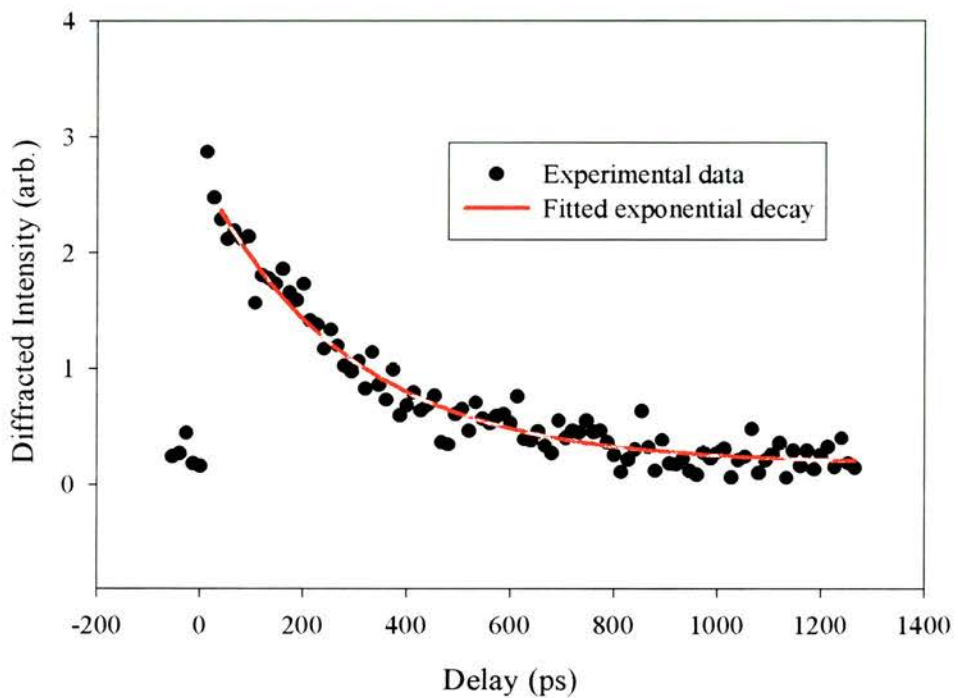


Figure 8-7 Diffraction intensity for a 4 micron grating with 285 ps decay time.

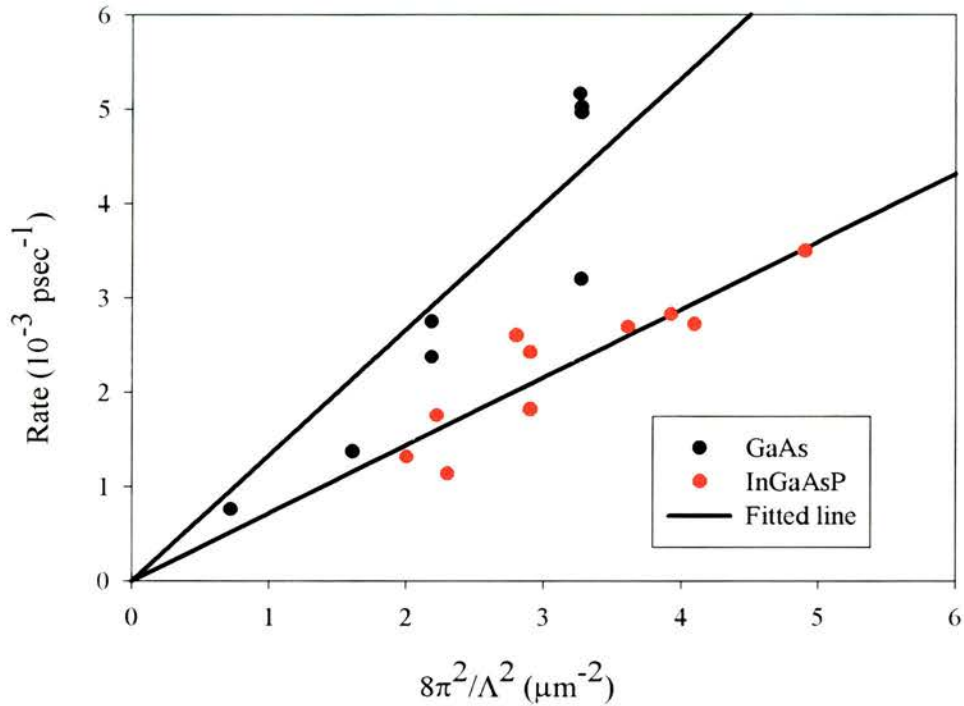


Figure 8-8 Measured grating decay rates of the diffracted signal against  $8\pi^2/\Lambda^2$  for InGaAsP (black points). Also plotted are the GaAs decay rates for comparison. The gradient gives the ambipolar diffusion coefficient of  $7.2\text{cm}^2/\text{s}$ .

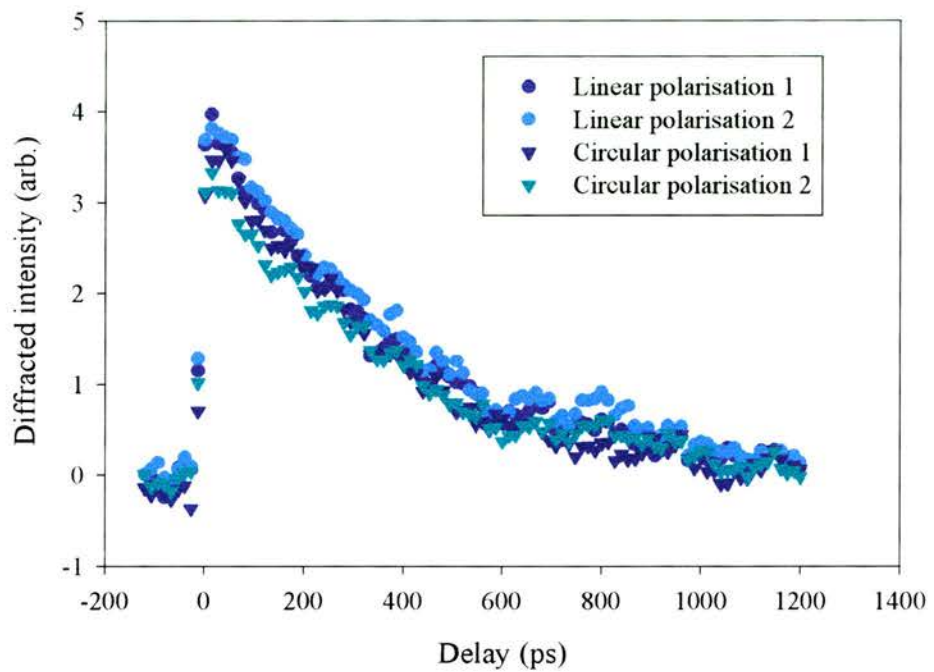


Figure 8-9 Diffracted intensity decay for orthogonal linear and opposite circular polarisations.

### 8-6-3 Time resolved spin gratings

The spin grating uses a linearly polarised probe beam that can be expressed as two opposite circular polarisations. It has already been observed for GaAs that the diffracted signal is rotated by  $\pi/2$  due to the two polarisation components of the grating being shifted in phase by  $\pi$  with respect to one another<sup>16</sup>. This was confirmed to be the case here by inserting an analyser into the diffracted signal path between the sample and detector and finding a maximum when cross-polarised with the incident probe beam.

Spin grating decays were measured and the square root of the diffracted intensity fitted with:

$$I = y_0 + \alpha \exp\left(-0.5\left(\frac{t-t_0}{b}\right)^2\right) + d \exp(-g(t-t_0)) \left(1 + \operatorname{erf}\left(\frac{2(t-t_0)-\Delta t_0^2}{2\Delta t_0^2}\right)\right) \quad (8.20)$$

where  $g$  is the decay rate as defined by:

$$g = \frac{1}{\tau_R} + \frac{2}{\tau_s} + \frac{4D_e\pi^2}{\Lambda^2} \quad (8.21)$$

Figure 8-10 and Figure 8-11 show the square root spin grating diffracted intensity decays with fitted curves for 6.3 and 5.3 micron grating periods.

The recombination time,  $\tau_R$ , is very long compared to the grating decay and spin relaxation times so  $1/\tau_R$  is negligible. Plotting  $(g-2/\tau_s)$  against  $4\pi^2/\Lambda^2$  we can fit a straight line through the origin with a gradient of the electron diffusion coefficient, Figure 8-12.

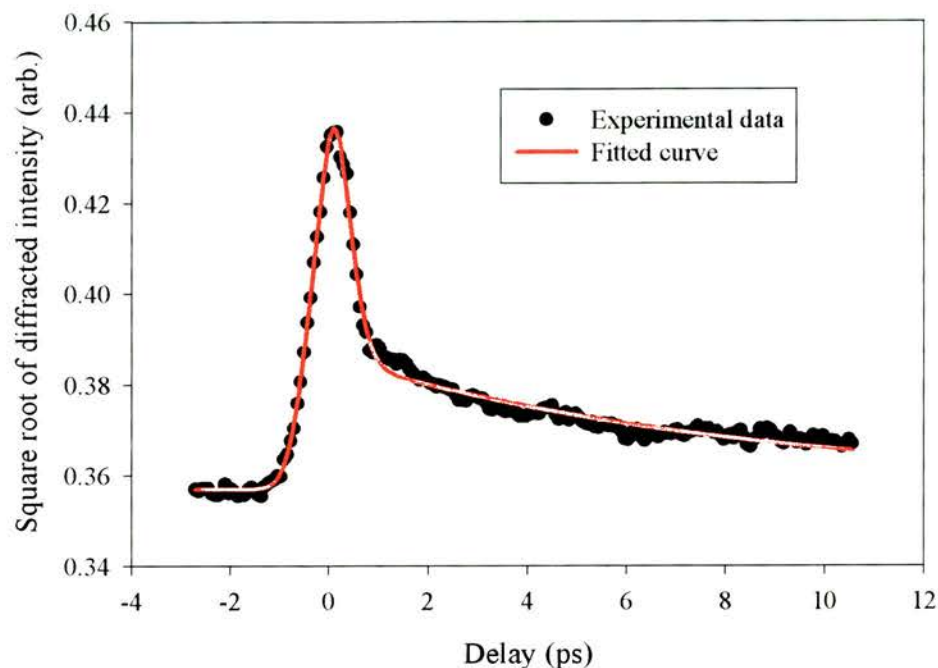


Figure 8-10 Spin grating decay for a 6.3 micron grating.

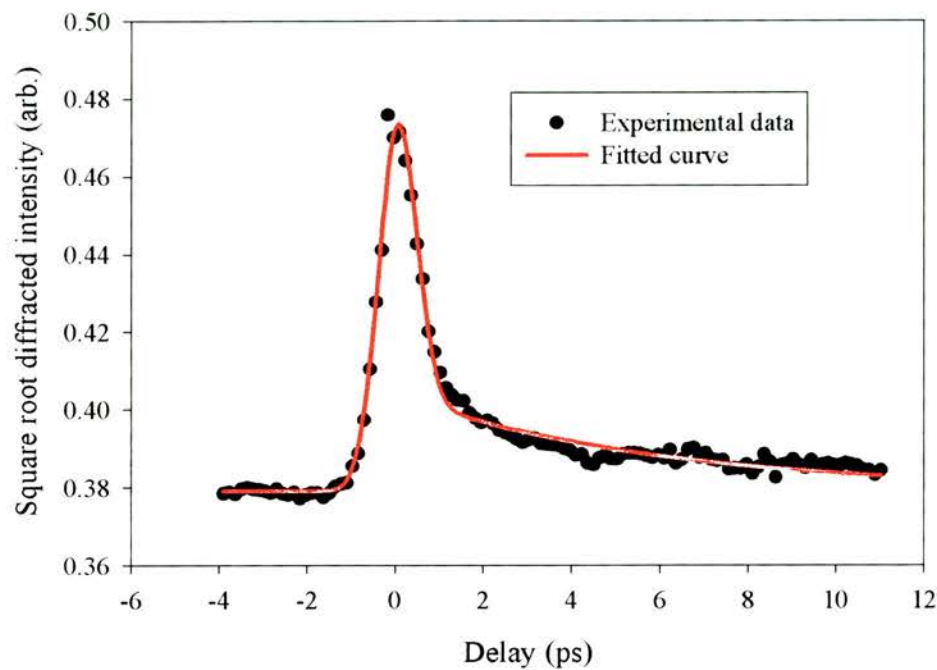


Figure 8-11 Spin grating decay for a 5.3 micron grating.

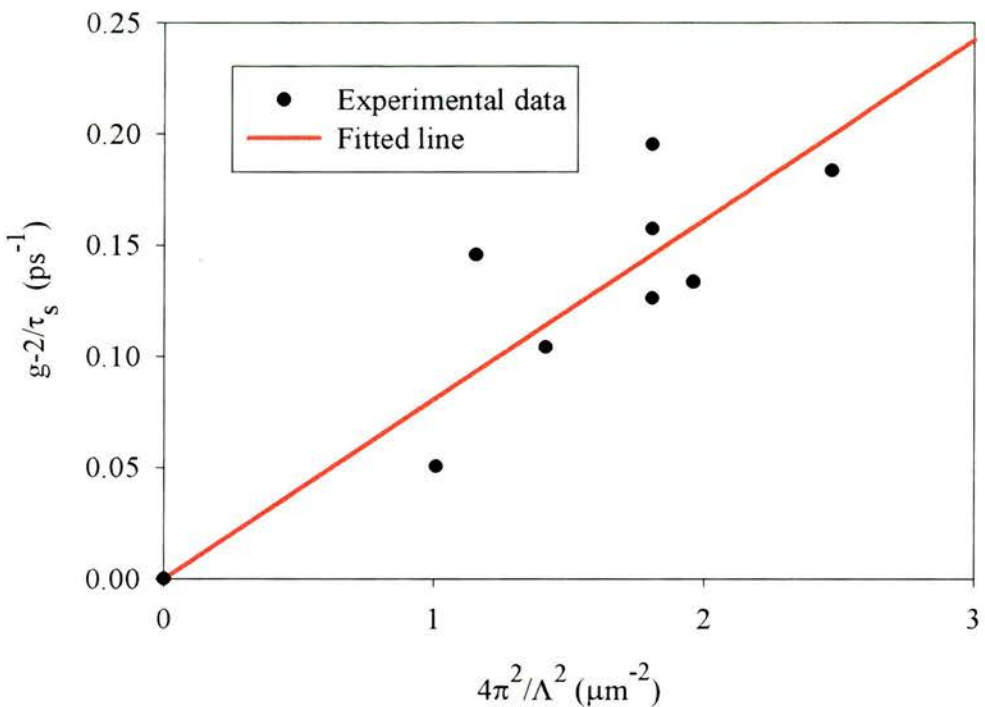


Figure 8-12 Measured diffracted signal decay rates for the spin grating minus the spin relaxation rate against  $4\pi^2/\Lambda^2$ . The gradient gives an electron diffusion coefficient of

$$810\text{cm}^2/\text{s.}$$

## 8-7 Analysis

### 8-7-1 Amplitude grating discussion and conclusion

From Figure 8-8 we obtained an intrawell ambipolar diffusion coefficient of  $7.2 \text{ cm}^2/\text{s}$  for an InGaAsP multiple quantum well sample by fitting a straight line to the data and calculating the gradient. A hole mobility of  $140 \text{ cm}^2/\text{Vs}$  is deduced from the Einstein equation, with the assumption that  $D_a=2D_h$ , see chapter 2.

The ambipolar diffusion coefficient result may be compared to the measured value of  $7.4 \text{ cm}^2/\text{s}$  for the diffusion coefficient in bulk-like InGaAsP epitaxial layers and to  $8.0 \text{ cm}^2/\text{s}$  for a compressively strained InGaAsP MQW SOA<sup>13,14</sup>. This leads us to the conclusion that there is little effect of quantisation or interface scattering on the hole mobility. Similar studies in GaAs also gave good agreement for hole mobilities when compared to the bulk case. In InGaAsP there is tendency for As to diffuse from areas of high concentration into areas of lower concentration, and for As to carry over in the gas phase during growth. We would therefore expect more interface scattering.

Similar measurements in GaAs gave a hole mobility of  $257 \text{ cm}^2/\text{Vs}$ <sup>12</sup>. Drift mobility is proportional to the scattering time and inversely to the effective mass. The hole effective mass of bulk InGaAsP is  $0.43m_0$ . This is comparable to  $0.50m_0$  for bulk GaAs. Therefore, it is deduced from the lower hole mobility results in InGaAsP that an increase in interface scattering gives a significant contribution to the hole drift mobility. Comparing InGaAsP to GaAs results therefore indicate alloy scattering is important<sup>1</sup>.

### 8-7-2 Spin grating discussion and conclusion

The spin grating decays were on the edge of the resolution of the system. However plotting the results in the way shown in Figure 8-12 gave a clear grating spacing dependence. From the slope of the results given in Figure 8-12 we obtained an electron

diffusion coefficient of  $807\text{cm}^2/\text{s}$  for sample MR1168. This would give an electron mobility of  $30,000\text{cm}^2/\text{Vs}$  (see chapter 2).

For GaAs multiple quantum wells the electron mobility is of the order of  $4000\text{cm}^2/\text{Vs}$ <sup>12</sup>.

For bulk  $\text{In}_{0.84}\text{Ga}_{0.16}\text{As}_{0.33}\text{P}_{0.67}$  the room temperature electron mobility for doping concentrations of  $10^{16}\text{ cm}^{-3}$  is expected to be  $3800\text{cm}^2/\text{Vs}$ <sup>17</sup>. Good quality bulk InP measured an electron mobility of  $5400\text{ cm}^2/\text{Vs}$  and  $40,000\text{cm}^2/\text{Vs}$  for InAs. Flatte et al<sup>18</sup> expected mobility for InGaAsP quantum wells in the range  $6800\text{cm}^2/\text{Vs}$  to  $10000\text{cm}^2/\text{Vs}$ .

Therefore, we have anomalously high electron mobility. This value of  $30,000\text{cm}^2/\text{Vs}$  does give a good prediction for the spin relaxation times measured for these samples, as calculated by M. Flatte et al<sup>18</sup> (see chapter 6).

The high mobility value may be explained by the build up of carriers due to the long carrier lifetime. The shorter repetition time of the laser source leads to a regime of high carrier density. Approaching degeneracy for the carriers will change the density dependence of the diffusion coefficient<sup>19</sup>. The diffusion can be described by<sup>20</sup>:

$$D_e(n_e) = D_0 \frac{(n_e/n_s)}{\left(1 - e^{-n_e/n_s}\right)}$$

where (8.22)

$$D_0 = \frac{kT}{\gamma_e^{\text{eff}} m_e}, \quad \frac{1}{n_s} = \frac{\pi \hbar^2}{m_e kT}$$

Where  $\gamma_e^{\text{eff}}$  is the effective electron momentum damping rate and  $n_e$  refers to either spin component. In the low-density regime, ( $n_e < n_s$ ), the diffusion coefficient is given by  $D_0$ . However, for  $n_e > n_s$  we have<sup>19</sup>:

$$D_e \approx (n_e/n_s) D_0 (8.23)$$

This shows that the diffusion coefficient grows linearly with electron concentration with eventual saturation. Wright<sup>19</sup> found that for GaAs and InGaAsP  $n_s$  is approximately  $5 \times 10^{11} \text{ cm}^{-2}$ . The built up of electrons due to the high carrier lifetime makes it likely that the densities are reaching this regime. Flatte and Byers<sup>21</sup> saw a similar dependence for doped bulk semiconductors. More studies are needed with a shorter duration pulse source (femtosecond) that can accurately resolve the short timescales and a slower pulse repetition in order to solve this issue.

Another possibility is the existence of spin mobility. This is unlikely at room temperatures and in undoped semiconductors but should be considered,. This is the diffusion of electron spins and is usually observed when spin packets are created in highly doped semiconductors. Spin packets or clusters are created and the spins diffuse out of these by flipping spin with neighbouring carriers. Awschalom et al<sup>22</sup> have reported the spin diffusion time to be anomalously high, finding times on the order of ten times faster than the electron diffusion.

To conclude the spin grating measurements have shown up a high mobility. We propose that a high carrier density regime is accessed because of carrier build-up.

**8-8 Bibliography**

- 1 A. Miller, in *Nonlinear optics in semiconductors Vol II; Vol. 59*, edited by E. Garmire and A. Kost (Acad. Press, San Diego, 1999), p. 287-312.
- 2 A. Miller, R. J. Manning, P. K. Milsom, D. C. Hutchings, D. W. Crust, and K. Woodbridge, "Transient grating studies of excitonic optical nonlinearities in GaAs/AlGaAs multiple-quantum-well structures," *J. Opt. Soc. Am. B-Optical Physics*, **6** (4), pp. 567-578, 1989.
- 3 D. A. B. Miller, D. S. Chemla, D. J. Eilenberger, P. W. Smith, A. C. Gossard, and W. Wiegmann, "Degenerate 4-wave mixing in room-temperature GaAs/GaAlAs multiple quantum well structures," *App. Phys. Lett.*, **42** (11), pp. 925-927, 1983.
- 4 H. J. Eichler and F. Massmann, "Diffraction efficiency and decay times of free-carrier gratings in silicon," *J. Appl. Phys.*, **53** (4), pp. 3237-3242, 1982.
- 5 S. C. Moss, J. R. Lindle, H. J. Mackey, and A. L. Smirl, "Measurement of the diffusion coefficient and recombination effects in germanium from optically-induced picosecond transient gratings," *Appl. Phys. Letts.*, **39** (3), pp. 227-229, 1981.
- 6 C. H. Hoffman, K. Jarasiunas, H. J. Gerritsen, and A. V. Nurmikko, "Measurement of surface recombination velocity in semiconductors dy diffraction from picosecond transient free-carrier gratings," *Appl. Phys. Lett.*, **33** , pp. 536, 1978.
- 7 K. Jarasiunas and J. Vaitkus, "Properties of laser induced gratings in CdSe," *Phys. Stat. Sol. (a)*, **23** , pp. K19, 1974.
- 8 V. Kremenitski, S. Odulov, and M. Soskin, "Dynamic gratings in Cadmium Telluride," *Phys. Stat. Sol. (a)*, **51** , pp. K63, 1979.

- 9 K. Jarasiunas and H. J. Gerritsen, "Ambipolar diffusion measurements in semiconductors using nonlinear transient gratings," *Appl. Phys. Lett.*, **33**, pp. 190, 1978.
- 10 D. S. McCallum, X. R. Huang, M. D. Dawson, T. F. Boggess, A. L. Smirl, and T. C. Hasenberg, "Picosecond room-temperature excitonic-absorption saturation and 4-wave-mixing in InAs/GaAs short-period strained-layer superlattices," *Superlattices and Microstructures*, **8** (1), pp. 127-130, 1990.
- 11 H. Weinert, J. Kolenda, and M. Petrauskas, "Lateral Transport in GaAs-(Al,Ga)As superlattice investigated by transient grating measurements," *Sol. State Commun.*, **81**, pp. 467, 1992.
- 12 A. R. Cameron, P. Riblet, and A. Miller, "Spin gratings and the measurement of electron drift mobility in multiple quantum well semiconductors," *Phys. Rev. Lett.*, **76** (25), pp. 4793-4796, 1996.
- 13 D. X. Zhu, S. Dubovitsky, W. H. Steier, J. Burger, D. Tishinin, K. Uppal, and P. D. Dapkus, "Ambipolar diffusion coefficient and carrier lifetime in a compressively strained InGaAsP multiple quantum well device," *App. Phys. Lett.*, **71** (5), pp. 647-649, 1997.
- 14 S. Juodkazis, M. Petrauskas, A. Quacha, and M. Willander, "Charge-carrier recombination and diffusion in InGaAs(P) epitaxial layers," *Phys. Stat. Sol. (a)*, **140** (2), pp. 439-443, 1993.
- 15 A. Miller, P. Riblet, M. Mazilu, S. White, T. M. Holden, A. R. Cameron, and P. Perozzo, "Exciton saturation in GaAs multiple quantum wells at room temperature," *J. Appl. Phys.*, **86** (7), pp. 3734-3744, 1999.
- 16 A. R. Cameron, Thesis, University of St Andrews, 1996.

- 17 "GaInAsP Alloy Semiconductors," edited by T. P. Pearsall (John Wiley and Sons Ltd., 1982).
- 18 M. Flatte, *Spin relaxation in InGaAs(P)*; Personal correspondence; 7 June 2000.
- 19 E. M. Wright, *Spin diffusion in InGaAsP*; Personal Communication; July 2, 2000.
- 20 H. Haug and S. W. Koch, *Quantum Theory of hte Optical and Electronic Properties of Semiconductors*, 1 ed. (World Scientific, Singapore, 1990).
- 21 M. E. Flatte and J. M. Byers, "Spin diffusion in semiconductors," *Physical Review Letters*, **84** (18), pp. 4220-4223, 2000.
- 22 J. M. Kikkawa and D. D. Awschalom, "Lateral drag of spin coherence in gallium arsenide," *Nature*, **397** (6715), pp. 139-141, 1999.

## Chapter 9

### Conclusions

The production of a Ti-Sapphire periodically poled lithium niobate optical parametric oscillator (OPO) has allowed an investigation of the ultrafast carrier and spin dynamics in InGaAsP multiple quantum wells. An all-optical polarisation switch with very interesting characteristics was demonstrated and an optically induced birefringence discovered.

The OPO was initially constructed with an argon-ion laser pumping a mode-locked Ti-Sapphire laser. The introduction of a solid state Millennia laser significantly improved the threshold, the stability and the beam quality of the resultant pulses from the OPO. Temperature and pump wavelength tuning attained an OPO wavelength range of 1.3 to 1.57 microns. The reflection coatings of the mirrors and output coupler set the lower wavelength limit and degeneracy (signal wavelength equal to that of the idler) presented the higher limit. Under Millennia pumping conditions, a point of zero dispersion at 1.52 microns created the need for a single prism in the cavity to be able to control the dispersion. With this in place, length tuning of up to 40 nm could be achieved by translating the output coupler. The wide tunability and high stability of the OPO made this an ideal source for the investigation of carrier dynamics of semiconductors at these fibre compatible telecommunication wavelengths.

The long carrier lifetime of 100's of nanoseconds in an undoped sample gives an idea of the high quality of the samples used. The decay times were significantly longer than GaAs quantum well samples previously investigated in St Andrews. The combined

effect of the carrier lifetime and the repetition time of the laser system (12ns) meant that the carrier density accumulated with each pulse, until a situation of equilibrium was reached. Therefore, the states were still filled at the zero-delay setting because of the previous pulse in the pump-probe system. This was apparent in pump-probe measurements by a signal before zero delay in both linear and circular polarisation configurations. The measurement of the lifetime by pump-probe methods under the current system was not possible because of the laser repetition frequency. An alternative method of time resolved photoluminescence was employed using a low repetition rate system. The undoped sample MR1168 has a long, non-exponential decay with a 1/e value of over 200ns. Radiative lifetime is proposed with a decay coefficient of  $10^{-10}\text{cm}^3/\text{s}$ , which agrees with previous results for bulk InGaAsP. The five p-i-n structures all gave much faster recoveries due to sweep-out effects resulting from the built-in electric field. Electron and hole sweep-out times are proposed to be responsible for the observed exponential decays with relaxation times of approximately 6ns and 40ns respectively. Further studies on these samples using applied fields as a function of temperature would confirm whether thermionic emission and/or tunnelling together with carrier sweep-out are the mechanisms involved here.

The spin relaxation times for InGaAsP MQWs were found to be in the range of 10 to 30ps. Circular polarisation pump-probe experiments using picosecond pulses exploiting the lifting of the degeneracy of the heavy hole exciton were found to be a good direct method of measuring the spin relaxation rates. The well width dependency of these rates was compared to that of GaAs. GaAs has been extensively studied and the mechanism of spin relaxation concluded to be that of D'yakonov-Perel, where the spin-splitting of the conduction band is ultimately responsible. Taking into account the difference in energy gap for the two material systems the results show a very good equality in relaxation times with well width. From this, and theoretical predictions by

Flatte et al, we deduce that the dominant mechanism is the same in each case. However, the actual percentage of contribution of the D'yakonov-Perel mechanism is unsure. The Elliot-Yafet mechanism is also a result of bandstructure effects and this poses the question of whether the two are linked. The Bir, Aranov and Pikus mechanism, which relies on exchange effects, is currently considered to dominate at room temperature. However, this thesis concentrated on the room temperature effects because of the high current interest in integration and switching in telecommunication systems.

Transient grating experiments allowed the measurement of the intrawell ambipolar and electron diffusion. The ambipolar diffusion coefficient and hole mobility were determined to be  $7.2 \text{ cm}^2/\text{s}$  and  $140 \text{ cm}^2/\text{Vs}$  respectively in the undoped InGaAsP multiple quantum well sample. Comparison with reported measurements in bulk-like InGaAsP epitaxial layers and a compressively strained InGaAsP MQW semiconductor optical amplifier concludes that there is little effect of the quantisation on the hole mobility. A comparison between these InGaAsP results and previous similar experiments in GaAs multiple quantum wells concluded that alloy scattering gives a significant contribution to the hole drift mobility.

Interband selection rules in quantum wells allowed the creation of an electron spin grating from a polarisation grating. The decay of this spin grating enabled the determination of an electron diffusion coefficient. This was found to be considerably higher than expected in comparison to accepted values for bulk material. The most probable explanation derives from the long carrier lifetime. The consequent build up of carriers introduces a large concentration, which increases the diffusion under degenerate conditions into a saturation regime. Further investigation is required with a shorter pulse duration source to fully resolve the fast grating decay and to clarify concentration dependence of the diffusion

The most interesting findings have been through the examination of the all-optical polarisation switch. The possibility of creating an effective positive and negative switch is extremely attractive from the point of view of telecommunications. The ease at which the investigated switch can be changed from one state to the other by using pump pulses of the opposite circular polarisations makes this a unique system for exploitation.

The long-lived carriers before zero delay introduced the ability an induced birefringence for the first time. This is small effect but the configuration of cross polarisation allows for very sensitive measurements. The birefringence in the InGaAsP multiple quantum wells was very surprising due to the symmetry of cubic zinc-blende lattice and its bandstructure. Modelling of the results under different conditions confirmed the existence of induced birefringence. The most viable explanation for the birefringence arises from the fact that the samples themselves are grown on a wedged substrate to enable the layers to adhere during the growth process. This creates a step like pattern on the sample. When excess carriers are generated, they distribute themselves along these stripes producing an asymmetry in the refractive index and creating the birefringence.

Work on electron spins in semiconductors is important for the design of new devices for telecommunications systems. The field of spintronics aims to control the electron spin instead of its charge. Optical switches are essential in the expanding world of telecommunications where there is an ever-increasing need for employing the full optical fibre bandwidth. Spin relaxation provides the picosecond timescales needed to achieve this. The quaternary semiconductor InGaAsP is of great interest in the design of these switches due to the compatibility of the band gap energy with optical transmission windows in the 1.3 and 1.5 spectral regimes.

As well as for switches, electron spins are also being exploited for use as memory by preserving the spin state over long times and distances. This is done coherently in conjunction with magnetic fields. Long-term prospects could be development of quantum computing schemes using the electron spins.

In conclusion, the work presented in this thesis is an integral part of an escalating field that exploits the spin of the electron to enable faster communications and new ways of storing and manipulating information.

## Chapter 10

### Publications

#### ***10-1 Journal Publications***

"In-Well Ambipolar Diffusion in Room Temperature InGaAsP Multiple Quantum Wells"

D. Marshall, A. Miller and C.C. Button.

IEEE Journal of Quantum Electronics, Vol. 36, No. 9, September 2000 pp 1013-1015.

"Carrier transport, ultrafast spin dynamics and polarisation switching in InGaAsP multiple quantum wells"

D. Marshall and A. Miller

Submitted for Special Issue on "Components for Ultrafast Communications" of Optical and Quantum Electronics.

"Spin relaxation in InGaAsP Multiple quantum wells"

D. Marshall, A. Miller and C.C. Button

*In Preparation*

"Polarization switching and induced birefringence in InGaAsP multiple quantum wells at 1.525 microns."

D. Marshall, A. Miller and C.C. Button

*In Preparation*

## ***10-2 Conference publications***

“Spin relaxation and all-optical polarisation switching in InGaAsP multiple quantum wells at 1.55 microns.”

(D. Marshall) J.T. Hyland, G.T. Kennedy, A. Miller and C.C. Button.

Paper QtuA4-1, Quantum Electronics, Snowmass, CO, April 12-13, 1999.

“In-well diffusion in InGaAsP multiple quantum wells”

D. Marshall, M. Ebrahimzadeh, A. Miller and C.C. Button.

Paper QThl5, QELS, San Francisco, CA, May 7-12, 2000.

“Polarisation switching and long lived circular dichroism in InGaAsP multiple quantum wells at 1.525 microns”

D. Marshall, M. Mazilu, M. Ebrahimzadeh, A. Miller and C.C. Button.

Paper CWP3, CLEO, San Francisco, CA, May 7-12, 2000.

“Spin-dependent excitonic optical nonlinearities and ultrafast polarisation switching in quantum wells”

D. Marshall

IOP meeting, Time Resolved Spectroscopy of Semiconductors: Recent developments and applications, University of Sheffield, June 13<sup>th</sup>, 2000.

“Room temperature spin gratings in InGaAsP multiple quantum wells”

Dawn Marshall, Michael Mazilu, Alan Miller

Paper QTuH5 CLEO Europe/IQEC, Nice, France, September 10-15, 2000

Chapter 10

Publications

“Excitonic Optical Nonlinearities and Ultrafast Polarization Switching in Quantum Wells”

Alan Miller and Dawn Marshall

Paper CTuD1 (Invited) CLEO Europe/IQEC, Nice, France, September 10-15, 2000

## Chapter 11

### Acknowledgements

Firstly I would like to thank my supervisor Alan Miller for his support and for putting up with all my strange results as well as sending me to conferences in Snowmass , San Francisco  and Nice .

To Jason Smith and Gerald Buller I am very grateful for the photoluminescence measurements and to Michael Flatte for the spin relaxation theoretical predictions.

To the people in the lab I would like to say a big thank you. Jonathan, pushing the end mirror on the OPO whilst looking for the much-awaited green flash for three months wouldn't have been the same without you. Michael thanks for putting up with my lack of maths and for the help with the modelling. Jim thanks for remaining contactable by email to answer my questions about pump-probe. To Steve good luck in your post-doc - I did warn you about those dots! To Julia and Andy, good luck. Julia - remember to leave some biscuits out at night for the gremlins in the lab and have fun with the OPO!!

Thanks to all the physics department staff, especially Mary for arranging appointments with Alan.

To my parents for providing the much appreciated financial support which enabled Daisy (my car!) to have a happy three years in and around St Andrews.

Tom, for all your support and encouragement over the past three years.

To everyone else I knew in St Andrews, both past and present, thanks for making my time here so enjoyable, for coming to the pub whenever necessary (which tended to be quite a lot) and for not laughing too much at my antics once we got there...

And finally thanks to the Engineering and Physical Sciences Research Council for financing this work.